UNIVERSITY OF THESSALY

SCHOOL OF ENGINEERING

DEPARTMENT OF MECHANICAL ENGINEERING

NUMERICAL INVESIGATION OF THE SHOCK WAVE STRUCTURE WITH KINETIC AND CONTINUUM MODELS

by

ALEXANDROS TSIMPOUKIS

Mechanical Engineer

Diploma, Department of Mechanical Engineering
Aristotle University of Thessaloniki

Submitted in Partial Fulfillment of the Requirements for the

Specialization degree of Postgraduate Diploma

in the Department of Mechanical Engineering,

University of Thessaly

VOLOS, 2015

Acknowledgements

I would like to express deepest gratitude to my supervisor Professor Dimitris Valougeorgis for his full support, expert guidance, understanding and encouragement throughout my study and research. Without his patience and counsel, this dissertation would not have been completed. I am also grateful to Professors Andritsos Nikos and Mathioulakis Dimitrios for serving as members of my Thesis Committee and for their comments and suggestions. I would also like to express my gratitude to the Ph.D. student Christos Tantos who created the first version of the kinetic code and for his valuable support and assistance throughout my postgraduate work. Above all, I would like to thank my parents for their unconditional support during the last year.

October, 2015

Alexandros Tsimpoukis

Abstract

The detailed structure of normal shock waves is a fundamental research problem with important applications and it is commonly implemented to benchmark the validity of novel numerical schemes investigating and describing the state of a gas far from local equilibrium. The most powerful approaches to handle this type of flows is the Direct Simulation Monte Carlo method and the numerical solution of the Boltzmann equation or of reliable kinetic model equations. The present work is based on the latter approach.

In particular, the non-linear Bhatnagar-Gross-Krook (BGK), ellipsoidal statistical (ES) and Shakhov (S) kinetic models, subject to Rankine-Hugoniot boundary conditions, are applied, to solve the one dimensional compressible normal shock wave problem. The intermolecular collisions are modeled by the inverse power law model. The computational scheme is based on finite volume in the physical space and on the discrete velocity method in the molecular velocity space. A Navier-Stokes solution is also obtained based on a typical 4th-order Runge-Kutta integration.

The kinetic solution is obtained in a wide range of the Mach number (up to 25) with the local Knudsen number varying in the whole range of gas rarefaction. The numerical results include the distributions of all macroscopic quantities of practical interest including the perpendicular and normal temperatures as well as the shock thickness in terms of the Mach number. In addition the detailed structure of the distribution function in several positions is provided based on the BGK, ES and S models. A detailed comparison with previous computational results available in the literature by the DCMC method and the direct solution of the full Boltzmann equation (BE) as well as with experimental work is performed.

Based on the numerical results it is clearly demonstrated that the S model is the most reliable choice for normal shock waves because it compares very well with the DSMC, BE and experimental results for all Mach numbers tested. It is noted that the computational effort is significantly reduced when model equations, instead of the DSMC method or the BE are introduced. An interesting issue is that as the Mach number is increased the shock thickness is rapidly decreased up to a characteristic Mach number and then is increased in a very slow pace. This minimum thickness of the shock front which is observed at about Mach number equal to 3 is analogous to the so-called Knudsen minimum and it has been also reported in previous theoretical and experimental works. Also, both the hard sphere and Maxwell intermolecular models are applied. It is found that the applied intermolecular potential model significantly influences the bulk quantities and shock structure due to the large temperature gradients and therefore, reliable intermolecular models corresponding to real gases must be introduced. Furthermore, the range of the validity of the Navier-Stokes equations along with the corresponding distribution functions in high Mach numbers are

tested and it is concluded that the classical Navier-Stokes approach is valid only for small Mach numbers resulting to flow conditions close to local equilibrium.

Nomenclature

f	distribution function
f^{0}	absolute Maxwellian
f^{M}	the local Maxwellian
g	distribution function, dimensionless
Y	reduced distribution function
Φ	reduced distribution function
k	Boltzmann constant, [*J/K*]
Kn	Knudsen number, dimensionless
m	mean molecular mass, [*kg*]
M	Mach number, dimensionless
M_1	upstream Mach number, dimensionless
n	number density, [*number of particles/m*^{3}]
P	pressure of the gas, [*Pa*]
P_0	equilibrium pressure of the gas, [*Pa*]
q	heat flux vector, dimensionless
$\hat{q}$	heat flux vector, [*W/m*^{2}]
R	gas constant, [*J/(kgK)*]
Re	Reynolds number, dimensionless
T	temperature of the gas, $[K]$
$\hat{u}$	macroscopic velocity vector, [*m/sec*]
u	macroscopic velocity vector, dimensionless
$\tilde{u}$	normalized macroscopic velocity vector, dimensionless
u_1	upstream macroscopic velocity vector, dimensionless
u_2	downstream macroscopic velocity vector, dimensionless
u_0	most probable molecular velocity, [*m/sec*]
v	collision frequency
c_i	molecular velocity vector, dimensionless
c_{ref}	reference molecular velocity vector, dimensionless
x,y,z	coordinates, dimensionless
$\hat{x},\hat{y},\hat{z}$	coordinates, [m]

Greek

γ	ratio of specific heats, dimensionless
λ_0	mean free path of the molecules, $[m]$
μ	viscosity of the gas, $[Pa\ \sec]$
ξ	molecular velocity vector, $[m/\sec]$

ρ	number density, dimensionless
$\tilde{\rho}$	normalized number density, dimensionless
$\hat{\sigma}_{ij}$	stress tensor, [$Pa=N/m^2$]
σ_{ij}	stress tensor, dimensionless
τ	temperature of the gas, dimensionless
$\tau_{//}$	parallel (or longitudinal) temperature of the gas, dimensionless
$\tau_{\perp}$	perpendicular temperature of the gas, dimensionless
$\hat{\tau}$	normalized temperature of the gas, dimensionless
ω	intermolecular model being implemented, dimensionless
n	exponent of the intermolecular force law for DCMC, dimensionless
ε	perturbation
ε_i	specific internal energy
α	speed of sound, [*m/sec*]

Table of contents

Chapter 1

Introduction

1.1 Main characteristics of shock waves

Violent disturbances that occur from detonation of explosives from the flow through rocket nozzles, supersonic flight of projectiles or from impact on solids, differ greatly from the "linear" phenomena of sound, light or electromagnetic signals. The propagation of violent disturbances is governed by nonlinear differential equations, and as a consequence the familiar laws of superposition, reflection, and refraction cease to be valid. For example, shock front is one of these occurrences. Across shock fronts the medium undergoes sudden and often considerable changes in velocity, pressure, and temperature. Even when the start of the motion is perfectly continuous, shock discontinuities may later arise automatically. Yet, under other conditions, just the opposite may happen; initial discontinuities may be smoothed out immediately. Hence, shock waves are nearly instantaneous changes in the particle velocity, pressure, temperature, entropy and density in a solid, liquid or gaseous medium [1]. Shock waves form when a wave following the loading profile of an initial disturbance moves faster than the leading edge. The increase in the trailing edge velocity occurs because the sound speed of a material increases as the density increases. In other words the leading edge of the shock wave compresses the material thereby increasing the density. Subsequently, the portion of the wave traveling through the higher density material moves faster until it catches the leading edge. This steep wave is now a nearly instantaneous change in the material state and is called a shock wave.

Shock front thicknesses are finite and on the order of the molecular mean free path of the medium, on the order of four mean free paths for gases and one mean free path for solids. For example, for ambient pressure range the mean free path is 68 nm, for low vacuum is 0.1 to 100 μm, for medium vacuum is 0.1 to 100 mm and for high vacuum is 10 cm to 1 km [2]. Moreover, irreversible conditions exist within the shock front due to plastic deformation (solids), viscous shear stress and heat conduction (solids, liquids, gases) as material flows in the direction of the shock. While conditions in the shock front are non-adiabatic, irreversible and non-equilibrium, outside the shock front the material is assumed to be adiabatic and reversible. This is graphically illustrated in Fig. 1.1.

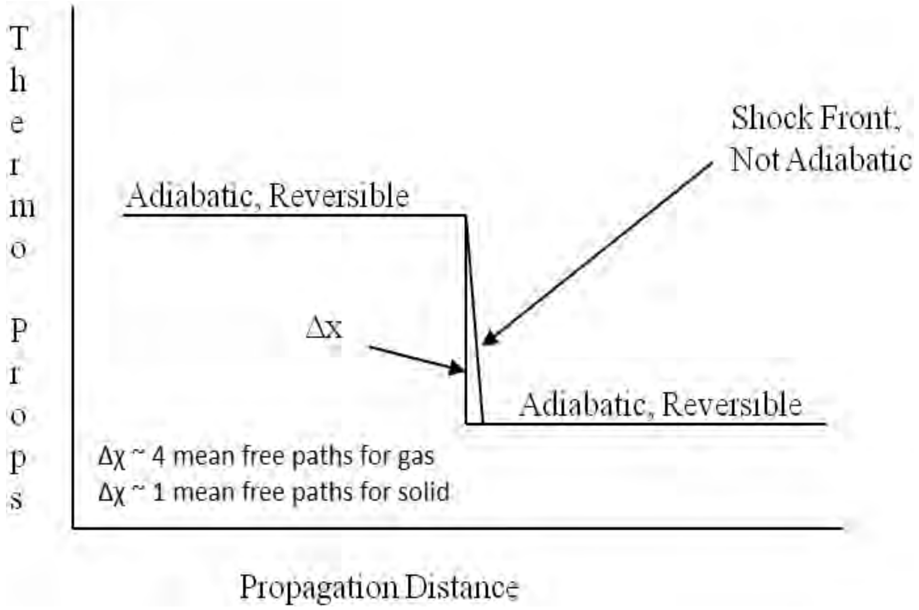

Figure 1.1: Shock front thickness is on the order of the molecular mean free path of the medium, i.e. Δx~4 for a gas and Δx~1 for solids [1].

In relation to a stationary point some finite distance from the shock front the processes are adiabatic because the shock velocity is much greater than the sound speed of the medium. Since conduction occurs at speeds much slower than the speed of sound there is insufficient time for conduction to occur between the shock front and the material immediately behind or in front of the shock. Within the shock front the mechanism that increases the temperature and pressure is momentum transfer and the irreversibilities associated with this process are approximated by heat conduction. In addition, processes away from the shock front are assumed to be reversible, i.e. when unloaded the material returns to its initial state. Thus, away from the shock front processes are assumed isentropic.

To compute the shock wave structure, it should be understood that the small length scales are usually considered to be too minute to resolve numerically. Using the continuum approach, with very high computational resolution, it is able to numerically resolve the shock front in Argon gas under various loading conditions. However, the Navier- Stokes (NS) equations [3] do not apply after a certain Mach number, since the theory of continuous medium collapses and the methods based on kinetic theory must be considered.

1.2 Literature review

There are several approaches in order to compute the shock wave structure. In this thesis two of them namely kinetic modeling and the typical NS approaches are examined. To understand their differences, the so-called Knudsen number is introduced. This characteristic number, which determines the degree of gas rarefaction and the area in which continuum model equations are valid, is defined by the relationship [4]

$$Kn = \frac{\lambda}{L} = \sqrt{\frac{\gamma\pi}{2}}\frac{M}{Re} \tag{1.1}$$

where L is a characteristic dimension of the problem, λ the mean free path of the particles, γ the ratio of specific heats, M the Mach number and Re the Reynolds number. The mean free path is defined as the average distance travelled by molecules between collisions. The importance of the Knudsen number is presented in Fig. 1.2.

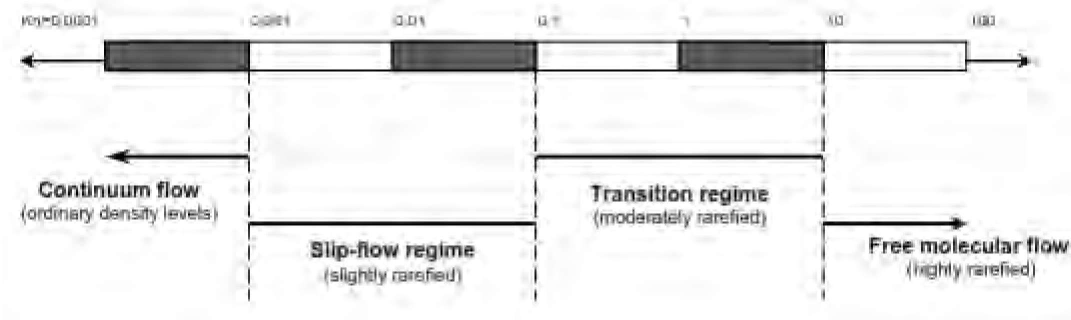

Figure 1.2: Knudsen number regimes [5].

It is the most important parameter that can be used to describe the non-equilibrium properties of the gas, which in a shock wave can be defined as a relation between the mean free path and the shock thickness. In the shock wave, macroscopic properties of the gas can change very rapidly within a short distance, which is about several mean free paths and the Knudsen number becomes quite large. The NS equations are valid in the continuum and slip regimes shown in Fig. 1.2, while kinetic modeling is valid in the whole range of the Knudsen number but becomes computationally expensive in small Knudsen numbers. Nevertheless, strong shock waves post a computational challenge in the study of stationary highly non- equilibrium flows.

1.2.1 Continuum models

It has been proved that the shock wave structure can be described well by fluid dynamic equations in the sense that NS equations give good agreement with the experimental data only at Mach numbers M<1.3 [3]. When the rarefied non-equilibrium effect is large, the macroscopic fluid models for viscous stress and heat transfer break down. Moreover, when applying the Burnett and super Burnett equations (or the so-called extended hydrodynamic approach) in the shock prediction some non-physical oscillations were found to appear in the solution even at M=2 [6].

Furthermore, in order to provide an improvement on the continuum equations, Mott-Smith [7] proposed a solution to the Boltzmann equation which is based upon assuming that the local distribution function is composed of weighted parts of the upstream and downstream equilibrium distributions. This bimodal method gives thicker shocks than the NS equations and considerably better agreement with experimental results at large Mach numbers as indicated by Schmidt [8].

Finally, in Grad method [9] and extended irreversible thermodynamics [10], a large number of hydrodynamic partial differential equations must be solved to get reasonable accuracy. The famous Grad's 13-moment method is successful in simulating the shock profile below the critical value M=1.65. When increasing the number of moments in extended thermodynamics, the solution converges rather slowly. Therefore, a large number of moments is required to get the accurate shock structure at large Knudsen numbers. At Mach numbers M<9.36, for example, one needs up to 15180 moments in extended hydrodynamics (506 one-dimensional equations). Hence, there is a need for accurate models which give reliable solutions with lower computational costs.

1.2.2 Experiments

Many experiments have been reported on shock thickness measurements, usually based on the density profile. Robben and Talbot [11] have made available their density profile data at M=10.7 from which the argon shock thicknesses are obtained. These measurements have been made in a low density wind tunnel and hence at very low free-stream temperatures. Alsmeyer [3] has published density profiles at M=8 using argon and shock thicknesses at various Mach numbers. Measurements of density profiles in an argon shock formed in a shock tube experiment are also reported by Schmidt [8] for M=2.8, 4, 6, and 8. At the larger Mach number, the temperatures within the shock become quite high. Finally, for M=25 there is an experiment by Pham-Van-Diep, Erwin and Muntz, who acquired the velocity distribution functions for certain spots and then compared them with DCMC results [12]. Most of the described experimental work is used in Chapter 4 to compare the present computational results with measurements.

1.2.3 Kinetic models

Due to the inadequacy of the continuum models to capture the shock thickness properly a different approach for solving shock waves is examined which is based on the kinetic theory related to dilute gases as founded by Maxwell and Boltzmann.

A particle at time t is characterized by its position vector $\mathbf{r} = (x, y, z)$ and its molecular velocity vector $\boldsymbol{\xi} = (\xi_x, \xi_y, \xi_z)$, $\xi \in (-\infty, +\infty)$. The basic unknown is the function f, which is called distribution function of the particles and it is defined so that the quantity $f(r, \xi, t)\, d^3r d^3\xi$ is the expected number of particles contained in the volume d^3r around r with molecular velocity in $d^3\xi$ around ξ at the time t. The distribution function f satisfies the Boltzmann transport equation.

$$\frac{\partial f}{\partial t}+\xi\frac{\partial f}{\partial \hat{r}}=J\left(f,f^{*}\right) \tag{1.2}$$

The left hand side of Eq. (1.2) represents the material derivative, is linear and it is treated with techniques from partial differential equations. The right-hand side of Eq. (1.2) represents the balance between molecules «lost» or «gained» during the binary molecular collisions. The term *J* (*f*, *f**) is the nonlinear collision integral that describes the net effect of populating and depopulating particles through collisions on the distribution function. The collision integral is the source of difficulty in obtaining analytical or even numerical solutions of the Boltzmann equation. This term depends on the model of intermolecular potential, which is the way the particles interact during the collisions.

Equation (1.2) is therefore a non-linear integro-differential equation and describes the evolution of the distribution function in a state far from equilibrium thermodynamics. In the case where we have absolute thermodynamic equilibrium, the distribution function takes the form of the famous Maxwell equilibrium distribution, which is the solution of Eq. (1.2), without changes in time and space. The absolute Maxwellian is given by the relationship

$$f^{o}=\frac{n}{\left(2\pi R_{i}T\right)^{3/2}}exp\left[-\frac{\left(\xi_{x}-\hat{u}_{x}\right)^{2}+\left(\xi_{y}-\hat{u}_{y}\right)^{2}+\left(\xi_{z}-\hat{u}_{z}\right)^{2}}{2R_{i}T}\right] \tag{1.3}$$

where *n* the number density, *T* the temperature and *u* the macroscopic velocity vector, which is usually zero since we refer to absolute thermodynamic equilibrium conditions.

The Boltzmann equation is valid from the continuum flow regime to the free molecule flow. So, theoretically a direct Boltzmann solver which is valid in the whole range of Knudsen number can be developed if the numerical discretization is properly designed. In the framework of deterministic approximation, the most popular class of methods is based on the so called discrete velocity or discrete ordinates method of the Boltzmann equation [1]. These methods use regular discretization of particle velocity space. Most of these methods can give accurate numerical solution for high Knudsen number flows, such as those from the upper transition to the free molecule regime. However, in the continuum flow regime, the requirement of time step in these methods being less than the particle collision time makes them computationally intensive[13].

One of the outstanding numerical techniques available for solving the Boltzmann equation is the direct simulation Monte Carlo (DSMC) [14] method. The DSMC method is a widely used technique in the numerical prediction of low-density flows. However, in the continuum–transition regime, where the density is not low enough, the DSMC requires a large number of particles for accurate simulation, which makes the technique expensive in terms of both the computation time and the memory requirement. At present, the accurate modelling of realistic configurations, such as aerospace vehicles in 3D by the DSMC method for $Kn \ll 1$, is beyond the currently available computing power. The DSMC method requires that the time step and cell size are less than the particle collision time and mean free path, which subsequently introduce enormous computational cost in the high-density regime.

A more efficient approach is to solve relaxation-type kinetic equations, which are approximations of the Boltzmann equation, such as the Bhatnagar-Gross-Krook (BGK) equation [15], the Shakhov model [16] and the ellipsoidal statistical BGK model [17]. Many features of transitional flows are properly described by that sort of approximating equations.

1.3 Shock wave applications

The study of the internal structure of shock fronts is of interest for many reasons. At first this problem attracted attention as purely a theoretical one, the solution of which aided in understanding the physical mechanism of shock compression, as a truly remarkable phenomenon in gas dynamics. Later shock waves have been employed in laboratories with the aim of obtaining high temperatures and of studying various processes which take place in gases at high temperatures, as for example, vibrational excitation in molecules, molecular dissociation, chemical reactions, ionization, and radiation. Theoretical considerations of the shock front structure enable one to deduce from the experimental data a good deal of valuable information about the rates of these processes. Finally, the study of the structure of very strong shock fronts in which radiation plays an important role helps to clarify the problem of such an important characteristic as the luminosity of the shock front and makes it possible to explain some interesting optical effects observed in strong explosions in air.

In general, shock waves exist in many fields such as detonations, astrophysics, granular flows and aerospace engineering. Shock wave research has traditionally developed as an element of high-speed gas dynamics supporting supersonic flights and atmospheric reentry of space vehicles. For example, as a spacecraft re-enters the earth's atmosphere, it is traveling very much faster than the speed of sound. Typical low earth orbit re-entry speeds are near 17,500 mph and the Mach number is 25. The main characteristic of re-entry aerodynamics is that the temperature of the flow is so great that the chemical bonds of the diatomic molecules of the air are broken. The molecules break apart producing an electrically charged plasma around the aircraft and strong shock waves are generated on the lower surface of the spacecraft. Also, another valuable macroscopic quantity for the spacecraft re-entry is the heat flux in order to create adequate heat protection on the spacecraft surface [18]. Furthermore, recompression shocks appear when the flow over a transonic body is decelerated to subsonic speeds and are usually generated by transonic wings or turbines. The flow over the suction side of a transonic wing is accelerated to a supersonic speed and the resulting re-compression can be by either Prandtl-Meyer compression or by the formation of a normal shock. This shock is of particular interest to designers because it can cause separation of the boundary layer at the point where it touches the transonic profile. This can then lead to full separation and stall on the profile, higher drag, or shock-buffet, a condition where the separation and the shock interact in a resonance condition, causing resonating loads on the underlying structure [19].

Shock wave phenomena also exist in nature. Astrophysical environments feature many different types of shock waves. Some common examples are supernovae shock waves or blast waves travelling through the interstellar medium, the bow shock caused by the Earth's magnetic field colliding with the solar wind and shock waves caused by galaxies colliding with each other. Another interesting type of shock in astrophysics is the quasi-steady reverse shock or termination shock that terminates the ultra-relativistic wind from young pulsars [20].

Moreover, shock waves have been successfully applied to medical therapy. Extracorporeal shock wave lithotripsy (ESWL) has been a success in noninvasive removal of urinary tract stones. Recently, shock wave therapy has been further developed for the revascularization of cerebral embolism, drug delivery, and other interesting therapeutic methods. Meanwhile shock waves have been used in orthopedics and traumatology to treat insertion tendinitis, avascular necrosis of the head of femur and other necrotic bone alterations. Another field of shock wave application is the treatment of tendons, ligaments and bones on horses in veterinary medicine. The idea behind using shock wave therapy for orthopedic diseases is the stimulation of healing in tendons, surrounding tissue and bones. This is a completely different approach compared to urology where shock waves are used for disintegration [21].

1.4 Thesis objectives and outline

The present work has the following objectives:

(i) Solve the monatomic normal gas shock structure problem based on the BGK, S and ES kinetic modes using the discrete ordinate algorithm in a wide range of the Mach number and perform a comparison between the three models. Compute all bulk quantities of practical interest including shock thickness.

(ii) Validate the developed algorithm by a comparison with previous numerical results obtained by the DCMC and BE solvers and conclude which kinetic model is the most efficient one.

(iii) Compare the results with the experimental profiles in order to further demonstrate the validity and accuracy of the kinetic modeling approach.

(iv) Determine the range of validity of the classical Navier- Stokes approach in terms of the Mach number and estimate roughly the critical Mach number above which this approach fails.

The structure of the thesis is arranged as follows: Following the present in introduction, the shock structure and the problem formulation are described, by the hydrodynamic and the kinetic approach, in Chapter 2. Moreover, the Navier-Stokes distribution is acquired and the three kinetic models are presented along with the associated boundary conditions and macroscopic quantities. The numerical schemes for both approaches are reported in Chapter 3. In Chapter 4, extensive computational results are presented. In particular, macroscopic distributions for various Mach numbers including the shock thickness are provided. The comparison of kinetic models with DCMC and BE results as well as with measurements is performed. In addition, the range of validity of the NS approach is examined. Finally, in Chapter 5, a brief outline of the present work, followed by some concluding remarks and description of future work is presented.

Chapter 2

Problem description and formulation

2.1 Shock wave structure

Usually, changes in macroscopic parameters in regions of continuous flow occur very slowly in comparison with the rates of the relaxation processes which lead to the establishment of thermodynamic equilibrium. Each gas particle at any instant of time is in the state of thermodynamic equilibrium which corresponds to the slowly changing macroscopic variables, as though the particle "follows" the changes in the variables. Therefore, when considering shock discontinuities within the framework of the hydrodynamics of an ideal fluid, it is proper to assume the state of the gas on both sides of the discontinuity to be in equilibrium. The density, pressure, etc. change very rapidly in the thin transition layer, through which the gas passes from its initial state of thermodynamic equilibrium into its final, also equilibrium state. The thermodynamic equilibrium inside shock front can be appreciably disturbed. Therefore, in studying the internal structure of a shock front it is necessary to consider the kinetics of relaxation processes and to investigate in detail the mechanism of the establishment of the final state of thermodynamic equilibrium in the fluid which is attained behind the shock front.

The mathematical theory of shock front structure is based on the assumption that the structure is steady. The time it takes the fluid in a shock wave to go from the initial to the final state is very short, much shorter than the characteristic times over which the flow variables change in the continuous flow region behind the shock front. In exactly the same way, the front thickness is much less than the characteristic length scale over which the state of the gas behind the front changes significantly, for example, the distance from the shock front to the piston "pushing" the wave (the piston moves with a non-uniform speed, in general). In the short time during which the shock wave traverses a distance of the order of the front thickness, its propagation velocity, pressure, and the other flow variables behind the front remain practically unchanged. However, the kinetics of the internal processes which take place within a shock front propagating through a gas with given initial conditions depend only on the wave strength. Therefore over some relatively long period, each of the gas particles flowing into the shock discontinuity passes through the same sequence of states as the preceding ones. In other words, the distribution of the various variables across the shock front forms a "frozen" picture which moves during this period as an entity together with the front [20].

In the following sections the characteristic properties of the structure of shock fronts are considered in detail. The Rankine–Hugoniot conditions, also referred to as Rankine–Hugoniot relations, form the relationships between the states on both sides of a shock wave in a one-dimensional flow in fluids. They are named in recognition of the work carried out by Scottish engineer and physicist William John Macquorn Rankine and French engineer Pierre Henri Hugoniot and they are provided in Section 2.1.1. Another crucial parameter which can describe the shock profile well is the shock thickness that is explained in Section 2.1.2.

2.1.1 Rankine-Hugoniot (R-H) relations

In order to compute the shock structure, a propagating shock wave is considered in the rest frame of the shock. Un-shocked gas approaches from the $+x$ direction moving faster than its sound speed and passes through the shock.

Pre-shock conditions: ρ_1, u_1, T_1.

Post-shock conditions: $\rho_2 > \rho_1, u_2 < u_1, T_2 > T_1$.

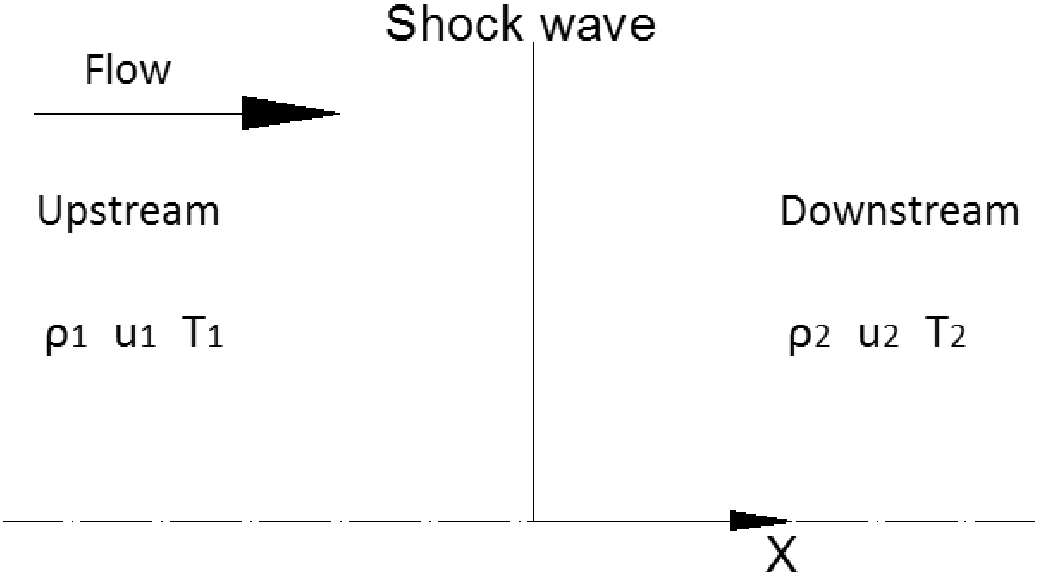

Figure 2.1: Notation

The relations ("jump conditions") between ρ_1, u_1, T_1 and ρ_2, u_2, T_2 are derived for a steady-state, plane-parallel shock. The velocity u is perpendicular to the shock front and the fluid properties depend only on the distance to the front [22]. Within the shock front, viscous effects are important. However, outside this layer, viscous effects are small on scales larger than the mean free path (MFP). The shock wave connects the equilibrium states for the density, velocity and temperature ρ_1, u_1, T_1 ahead of the shock at $x = -\infty$ and the equilibrium quantities ρ_2, u_2, T_2 behind the shock at $x = +\infty$.

The conservation equations are

$$\frac{d}{dx}Q(\rho,u,p)=0\Rightarrow Q(\rho,u,p)=constant \tag{2.1}$$

and although the quantities Q involve viscous terms, these can be ignored outside the shock zone and can therefore derive the jump conditions from equations that don't involve viscosity terms. The continuity, momentum equation, thermal energy and kinetic energy conservation equations are applied and the following assumptions are made: steady-state $\partial/\partial t=0$, plane-parallel $\partial/\partial z=0$, $\partial/\partial y=0$, $\partial/\partial x=d/dx$. Also, gravity and viscosity can be ignored. Hence, these equations become

$$\frac{d}{dx}(\rho u)=0 \tag{2.2.a}$$

$$\frac{du}{dx}=-\frac{1}{\rho}\frac{dP}{dx} \tag{2.2.b}$$

$$\frac{d}{dx}(\rho\varepsilon_i u)=-P\frac{du}{dx} \tag{2.2.c}$$

$$\frac{d}{dx}\left(\frac{1}{2}\rho u^2 u\right)=-u\frac{dP}{dx} \tag{2.2.d}$$

where ε_i is the specific internal energy of the fluid. Integrating the Eqs. (2.2), it is deduced that

$$\rho_1 u_1=\rho_2 u_2 \tag{2.3.a}$$

$$\rho_1 u_1^2+P_1=\rho_2 u_2^2+P_2 \tag{2.3.b}$$

$$\frac{1}{2}u_1^2+\frac{\gamma}{\gamma-1}\frac{P_1}{\rho_1}=\frac{1}{2}u_2^2+\frac{\gamma}{\gamma-1}\frac{P_2}{\rho_2} \tag{2.3.c}$$

Following some mathematical manipulation, the well-known Rankine-Hugoniot jump conditions are formed:

$$\frac{\rho_2}{\rho_1}=\frac{u_1}{u_2}=\frac{1+\frac{(\gamma+1)}{(\gamma-1)}\frac{p_1}{p_2}}{\frac{(\gamma+1)}{(\gamma-1)}+\frac{p_2}{p_1}} \tag{2.4}$$

Even though the physics of the shock region may be complicated, these conditions follow only from conservation of mass, momentum, and energy without involving any advanced treatment. They inter-relate the ratios of density, pressure and velocity across a shock wave.

The dimensionless number that characterizes the strength of a shock is the Mach number defined as the ratio of the shock speed to the upstream sound speed:

$$M_1=\frac{u_1}{a_1}=\sqrt{\frac{\rho_1 u_1^2}{\gamma p_1}} \tag{2.5}$$

The factor in the square root can be viewed as a ratio of "ram pressure" to thermal pressure in the pre-shock gas, or as a ratio of kinetic energy density to thermal energy density. A further manipulation of the R-H relations yields

$$u_1 u_2 = a_*^2 \tag{2.6.a}$$

$$\frac{a_*^2}{u_1^2} = 2\frac{(\gamma-1)}{(\gamma+1)}\left[\frac{1}{2}+\frac{1}{M_1^2(\gamma-1)}\right] \tag{2.6.b}$$

Equation (2.6.a) is called the Prantdl or Meyer relation with the subscript * denoting the sonic condition. Also, Eq. (2.6.b) is derived from the energy equation involving the upstream conditions and the sonic conditions. Hence, the shock jump conditions are expressed as

$$\frac{\rho_2}{\rho_1} = \frac{u_1}{u_2} = \frac{(\gamma+1)M_1^2}{(\gamma-1)M_1^2+2} \tag{2.7.a}$$

$$\frac{p_2}{p_1} = \frac{2\gamma M_1^2-(\gamma-1)}{\gamma+1} \tag{2.7.b}$$

Together these conditions imply

$$\frac{T_2}{T_1} = \frac{\left[2\gamma M_1^2-(\gamma-1)\right]\left[2+M_1^2(\gamma-1)\right]}{(\gamma+1)^2 M_1^2} \tag{2.7.c}$$

Equations (2.7) are very useful because they provide the macroscopic ratios in terms only of the upstream Mach number.

2.1.2 Shock thickness

One of the main parameters which can well describe the shock profile is the shock thickness. It is defined as the maximum slope of the density profile given by

$$\delta = \frac{\rho_2-\rho_1}{(d\rho/dx)_{max}} \tag{2.8}$$

In Fig. 2.2, this parameter is shown in dimensionless form as δ/λ_1 where λ_1 is the upstream mean free path along with the temperature and density distributions across the shock wave. Another quantity of some practical interest is the temperature-density separation denoted as Δ/λ_1 and defined as the distance between the two points at which $\tau = 0.5$ and $\rho = 0.5$ respectively.

It is evident from that the order of magnitude of the front thickness is

$$\delta \sim \lambda_1 \frac{M_1}{M_1^2-1} \tag{2.9}$$

Also, from the definition of the Knudsen number it is deduced that

$$Kn = \frac{\lambda_1}{\delta} = \frac{\lambda_1}{\dfrac{\rho_2-\rho_1}{(d\rho/dx)_{max}}} \tag{2.10}$$

Hence, it is obvious that the reciprocal shock thickness is the local Knudsen number.

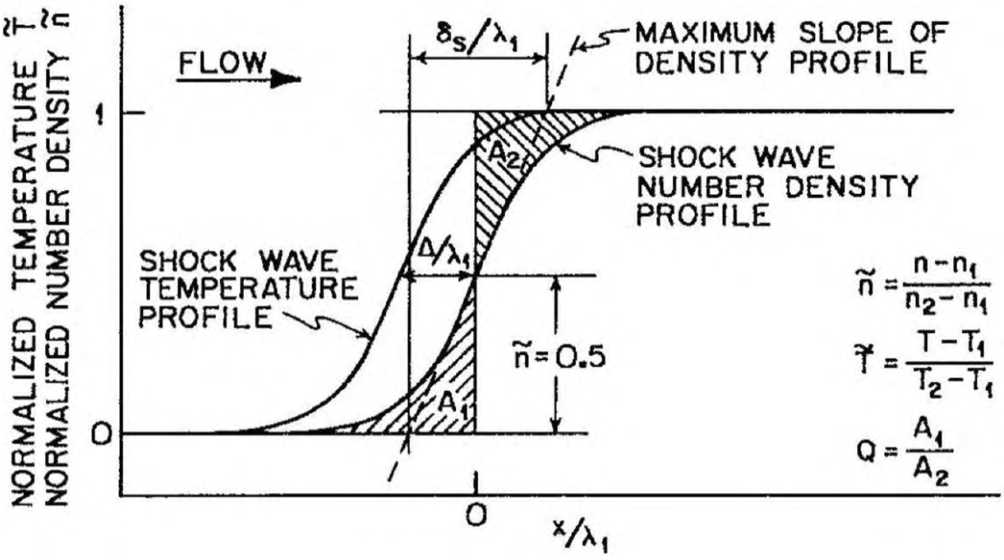

Figure 2.2: Shock thickness [12]

It has been found that Eq. (2.10) is valid only at small Mach numbers. A more precise definition of the Knudsen number in the case of high Mach numbers is reported by Macrossan [23] where

$$Kn = M_1 \frac{\lambda_1}{\dfrac{\rho_2 - \rho_1}{\left(d\rho / dx\right)_{max}}} \tag{2.11}$$

Exactly the same definition is given by Bird for high-speed expanding flows [14] where this quantity is also specified as the local “breakdown parameter”.

In a weak shock wave when $M_1 - 1 \ll 1$ the front thickness is given by $\delta \sim \lambda_1 / (M_1 - 1)$ and therefore can be equal to many molecular free paths. In the case when M_1=2, the front thickness is approximately equal to three molecular free paths λ_1 [24]. In the limiting case of a very strong wave ($M \to \infty$), the front thickness is given by $\delta \sim \lambda_1 / M_1 \to 0$, i.e., it tends to zero. The statement that the front thickness vanishes as the wave strength increases should not be taken literally. The fact is that when the front thickness becomes of the order of a mean free path, the hydrodynamic theory loses its meaning, since it is based on the assumption that the gradients are small or otherwise that the mean free path is small in comparison with the distance over which appreciable changes in the flow variables take place. Hence, the theory is simply inapplicable for sufficiently strong waves. It is evident physically that the thickness of the shock front for a wave of any strength cannot become smaller than the mean free path, since the gas molecules flowing into the discontinuity must make at least several collisions in order to scatter the directed momentum and to convert the kinetic energy of the directed motion into the kinetic energy of random motion (into heat). At the same time, the thickness of the shock front in the case of a strong wave cannot include many mean free paths, since the molecules of the incident stream loose, on the average, an appreciable fraction of their momentum during each collision.

The problem of the structure of strong shock fronts must be treated on the basis of the kinetic theory of gases. Hence, there are numerical studies that are concerned with the improvement of the simple theory presented above, by taking the dependence of the transport coefficients on temperature into account and by calculating the effect of the Prandtl number on the front structure. However, they do not contribute anything new in principle beyond the particular case considered above, and at best are of interest for the case of weak waves only.

2.2 Hydrodynamic approach

2.2.1 Governing equations

The steady one-dimensional compressible Navier-Stokes equations are given by [25]:

$$\frac{d}{dx}\begin{bmatrix} n\hat{u} \\ n\hat{u}^2 + \hat{p} - \hat{\sigma}_{xx} \\ n\hat{u}H - \hat{\sigma}_{xx}\hat{u} + \hat{q} \end{bmatrix} = 0 \tag{2.12}$$

where σ_{xx} is the *xx* component of the viscous stress tensor and q is the heat flux which are given by

$$\hat{\sigma}_{xx} = \frac{4}{3}\mu\frac{d\hat{u}}{d\hat{x}} \tag{2.13.a}$$

$$\hat{q} = -\frac{\gamma\mu}{Pr\left(\gamma - 1\right)}\frac{dT}{d\hat{x}} \tag{2.13.b}$$

Integrating the Eqs (2.12) results to

$$\begin{bmatrix} n\hat{u} \\ n\hat{u}^2 + \hat{p} - \hat{\sigma}_{xx} \\ n\hat{u}H - \hat{\sigma}_{xx}\hat{u} + \hat{q} \end{bmatrix} = \begin{bmatrix} C_1 \\ C_2 \\ C_3 \end{bmatrix} \tag{2.14}$$

Then, this set of equations is applied inside and outside the viscous shock to get

$$nu = nu_o = C_1 \tag{2.15.a}$$

$$n\hat{u}^2 + \hat{p} - \hat{\sigma}_{xx} = \left(n\hat{u}^2 + \hat{p}\right)_o = C_2 \tag{2.15.b}$$

$$\rho\hat{u}H - \sigma_{xx}\hat{u} + q = \left(n\hat{u}H\right)_o = C_3 \tag{2.15.c}$$

where the subscript *o* denotes the outside state, while the inside state has no subscript. However, since $\hat{\sigma}_{xx} = \hat{q} = 0$ outside the viscous shock where the solution is constant and since the right hand side terms are all constant Eqs. (2.15) may be further simplified. Equation (2.15.a) becomes $n\hat{u} = m$ and then is substituted into other Eqs. (2.15.b) and (2.15.c) to find that

$$\sigma_{xx} = m\hat{u} + \hat{p} - C_2 \tag{2.16.a}$$

$$q=\frac{1}{2}m\hat{u}^{2}-\frac{3}{2}n\hat{u}-C_{2}\hat{u}+C_{3} \tag{2.16.b}$$

These results are substituted back into Eqs. (2.13) to yield

$$\frac{d\hat{u}}{dx}=\frac{3}{4\mu}\left(m\hat{u}+\hat{p}-C_{2}\right) \tag{2.17.a}$$

$$\frac{dT}{dx}=\frac{2\,Pr}{5\mu}\left(\frac{1}{2}m\hat{u}^{2}-\frac{3}{2}Tm-C_{2}\hat{u}+C_{3}\right) \tag{2.17.b}$$

It is convenient to introduce the following dimensionless quantities:

$$\tau=\frac{T}{T_1},\rho=\frac{n}{n_1},u=\frac{\hat{u}_x}{\sqrt{2R_iT_1}},p=\frac{\hat{p}}{p_1},q=\frac{\hat{q}}{\sqrt{2R_iT_1}\,p_1} \tag{2.18.a}$$

$$c_x=\frac{\xi_x}{\sqrt{2R_iT_1}},\lambda_1=\frac{16}{5}\frac{\mu_1}{n_1\sqrt{2\pi RT_1}},\ x=\frac{\hat{x}}{\lambda_1},\ \frac{\mu(T_1)}{\mu(T)}=\left(\frac{T_1}{T}\right)^{\omega} \tag{2.18.b}$$

Therefore, Eqs. (2.17) can be written as

$$\frac{du}{dx}=\frac{6}{5\sqrt{\pi}}\tau^{1-\omega}\left(C_1\,u+\frac{\tau\,C_1}{u}-C_2\right) \tag{2.19.a}$$

$$\frac{d\tau}{dx}=-\frac{32\,Pr}{25\sqrt{\pi}}\tau^{1-\omega}\left(\frac{C_1\,u^2}{2}-\frac{3\,C_1\,\tau}{2}+C_3-u\,C_2\right) \tag{2.19.b}$$

This is a system of nonlinear ordinary differential equations (ODE) for u and τ (the viscosity μ depends on τ).

To integrate the system, the Mach number M_1 is chosen on the left side of the shock and the left and right states are set up as follows:

$$\rho_1=1,\ u_1=\sqrt{\frac{5}{6}}M_1,T_1=1,\ p_1=1 \tag{2.20.a}$$

$$\rho_2=\frac{(\gamma+1)M_1^2}{(\gamma-1)M_1^2+2},\ u_2=\frac{\rho_1 M_1}{\rho_2} \tag{2.20.b}$$

$$\frac{T_2}{T_1}=\frac{\left[2\gamma M_1^2-(\gamma-1)\right]\left[2+M_1^2(\gamma-1)\right]}{(\gamma+1)^2 M_1^2},\ p_2=\frac{1}{\gamma}\left[1+\frac{2\gamma}{(\gamma+1)}\left(M_1^2-1\right)\right] \tag{2.20.c}$$

All variables are in dimensionless form. Also, the constants in Eqs. (2.19) are computed by the left (or the right) state as

$$C_1=m=\rho_1 u_1 \tag{2.21.a}$$

$$C_2=\rho_1 u_1^2+p_1 \tag{2.21.b}$$

$$C_3=u_1\left(\frac{\gamma p_1}{\gamma-1}+\frac{1}{2}\rho_1 u_1^2\right) \tag{2.21.c}$$

The NS solution is based on the numerical integration of Eqs. (2.19) subject to the upstream and downstream conditions (2.20) and it is performed by a 4th order Runge-Kutta scheme.

2.2.2 Navier- Stokes distribution

In order to identify the reasons that Navier- Stokes equations cannot capture the shock thickness above a certain Mach number, the NS distribution function is defined and computed [26]. It is given by

$$f^{NS} = f^{M}\left[1-\frac{\hat{\sigma}_{ij}}{\hat{p}}\frac{\left(\xi_i-\hat{u}_i\right)\left(\xi_j-\hat{u}_j\right)}{2RT}-\frac{\hat{q}\left(\xi_x-\hat{u}_x\right)}{\hat{p}RT}\left(1-\frac{2}{5}\frac{\left(\xi_x-\hat{u}_x\right)^2+\xi_y{}^2+\xi_z{}^2}{RT}\right)\right] \tag{2.22}$$

where

$$f^{M} = \frac{n}{\left(2\pi R_i T\right)^{3/2}}exp\left[-\frac{\left(\xi_x-\hat{u}_x\right)^2+\xi_y^2+\xi_z^2}{2R_iT}\right] \tag{2.23}$$

The non-dimensional parameters in Eq. (2.18) are used plus the dimensionless distribution

$$g=\frac{f\left(\sqrt{2R_iT_1}\right)^3}{n_1} \tag{2.24}$$

Then, Eq. (2.22) reads as

$$g^{NS} = g^{M}\left[1-\frac{\sigma_{ij}\left(c_i-u_i\right)\left(c_j-u_j\right)}{p\tau}-\frac{2q\left(c_x-u_x\right)}{p\tau}\left(1-\frac{4}{5}\frac{\left(c_x-u_x\right)^2+c_y{}^2+c_z{}^2}{\tau}\right)\right] \tag{2.25}$$

with

$$g^{M} = \frac{\rho}{\pi^{3/2}\tau^{3/2}}exp\left[-\frac{\left(c_x-u_x\right)^2+c_y^2+c_z^2}{\tau}\right] \tag{2.26}$$

Next, the projection procedure, (described in the next section) is applied in order to eliminate the molecular velocities in the y and z direction. The reduced distribution functions are

$$Y(x,c_x)=\int_{-\infty}^{\infty}\int_{-\infty}^{\infty} g\left(x,\xi_x,\xi_y,\xi_z\right)d\xi_y d\xi_z \tag{2.27.a}$$

$$\Phi(x,c_x)=\int_{-\infty}^{\infty}\int_{-\infty}^{\infty}\left(\xi_y^2+\xi_z^2\right) g\left(x,\xi_x,\xi_y,\xi_z\right)d\xi_y d\xi_z \tag{2.27.b}$$

Following the detailed derivation presented in the Appendix 1 it is deduced that

$$Y^{NS}=Y^{M}\left[1-\left(\frac{\sigma_{zz}+\sigma_{yy}}{2p}+\frac{\sigma_{xx}\left(c_x-u_x\right)^2}{p}\right)-\frac{2q_x\left(c_x-u_x\right)}{5p\tau}\left(-4\left(c_x-u_x\right)^2+\tau\right)\right] \tag{2.28}$$

where

$$Y^{M}=\frac{\rho}{\sqrt{\pi\tau}}exp\left[-\frac{\left(c_x-u_x\right)^2}{\tau}\right] \tag{2.29}$$

and

$$\Phi^{NS}=\Phi^{M}\left[1-\left(\frac{\sigma_{zz}+\sigma_{yy}}{p}+\frac{\sigma_{xx}\left(c_x-u_x\right)^2}{p\tau}\right)+\frac{2q_x\left(c_x-u_x\right)}{5p\sqrt{\tau}}\left(4\left(c_x-u_x\right)^2+3\tau\right)\right] \tag{2.30}$$

where

$$\Phi^M = \frac{\rho\sqrt{\tau}}{\sqrt{\pi}} exp\left[-\frac{\left(c_x - u_x\right)^2}{\tau}\right] \tag{2.31}$$

Once the NS solution is recovered by solving Eq. (2.19) it is possible to substitute the computed bulk quantities into Eqs (2.28) and (2.30) to deduce the NS distribution functions which will be compared with the corresponding kinetic ones to investigate the differences at a mesoscale level.

2.3 Kinetic models

2.3.1 General form

The governing equations for all three kinetic models can all be written in the following one-dimensional form

$$\frac{\partial f}{\partial t} + \xi_x \frac{\partial f}{\partial x} = v\left(f^{eq} - f\right) \tag{2.32}$$

where f the distribution function, f^{eq} the equilibrium distribution function, and v the collision frequency. The Maxwell distribution f^M, is expressed as

$$f^M = \frac{n}{\left(2\pi R_i T\right)^{3/2}} exp\left[-\frac{\left(\xi_x - \hat{u}_x\right)^2 + \xi_y^2 + \xi_z^2}{2R_i T}\right] \tag{2.33}$$

Assuming steady-state conditions Eq. (2.32) is rewritten as

$$\xi_x \frac{\partial f}{\partial x} = v\left(f^{eq} - f\right) \tag{2.34}$$

In addition, the viscosity is proportional to temperature according to the inverse power law

$$\frac{\mu\left(T_1\right)}{\mu\left(T\right)} = \left(\frac{T_1}{T}\right)^{\omega} \tag{2.35}$$

Hence, the collision frequency can be deduced to

$$v = \frac{P}{\mu} = \frac{nRT}{\mu} = \frac{nRT_1}{\mu_1}\frac{n}{n_1}\frac{T}{T_1}\left(\frac{T_1}{T}\right)^{\omega} = \frac{nRT_1}{\mu_1}\frac{n}{n_1}\left(\frac{T_1}{T}\right)^{\omega} \tag{2.36}$$

and Eq. (2.34) is written as

$$\xi_x \frac{\partial f}{\partial x} = \frac{p_1}{\mu_1}\frac{n}{n_1}\left(\frac{T}{T_1}\right)^{1-\omega}\left(f^{eq} - f\right) \tag{2.37}$$

by $R = k_B / m$. Based on the same non- dimensionalization as above yields

$$c_x \frac{\partial g}{\partial x} = \frac{8}{5\sqrt{\pi}}\tau^{1-\omega}\rho\left(g^{eq} - g\right) \tag{2.38}$$

The applied projection procedure has been extensively used over the years in solving flow and heat transfer problems using kinetic equations. The main idea is to eliminate, depending upon the problem geometry and physics, one or two components of the molecular velocity vector and as a result to reduce significantly the required computational effort. This can be achieved through a formal mathematical procedure. The governing equations are integrated accordingly over the space of the appropriate component of the molecular velocity yielding a reduced set of equations, which do not include the component of the molecular velocity upon which the integration has been performed. Hence, the system of equations is reduced into two functions that depend only on x and c_x. The two functions Y and Φ are

$$Y(x,c_x) = \int_{-\infty}^{\infty}\int_{-\infty}^{\infty} g\left(x,\xi_x,\xi_y,\xi_z\right) d\xi_y d\xi_z \tag{2.39.a}$$

$$\Phi(x,c_x) = \int_{-\infty}^{\infty}\int_{-\infty}^{\infty} \left(\xi_y^2+\xi_z^2\right) g\left(x,\xi_x,\xi_y,\xi_z\right) d\xi_y d\xi_z \tag{2.39.b}$$

and they obey the following transports equations:

$$c_x \frac{\partial Y}{\partial x} = \frac{8}{5\sqrt{\pi}} \tau^{1-\omega} \rho\left(Y^{eq}-Y\right) \tag{2.40.a}$$

$$c_x \frac{\partial \Phi}{\partial x} = \frac{8}{5\sqrt{\pi}} \tau^{1-\omega} \rho\left(\Phi^{eq}-\Phi\right) \tag{2.40.b}$$

In the next sections the corresponding equilibrium distributions for each model are formulated.

2.3.2 The BGK model

The steady-state 1D Bhatnagar-Gross-Krook (BGK) model is described by

$$\xi_x \frac{\partial f}{\partial x} = v\left(f\left(n,\hat{u},T\right) - f\left(t,\hat{r},\xi\right)\right) \tag{2.41}$$

where f the distribution function, f^M the local Maxwellian and v the collision frequency. The local equilibrium distribution f^{eq}, is expressed as

$$f^{eq} = f^M = \frac{n}{\left(2\pi R_i T\right)^{3/2}} exp\left[-\frac{\left(\xi_x-\hat{u}_x\right)^2+\xi_y^2+\xi_z^2}{2R_i T}\right] \tag{2.42}$$

This model constitutes the simplest possible approach of the collision term and the basis upon which other more advanced subsequent models have been developed. The equilibrium distribution function for the BGK model is

$$g^{eq} = \frac{\rho}{\pi^{3/2}\tau^{3/2}} exp\left[-\frac{\left(c_x-u_x\right)^2+c_y^2+c_z^2}{\tau}\right] \tag{2.43}$$

while after the projections, the reduced distribution functions become

$$Y^{eq} = \frac{\rho}{\sqrt{\pi\tau}} exp\left[-\frac{\left(c_x-u_x\right)^2}{\tau}\right] \tag{2.44.a}$$

$$\Phi^{eq} = \frac{\tau^{1/2}\rho}{\sqrt{\pi}} exp\left[-\frac{\left(c_x-u_x\right)^2}{\tau}\right] \tag{2.44.b}$$

As it is well known the BGK model is a reliable model mainly for isothermal flows.

2.3.3 The Shakhov (S) model

An improved version, has been presented in 1974 by Shakhov, known as the S model. The steady-state 1D S model is described by the equation

$$\xi_x \frac{\partial f}{\partial x} = \frac{P}{\mu}\left\{ f^{eq}\left[1+\frac{2m}{15n\left(k_B T\right)^2} q\left(\xi-u\right)\left(\frac{m\left(\xi-u\right)^2}{2k_B T}-\frac{5}{2}\right)\right]-f\right\} \tag{2.45}$$

The diversification of the BGK model presented in the distribution equilibrium which now includes the heat flux terms, making possible the export of results with sufficient precision for non-isothermal flows. The Shakhov model is capable to estimate simultaneously both the transport coefficients of viscosity and thermal conductivity correctly, yielding the correct Prandtl number of 2/3 for monatomic gases (the BGK yields the wrong Prandtl number of 1). The equilibrium distribution for the S model is

$$g^{eq} = \frac{\rho}{\pi^{3/2}\tau^{3/2}} exp\left[-\frac{\left(c_x-u_x\right)^2+c_y^2+c_z^2}{\tau}\right]\left[1+\frac{2}{15}\frac{q_x\left(c_x-u_x\right)}{\rho\tau^2}\left(\frac{2\left(c_x-u_x\right)^2}{\tau}-5\right)\right] \tag{2.46}$$

while after the projections, the reduced distribution functions become

$$Y^{eq} = \frac{\rho}{\sqrt{\pi\tau}} exp\left[-\frac{\left(c_x-u_x\right)^2}{\tau}\right]\left[1+\frac{2}{15}\frac{q_x\left(c_x-u_x\right)}{\rho\tau^2}\left(\frac{2\left(c_x-u_x\right)^2}{\tau}-3\right)\right] \tag{2.47.a}$$

$$\Phi^{eq} = \frac{\tau^{1/2}\rho}{\sqrt{\pi}} exp\left[-\frac{\left(c_x-u_x\right)^2}{\tau}\right]\left[1+\frac{2}{15}\frac{q_x\left(c_x-u_x\right)}{\rho\tau^2}\left(\frac{2\left(c_x-u_x\right)^2}{\tau}-1\right)\right] \tag{2.47.b}$$

2.3.4 The ellipsoidal statistical (ES) model

The steady-state 1D ES model is described by the equation

$$\xi_x \frac{\partial f}{\partial x} = \frac{P}{\mu} Pr\left(f^{eq}-f\right) \tag{2.48}$$

with *f* being the distribution function and *v* is the collision frequency. By substituting *Pr=1* it can be seen that the BGK expression is retrieved. The characteristic value for monatomic gases, *Pr=2/3*, has been used in the following calculations. The collision term is retained in its non-linear form with

$$f^{eq} = \frac{n}{\left(2\pi\right)^{3/2}\sqrt{|\lambda|}} exp\left[-\sum_{i,j=1}^{3}\left(\xi_i-\hat{u}_i\right)\left(\xi_j-\hat{u}_j\right)\lambda_{ij}\right] \tag{2.49}$$

where

$$\lambda_{ij} = \left(1-\lambda\right)RT\,\delta_{ij} + \lambda\int_{-\infty}^{\infty}\int\int\sum_{i,j=1}^{3}\left(\xi_i-\hat{u}_i\right)\left(\xi_j-\hat{u}_j\right) f d^3\xi \tag{2.50}$$

Equation (2.49) for the present problem is written as

$$f^{eq}=\frac{n}{\left(2\pi\right)^{3/2}\sqrt{\lambda_{xx}}\lambda_{yy}}exp\left[-\frac{\left(\xi_x-\hat{u}_x\right)^2}{2\lambda_{xx}}-\frac{\xi_y^2+\xi_z^2}{2\lambda_{yy}}\right] \tag{2.51}$$

where

$$\lambda_{xx}=\left(1-\lambda\right)RT+\frac{\lambda}{mn}\int_{-\infty}^{\infty}\int\int\left(\hat{u}_x-\xi\right)^2 fd^3\xi \tag{2.52.a}$$

$$\lambda_{yy}=\left(1+\frac{1}{2}\lambda\right)RT-\frac{\lambda}{2mn}\int_{-\infty}^{\infty}\int\int\left(\hat{u}_x-\xi\right)^2 fd^3\xi \tag{2.52.b}$$

with $\lambda=\left(1-Pr\right)/Pr$.

In order to compute the parameter λ_{22} it has been considered that $\sigma_{zz}=\sigma_{yy}$. The other components of the stress tensor are all zero. The governing equations are slightly different in this model because they contains Prantdl number and are given by

$$c_x\frac{\partial g}{\partial x}=\frac{8}{5\sqrt{\pi}}\tau^{1-\omega}\rho Pr\left(g^{eq}-g\right) \tag{2.53.a}$$

$$c_x\frac{\partial Y}{\partial x}=\frac{8}{5\sqrt{\pi}}\tau^{1-\omega}\rho Pr\left(Y^{eq}-Y\right) \tag{2.53.b}$$

$$c_x\frac{\partial Y}{\partial x}=\frac{8}{5\sqrt{\pi}}\tau^{1-\omega}\rho Pr\left(\Phi^{eq}-\Phi\right) \tag{2.53.c}$$

The equilibrium distribution function for the ES model is

$$g^{eq}=\frac{\rho}{\pi^{3/2}\sqrt{k_{xx}}k_{yy}}exp\left[-\frac{\left(c_x-u_x\right)^2}{k_{xx}}-\frac{c_y^2+c_z^2}{k_{yy}}\right] \tag{2.54}$$

where

$$k_{\chi\chi}=\left(1-\lambda\right)\tau+\frac{\lambda}{\rho}\sigma_{\chi\chi} \tag{2.55.a}$$

$$k_{yy}=\left(1+\frac{1}{2}\lambda\right)\tau-\frac{\lambda}{2\rho}\sigma_{\chi\chi} \tag{2.55.b}$$

Finally, after the projections, the reduced distribution functions become

$$Y^{eq}=\frac{\rho}{\sqrt{\pi}\sqrt{k_{\chi\chi}}}exp\left[-\frac{\left(c_x-u_x\right)^2}{k_{\chi\chi}}\right] \tag{2.56.a}$$

$$\Phi^{eq}=\frac{\rho k_{yy}}{\sqrt{\pi}\sqrt{k_{\chi\chi}}}exp\left[-\frac{\left(c_x-u_x\right)^2}{k_{\chi\chi}}\right] \tag{2.56.b}$$

It is noted that the ES model has been originally formulated to tackle anisotropic problems such as shock waves. Also it possesses the advantages of the S model related to the correct estimation of the transport coefficients and the Prandtl number.

2.4 Boundary conditions

In order to close the problem, the upstream and downstream boundary conditions must be defined. Since far upstream and downstream equilibrium conditions are assumed the corresponding distributions are Maxwellians given by:

$$f_1 = \frac{n_1}{\left(2\pi R_i T_1\right)^{3/2}} exp\left[-\frac{\left(\xi_x - u_{x1}\right)^2 + \xi_y^2 + \xi_z^2}{2R_i T_1}\right] \tag{2.57.a}$$

$$f_2 = \frac{n_2}{\left(2\pi R_i T_2\right)^{3/2}} exp\left[-\frac{\left(\xi_x - u_{x2}\right)^2 + \xi_y^2 + \xi_z^2}{2R_i T_2}\right] \tag{2.57.b}$$

In dimensionless form they are written as

$$g_1 = \frac{\rho_1}{\left(\pi\tau_1\right)^{3/2}} exp\left[-\frac{\left(c_x - u_{x1}\right)^2 + c_y^2 + c_z^2}{\tau_1}\right] \tag{2.58.b}$$

$$g_2 = \frac{\rho_2}{\left(\pi\tau_2\right)^{3/2}} exp\left[-\frac{\left(c_x - u_{x2}\right)^2 + c_y^2 + c_z^2}{\tau_2}\right] \tag{2.58.a}$$

After applying the projection procedure, the reduced distribution functions become

$$Y_2 = \frac{\rho_2}{\sqrt{\pi\tau_2}} exp\left[-\frac{\left(c_x - u_{x2}\right)^2}{\tau_2}\right] \tag{2.59.a}$$

$$\Phi_2 = \frac{\rho_2\sqrt{\tau_2}}{\sqrt{\pi}} exp\left[-\frac{\left(c_x - u_{x2}\right)^2}{\tau_2}\right] \tag{2.59.b}$$

$$Y_1 = \Phi_1 = \frac{1}{\sqrt{\pi}} exp\left[-\frac{\left(c_x - u_{x2}\right)^2}{\tau_2}\right] \tag{2.59.c}$$

It is obvious that the number density, temperature and the velocity are needed in order to compute the boundary conditions. At $x = -\infty$ the dimensionless bulk quantities are:

$$u_1\left(x = -\infty\right) = \frac{\hat{u}_x}{\sqrt{2R_i T_1}} = M_1 \frac{\sqrt{\gamma R_i T_1}}{\sqrt{2R_i T_1}} = \sqrt{\frac{\gamma}{2}} M_1 = \sqrt{\frac{5}{6}} M_1 \tag{2.60.a}$$

$$\rho_1 = 1 \quad \tau_1 = 1 \tag{2.60.b}$$

At $x = +\infty$ the Rankine- Hugoniot relations are used to find

$$\rho_2 = \frac{\left(\gamma + 1\right) M_1^2}{\left(\gamma - 1\right) M_1^2 + 2} \tag{2.61.a}$$

$$\hat{u}_1 n_1 = \hat{u}_2 n_2 \rightarrow u_2 = \frac{u_1}{\rho_2} = \frac{\sqrt{\gamma}\left(2 + \left(\gamma - 1\right) M_1^2\right)}{\sqrt{2}\left(\gamma + 1\right) M_1} \tag{2.61.b}$$

$$\tau_2 = \frac{\left(2 + \left(\gamma - 1\right) M_1^2\right)\left(2\gamma M_1^2 - \left(\gamma - 1\right)\right)}{\left(\gamma + 1\right)^2 M_1^2} \tag{2.61.c}$$

Equations (2.60) and (2.61) are employed to close the problem and to compute the kinetic solution.

2.5 Macroscopic quantities

Following the computation of the reduced distribution functions, the macroscopic distributions are evaluated. They include the number density, the velocity, the total temperature as well as its components namely the parallel and perpendicular temperatures, the stress tensor and the heat flux. The detailed derivation is given in Appendix B, while here only the definitions are provided:

Number density:

$$\rho(x)=\int_{-\infty}^{+\infty} Y\left(x,c_x\right)dc_x \tag{2.62}$$

Velocity:

$$u_x(x)=\frac{1}{\rho}\int_{-\infty}^{+\infty} c_x Y\left(x,c_x\right)dc_x \tag{2.63}$$

Temperature:

$$\tau(x)=\frac{2}{3\rho}\int_{-\infty}^{+\infty}\left(c_x-u_x\right)^2 Y\left(x,c_x\right)+\Phi\left(x,c_x\right)dc_x \tag{2.64}$$

Parallel temperature:

$$\tau_{//}(x)=\frac{2}{3\rho}\int_{-\infty}^{+\infty}\left(c_x-u_x\right)^2 Y\left(x,c_x\right)dc_x \tag{2.65}$$

Perpendicular temperature:

$$\tau_{\perp}(x)=\frac{2}{3\rho}\int_{-\infty}^{+\infty}\Phi\left(x,c_x\right)dc_x \tag{2.66}$$

Heat flux:

$$q_x=\int_{-\infty}^{+\infty}\left[\left[c_x^3-u_x^3-\left(3c_x u_x^2+3c_x^2 u_x\right)\right]Y\left(x,c_x\right)+\left(c_x-u_x\right)\Phi\left(x,c_x\right)\right]dc_x \tag{2.67}$$

Parallel stress:

$$\sigma_{//}=\sigma_{xx}=\int_{-\infty}^{+\infty}\left(c_x-u_x\right)^2 Y\left(x,c_x\right)dc_x \tag{2.68}$$

Perpendicular stress:

$$\sigma_{\perp}=\sigma_{yy}+\sigma_{zz}=\int_{-\infty}^{+\infty}\Phi\left(x,c_x\right)dc_x \tag{2.69}$$

2.6 The variable hard sphere (VHS) model

A molecular model is established through the definition of the intermolecular potential φ which is related to the spherically symmetric force F between the molecules. The force F is strongly repulsive at short distances and weakly attractive at larger distances. In general, the simplest acceptable model is chosen and in most cases the attractive component is neglected.

Here, the variable hard sphere model introduced by Bird [27] is applied. This is a hard sphere molecule with a diameter d that is a function if the relative velocity c_r. In the variable hard sphere (VHS) model it is assumed that

$$d = d_{ref} \left(c_{r,ref} / c_r \right)^{\omega} \tag{2.70}$$

where the subscript *ref* denotes reference values and the exponent ω is a parameter. It is easily proved that the variation of viscosity with temperature is the same as that in the inverse power law (IPL). It was mentioned before that the inverse power law is used, so the viscosity takes the same form just with an adjustment of the exponent ω.

$$\mu \propto T^{\omega} \tag{2.71}$$

where

$$\omega = \frac{1}{2} \frac{(n+3)}{(n-1)} \tag{2.72}$$

and n is exponent of the intermolecular force law that is usually used with DCMC method.

The hard sphere (HS) and the Maxwell (M) intermolecular potential models are the two limiting cases of the VHS or the IPL model. As it has been pointed out by setting the parameter $\omega=0.5$ (or $n=\infty$) the hard sphere model is obtained, while by setting $\omega=1$ (or $n=5$) the Maxwell model is obtained. These limiting values correspond to theoretical gases, while in real gases the parameter ω varies as $0.5 \le \omega \le 1$.

Chapter 3

Computational methods

3.1 Numerical scheme of Navier-Stokes equations

The implemented solution is presented in Gilbard and Paolucci [28], while a more detailed description is given in the text by Masatsuka [25].

A one-dimensional grid is defined by the set of nodes $\{x_k\} = x_1, x_2, x_3, \ldots x_N$, where N is the total number of nodes in the grid. The system is integrated from the downstream area and it begins from x_N to x_{N-1} with the initial values: $u(x_N) = u_2 + \varepsilon$ where ε is a small number (e.g., $\varepsilon = 1 \times 10^{-10}$) and $\tau(x_N) = \tau_2$ with a very small step δx compared with $x_N - x_{N-1}$. Then, the same procedure is applied between two adjacent nodes, k and $k-1$, where $k=N-1, \ldots 3, 2$, with the solutions at $x = x_k$ as the initial values. The classical fourth-order Runge-Kutta scheme [29] is applied with $\delta x = (x_k - x_{k-1}) / 1000$ between the two nodes, k and k−1. It is important that the last step in the integration between two nodes needs to be adjusted to finish exactly at $x_k = x_{k-1}$.

Moreover, the small number ϵ is essential to obtaining a meaningful solution. In fact, if $\varepsilon = 0$, the computation fails and the correct upstream state of the shock is not reached because the right hand side of the system (2.19) is exactly zero. Hence, the location of the shock depends on the magnitude of ϵ, but if ϵ is large enough (e.g., $\varepsilon = 0.1$), then the shock profile isn't computed properly in the downstream area. In addition, the correct transition to the upstream area is achieved through the constants C_1, C_2 and C_3 which are the equal for the downstream and upstream area due to the conservation of mass, momentum and energy.

In order to find the solution, it is necessary to integrate the ODE's (2.19.a) and (2.19.b) from $x=x_0$ to $x=x_i$ and find the velocity u_i and the temperature T_i at $x=x_i$. So, the ODE's are integrated from $x=x_0$ to $x=x_i$ in 1000 steps by the classical 4th order Runge-Kutta method. A trial step at the midpoint of an interval is used to cancel out lower-order error terms. The fourth-order formula is

$$
\begin{aligned}
x &= x + dx \\
K_1 &= V + \frac{1}{2} dx \times rhs(V) \\
K_2 &= V + \frac{1}{2} dx \times rhs(K_1) \\
K_3 &= V + \frac{1}{2} dx \times rhs(K_2) \\
V &= (K_1 + 2K_2 + K_3 - V)\frac{1}{3} + \frac{1}{6} dx \times rhs(K_3)
\end{aligned}
\tag{3.1}
$$

where the *rhs* is the right hand part of the Eqs. (2.19). Finally, when the ODE’s are solved, the following quantities are computed

$$u = u_i \tag{3.2.a}$$

$$\tau = \tau_i \tag{3.2.b}$$

$$\rho = C_1 / u \tag{3.2.c}$$

$$\sigma_{xx} = C_1 u + \frac{C_1 \tau}{u} - C_2 \tag{3.2.d}$$

$$q = \frac{1}{2} C_1 u^2 - \frac{C_1 \tau}{(\gamma - 1)} - C_2 u + C_3 \tag{3.2.e}$$

where the constants C_1, C_2, C_3 have been computed by the equations (2.21).

3.2 Numerical schemes of kinetic models

3.2.1 Iteration Procedure

Since the methodology is the same for all three kinetic models it is described based on the S model equations. To solve these equations an iterative procedure is applied between the kinetic equations and the associated moments of the distribution function which appear in the expressions of the equilibrium distribution. In order to minimize computational time, the open-mpi interface has been used.

The kinetic equations may be written as

$$c_x \frac{\partial Y^{k+1/2}}{\partial x} = \frac{8}{5\sqrt{\pi}} \tau^{1-\omega^k} \rho^k \left(Y^{eq^k} - Y^{k+1/2} \right) \tag{3.3.a}$$

$$\frac{\partial \Phi^{k+1/2}}{\partial x} = \frac{8}{5\sqrt{\pi}} \tau^{1-\omega^k} \rho^k \left(\Phi^{eq^k} - \Phi^{k+1/2} \right) \tag{3.3.b}$$

where Y^{eq}, Φ^{eq} are given by Eqs. (2.47.a, 2.47.β). The bulk quantities involved in the computations are

$$\rho^{k+1} = \int_{-\infty}^{+\infty} Y(x, c_x)^{k+1/2} dc_x \tag{3.4.a}$$

$$u_x^{k+1} = \frac{1}{\rho^{k+1}} \int_{-\infty}^{+\infty} c_x Y(x, c_x)^{k+1/2} \, dc_x \tag{3.4.b}$$

$$\tau^{k+1} = \frac{2}{3\rho^{k+1}} \int_{-\infty}^{+\infty} (c_x - u_x)^2 \, Y(x, c_x)^{k+1/2} + \Phi(x, c_x)^{k+1/2} \, dc_x \tag{3.4.c}$$

$$q_x^{k+1} = \int_{-\infty}^{+\infty} \left[\left[c_x^3 - u_x^{3\,k+1} - \left(3 c_x u_x^{2\,k+1} + 3 c_x^2 u_x^{k+1} \right) \right] Y(x, c_x)^{k+\frac{1}{2}} + \left(c_x - u_x^{k+1} \right) \Phi(x, c_x)^{k+\frac{1}{2}} \right] dc_x \tag{3.4.d}$$

The indexes *k*, *k+1/2* and *k+1* indicate the steps needed in the iteration process which is described as follows: The bulk quantities are known from the previous iteration. Thus, the equilibrium distributions Y^{eq}, Φ^{eq} are computed. Then, the kinetic equations are solved for the unknown distributions *Y*, *Φ*. Finally, updated estimates of the local macroscopic quantities are computed based on the moments of the distribution functions *Y*, *Φ*. This concludes one iteration. The iteration process is terminated when convergence is achieved. The code is parallel. The solution of the kinetic equations is performed in several CPUs. The results are transferred into a single CPU to compute the moments. The iteration procedure is explained graphically in Figure 3.1.

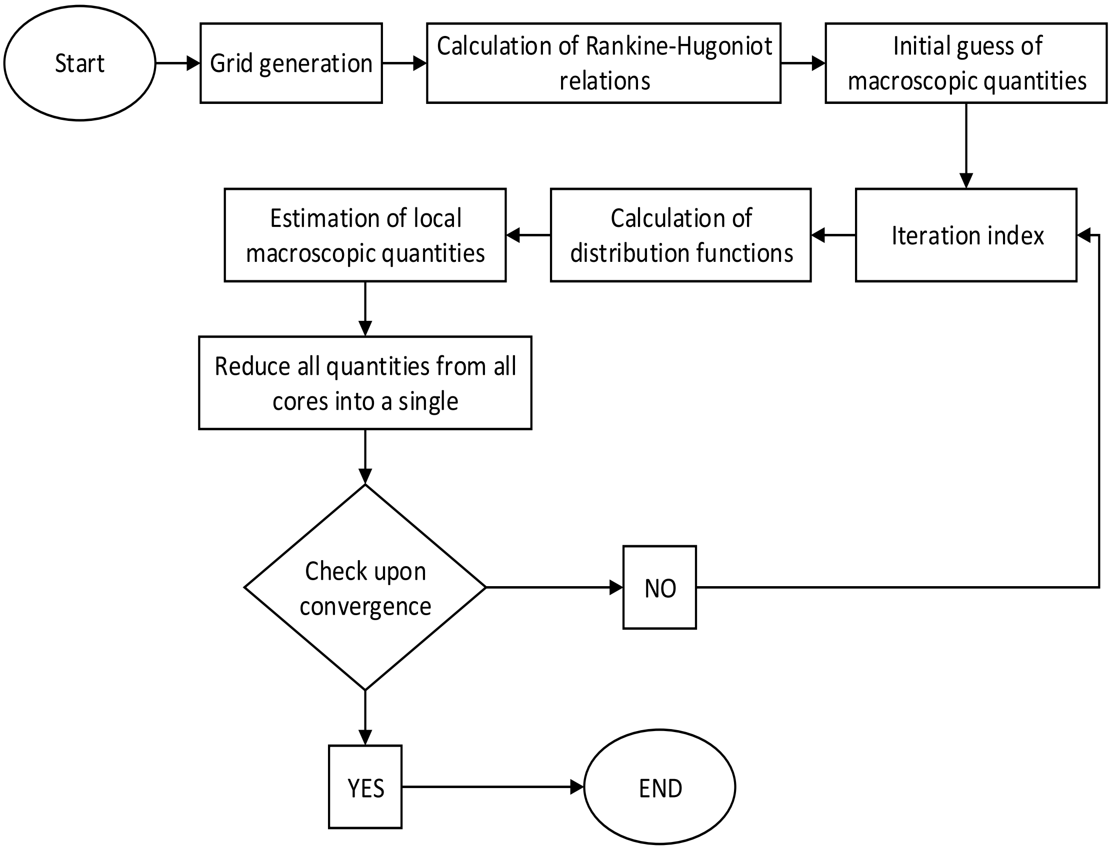

Figure 3.1: Flow chart of the algorithm

3.2.2 Discretization of in the physical and molecular space

A finite volume scheme [30] has been applied here for the discretization of the governing equations (2.40) in the physical space. Hence, the operator *A* is applied

$$A=\int_{x_i-\frac{\Delta\chi}{2}}^{x_i+\frac{\Delta\chi}{2}}(\ldots)\,dx \tag{3.5}$$

on Eq. (2.40) to yield

$$c_x\left[Y_{i+\frac{1}{2},m}-Y_{i-\frac{1}{2},m}\right]=\frac{8}{5\sqrt{\pi}}\frac{\Delta x}{2}\begin{bmatrix}\left(\tau^{1-\omega}\rho\right)_{i+\frac{1}{2},m}\left(Y^{M}_{i+\frac{1}{2},m}-Y_{i+\frac{1}{2},m}\right)\\ +\left(\tau^{1-\omega}\rho\right)_{i-\frac{1}{2},m}\left(Y^{M}_{i-\frac{1}{2},m}-Y_{i-\frac{1}{2},m}\right)\end{bmatrix} \tag{3.6}$$

By setting

$$Y^{+}=Y_{i+\frac{1}{2},m},Y^{-}=Y_{i-\frac{1}{2},m} \tag{3.7}$$

the equations are transformed into

$$\frac{c_x}{\Delta x}\left[Y^{+}_{i+\frac{1}{2},m}-Y^{-}_{i-\frac{1}{2},m}\right]=\frac{4\left(\tau^{1-\omega}\rho\right)_{i+\frac{1}{2},m}}{\sqrt{\pi}}Y^{M,+}-\frac{4\left(\tau^{1-\omega}\rho\right)_{i-\frac{1}{2},m}}{\sqrt{\pi}}Y^{+}$$

$$+\frac{4\left(\tau^{1-\omega}\rho\right)_{i+\frac{1}{2},m}}{\sqrt{\pi}}Y^{M,-}-\frac{4\left(\tau^{1-\omega}\rho\right)_{i-\frac{1}{2},m}}{\sqrt{\pi}}Y^{-}\Rightarrow$$

$$Y^{-}\left[\frac{c_x}{\Delta x}-\frac{4\left(\tau^{1-\omega}\rho\right)_{i-\frac{1}{2},m}}{\sqrt{\pi}}\right]=Y^{+}_{i}\left[\frac{c_x}{\Delta x}+\frac{4\left(\tau^{1-\omega}\rho\right)_{i+\frac{1}{2},m}}{\sqrt{\pi}}\right]$$

$$-\frac{4\left(\tau^{1-\omega}\rho\right)_{i+\frac{1}{2},m}}{\sqrt{\pi}}Y^{M,+}-\frac{4\left(\tau^{1-\omega}\rho\right)_{i-\frac{1}{2},m}}{\sqrt{\pi}}Y^{M,-}\Rightarrow$$

The discretized equations are rewritten for negative and positive velocities:

- for negative velocities $c_x < 0$

$$Y_{i-\frac{1}{2},m}=\frac{Td_1}{Td_2}Y_{i+\frac{1}{2},m}-\frac{Td_3}{Td_2}Y^{M}_{i+\frac{1}{2},m}-\frac{Td_4}{Td_2}Y^{M}_{i-\frac{1}{2},m} \tag{3.8.a}$$

$$\Phi_{i-\frac{1}{2},m}=\frac{Td_1}{Td_2}\Phi_{i+\frac{1}{2},m}-\frac{Td_3}{Td_2}\Phi^{M}_{i+\frac{1}{2},m}-\frac{Td_4}{Td_2}\Phi^{M}_{i-\frac{1}{2},m} \tag{3.8.b}$$

- for positive velocities $c_x > 0$

$$Y_{i+\frac{1}{2},m}=\frac{Td_2}{Td_1}Y_{i-\frac{1}{2},m}+\frac{Td_3}{Td_1}Y^{M}_{i+\frac{1}{2},m}+\frac{Td_4}{Td_1}Y^{M}_{i-\frac{1}{2},m} \tag{3.9.a}$$

$$\Phi_{i+\frac{1}{2},m}=\frac{Td_2}{Td_1}\Phi_{i-\frac{1}{2},m}+\frac{Td_3}{Td_1}\Phi^{M}_{i+\frac{1}{2},m}+\frac{Td_4}{Td_1}\Phi^{M}_{i-\frac{1}{2},m} \tag{3.9.b}$$

Here, the following definitions have been introduced:

$$Td_1=\frac{c_x}{\Delta x}+\frac{4\left(\tau^{1-\omega}\rho\right)_{i+\frac{1}{2},m}}{5\sqrt{\pi}},\ Td_2=\frac{c_x}{\Delta x}-\frac{4\left(\tau^{1-\omega}\rho\right)_{i-\frac{1}{2},m}}{5\sqrt{\pi}} \tag{3.10.a}$$

$$Td_3=\frac{4\left(\tau^{1-\omega}\rho\right)_{i+\frac{1}{2},m}}{5\sqrt{\pi}},\ Td_4=\frac{4\left(\tau^{1-\omega}\rho\right)_{i-\frac{1}{2},m}}{5\sqrt{\pi}} \tag{3.10.b}$$

$$Y^{M}_{i,m}=\frac{\rho_i}{\sqrt{\tau_i\pi}}exp\left[-\frac{\left(c_x-u_{x,i}\right)^2}{\tau_i}\right],\Phi^{M}_{i,m}=\frac{\rho_i}{\sqrt{\tau_i\pi}}exp\left[-\frac{\left(c_x-u_{x,i}\right)^2}{\tau_i}\right] \tag{3.11}$$

3.2.3 Numerical Integration

After obtaining the values of *Y* and *Φ*, it is necessary to integrate over the velocity space to obtain the macroscopic quantities needed for the next iteration. This is achieved by using the simple trapezoidal rule which is a 3rd order scheme technique for approximating the definite integral

$$\int_a^b f(x)dx \tag{3.12}$$

It is mentioned that using trapezoidal rule instead of Gauss–Legendre quadrature, which is considered as a more advanced numerical integration algorithm, is necessary because the computed distribution functions do not match with the Gauss distribution. Hence, using trapezoidal rule with a uniform grid it may require a denser grid but it is also safer from the computational point of view in catching the irregularities of the distribution function.

The velocity domain is discretized into N equally spaced segments, or $N+1$ grid points $a = x_1 < x_2 < \ldots < x_{N+1} = b$, where the grid spacing is $h=(b-a)/N$. The approximation to the integral becomes

$$\int_a^b f(x)dx = \frac{b-a}{2N}\left(f(x_1)+2f(x_2)+2f(x_3)+2f(x_4)+\ldots+2f(x_N)+f(x_{N+1})\right) \tag{3.13}$$

By applying the trapezoidal rule, the macroscopic distributions are estimated:

$$\rho = \sum_{i=1}^{m} Y(x,c_x)\, w\frac{\Delta x}{2} \tag{3.14}$$

$$u_x = \sum_{i=1}^{m} c_x Y(x,c_x)\, w\frac{\Delta x}{2} \tag{3.15}$$

$$\tau = \frac{2}{3\rho}\sum_{i=1}^{m}\left[(c_x-u_x)^2\, Y(x,c_x)+\Phi(x,c_x)\right] w\frac{\Delta x}{2} \tag{3.16}$$

$$\tau_{//}(x) = \frac{2}{3\rho}\sum_{i=1}^{m}\left[(c_x-u_x)^2\, Y(x,c_x)\right] w\frac{\Delta x}{2} \tag{3.17}$$

$$\tau_{\perp}(x) = \frac{2}{3\rho}\sum_{i=1}^{m}\left[\Phi(x,c_x)\right] w\frac{\Delta x}{2} \tag{3.18}$$

$$q = \sum_{i=1}^{m}\left[\left(c_x^3-u_x^3-\left(3c_x u_x^2+3c_x^2 u_x\right)\right) Y(x,c_x)+(c_x-u_x)\Phi(x,c_x)\right] w\frac{\Delta x}{2} \tag{3.19}$$

$$\sigma_{//} = \sigma_{xx} = \sum_{i=1}^{m}\left[(c_x-u_x)^2\, Y(x,c_x)\right] w\frac{\Delta x}{2} \tag{3.20}$$

$$\sigma_{\perp} = \sigma_{yy}+\sigma_{zz} = \sum_{i=1}^{m}\left[\Phi(x,c_x)\right] w\frac{\Delta x}{2} \tag{3.21}$$

Obtaining the correct result is achieved with two important parameters. Firstly, in the upstream region, the spacing between the discrete velocities has to be short in order to define accurately the highly peaked distribution functions. Secondly, the widely spread distribution functions in the downstream region require the discrete molecular velocities to be extended in a wide range [31]. Therefore, the integration limits are selected from the Rankine – Hugoniot relations and are given by the empirical relation provided by Shakhov [32]

$$-3\sqrt{T_2} < c_x > 3\sqrt{T_2} + u_1 \tag{3.22}$$

Equation (3.22) provide a good hint for the integrations limits. However, it is observed that these limits have to be expanded to at least ± 10 units. This method produces excellent results, but for each Mach number, the range of the discrete velocities has to be adjusted properly in order to minimize CPU time requirements. In the next section, the computational time is presented along with some attempts to reduce it.

Furthermore, since there is no solid boundary present in this problem, the shock may be located anywhere in space. It is thus necessary to place it arbitrarily on the numerical grid. The midpoint of the shock is taken to be where the density profile reaches the value 0.5. As the iterations proceed, there is a tendency for the shock to translate slightly in space so that the numerical grid must be shifted accordingly. Enough grid points must be taken to insure that all of the shock structure is included, since the extent of the shock in physical space is unknown a priori.

3.2.4 CPU time requirements

It is important to optimize the numerical scheme in order to get accurate results with the minimum computational cost. The required CPU time is presented in terms of the Mach number in Figure 3.2 for the numerical solution of the steady state shock wave problem using the BGK, S and ES models. The results describe the computational time per CPU core in minutes for two different domains (both start at -30 mean free paths and then one finishes at +20 and the second at +30). Even though, the range in the physical space is less important than the molecular velocity space it is still significant to optimize it. If the length of the physical domain is larger than needed the results will be accurate but the computational time is rapidly increased.

Observing the CPU time in Fig. 3.2, it is obvious that the ES model requires the shortest time at each Mach number in both domains, while the BGK model takes the longest time to converge. Especially in the Mach numbers of 2 and 3, the CPU requirements are 1827.4 and 1450.2 minutes well above the corresponding ones for the ES model. For these cases, the iteration procedure converges very slowly after the maximum error becomes 0.00003. However, further reduction of the physical space to [-20,20] and [-10,10] reduces time requirements to 161.09 and 3.27 minutes respectively but unfortunately, these small physical domains provide accurate results only at small Mach numbers. Moreover, the S model CPU requirements are between those of the BGK and ES models and considering the very good agreement with DSMC and BE results as well as with experiments which will be shown in Chapter 5, seems to be the most reliable model for normal shock wave simulations.

Generally speaking is very difficult to withdraw general rules or guidelines about discretization in the physical and velocity spaces. Hence, tailor oriented discretization with respect to the Mach number is needed.

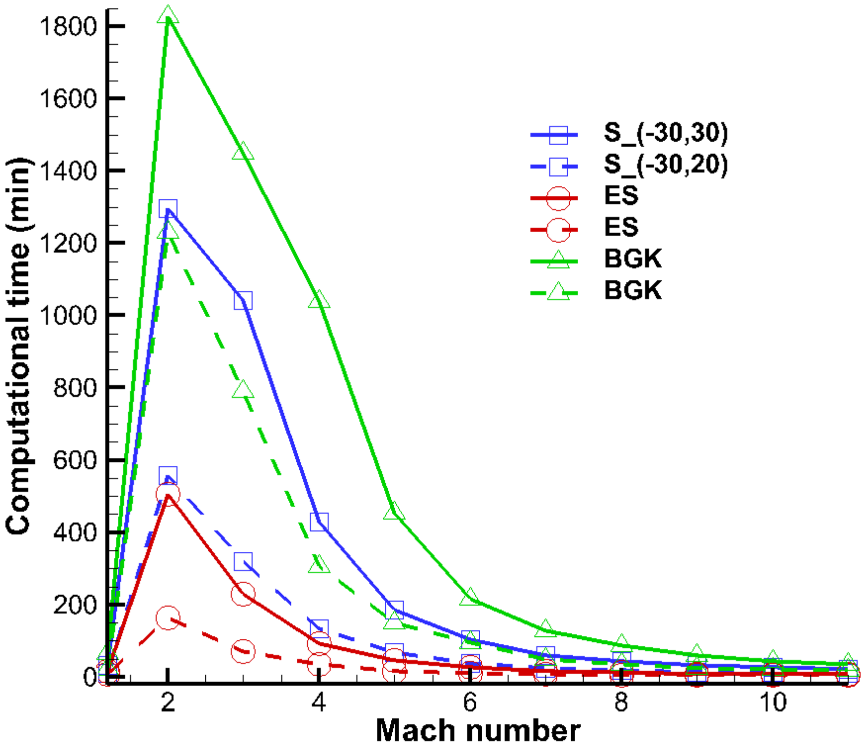

Figure 3.2: Computational time in minutes per cpu for the BGK, S and ES models, for different Mach numbers and two physical domains.

.

Chapter 4

Results and discussion

4.1 Numerical and flow parameters

The numerical results presented here have been obtained using the double projected kinetic equations for the BGK, S and ES model as they have been described in Chapter 3. In order to achieve good accuracy in the numerical results, the computational algorithm makes use of 9001 nodes in the spatial discretization at Mach number 1.2 and 6001 nodes at Mach numbers 3, 8 and 25. However, at Mach numbers 15 and 20 the nodes are reduced to 1001 and the results are exactly the same with the higher number of nodes. The cases with 1001 nodes have been run in an Intel core i5 4690, 3.5 GHz CPU, the cases for the Mach numbers 1.2 and 3 in six Intel core i5 2500, 3.3 GHz CPU's and the remaining cases in eight Intel core i5 3570, 3.4 GHz CPU's. The termination criterion for the iterative process has been set as the sum of the maximum relatives errors between the macroscopic quantities of the flow and equal to 10^{-5}.

Moreover, the density, temperature and velocity profiles are presented in a normalized form given by

$$\tilde{\rho} = \frac{\rho - \rho_1}{\rho_2 - \rho_1},\ \tilde{u} = \frac{u - u_2}{u_1 - u_2},\ \tilde{\tau} = \frac{\tau - \tau_1}{\tau_2 - \tau_1} \tag{4.1}$$

where the subscript 1 and 2 refer to upstream and downstream boundary conditions respectively. The normalized density is used everywhere, while the normalized velocity and temperature are used only in section 4.6. In the other sections the results for the velocity and temperature as well as for all other bulk quantities are presented in the dimensionless form described in Section 2.

Furthermore, the computed results correspond to a viscosity law which is according to the experimental conditions. For example, for Argon gas, Schmidt [8] suggests ω=0.68, Alsmeyer [3] suggests ω=0.72, while for pressure 101.325 Pa and temperature 0^{o} C, the real viscosity index is ω=0.81.

The numerical parameters for the kinetic models and the Navier-Stokes equations are tabulated in Tables 4.1 and 4.2 respectively. They include the range in the physical domain in mean free paths and in the molecular velocity space in dimensionless units. The number of nodes in both spaces is also provided. The viscosity index is specified as well as the perturbation parameter in the hydrodynamic solution.

Table 4.1: Parameters for BGK, S and ES models

Parameters	M_1=1.2	M_1=3	M_1=8	M_1=15	M_1=20	M_1=25
Nodes	9001	6001	6001	1001	1001	6001
Physical Domain	[-30,30]	[-20,20]	[-30,20]	[-50,50]	[-50,50]	[-50,50]
Range between molecular velocities	[-10,10]	[-10,10]	[-23,31]	[-35,49]	[-61,61]	[-61,61]
Space between molecular velocities	0.119	0.24	0.3	0.3	0.3	0.3
Δx	0.0066	0.01	0.00833	0.1	0.1	0.0166
Viscosity temperature index (ω)	0.5	0.5	0.68	0.68	0.68	0.66

Table 4.2: Parameters for Navier Stokes equations

Parameters	Ma=1.2	Ma=2	Ma=3	Ma=8
Nodes	9001	10001	6001	6001
Physical Domain	[-30,30]	[-30,30]	[-30,30]	[-30,30]
Perturbation (ε)	0.00001	0.00001	0.00001	0.00001
Viscosity temperature index (ω)	0.5	0.5	0.5	0.68

4.2 Macroscopic distributions for various Mach number

Results of the macroscopic distributions are provided in a wide range of the Mach number. In all cases only monatomic gases with the non-equilibrium state limited to the translational energy mode are considered. Comparisons are made with available computational results obtained by other methods as well as with experimental results. In all figures the x -coordinate is normalized by $\sqrt{\pi}\lambda_1 / 2$ where λ_1 is the mean free path of the gas molecules at the upstream conditions.

Figures 4.1, 4.3 4.5, 4.7, 4.9 and 4.10 present density, temperature, velocity and heat flux distributions inside the shock layer for various Mach numbers based on the S, ES and BGK models and Figs. 4.2, 4.4, 4.6, 4.8, 4.10 and 4.12 present the corresponding perpendicular, parallel and total temperatures. As a general remark it is stated that there is qualitatively agreement between the three kinetic models. Therefore, the detailed discussion of the macroscopic quantities in terms of the shock strength (i.e. the Mach number) will be based on the S model, while the comparison between the results of the three models will be also included. In all these figures the *x*-axis is in numbers of mean free paths (MFP). As it is mentioned before, the midpoint of the shock $x=0$ is taken to be where the normalized density profile reaches the value 0.5. The number of MFPs for $M_1=1.2$ is about 28, then for $M_1=3$ is decreased down to 6 and then as the Mach number is further increased the number of MFPs is monotonically increased but in a small pace reaching finally at $M_1=25$ the number of 10 MFPs. It is noted that these lengths are the ones needed to properly recover the upstream and downstream conditions including the proper shock thickness at each Mach number.

- **Number density**

The shock front is commonly presented with the number density profile. In all cases the number density is increased, while the proper upstream and downstream conditions are recovered. Observing carefully the density variation, it is seen that the profile is smooth at $M_1=1.2$ and then it gets steeper at $M_1=3$. This is expected since the flow departs from equilibrium. It is interesting to note however, that at $M_1=8$, the density variation is not as rapid as before and it starts getting smoother as the Mach number is further increased. As it is stated in Section 2 the number density variation provides an indication of the shock thickness in terms of the Mach number and the departure of local equilibrium. More specifically it seems that there is a minimum thickness in moderate Mach numbers which corresponds to Knudsen numbers in the transition flow regime. A more thorough discussion on the shock thickness is provided in Section 4.3.

- **Velocity**

The velocity distribution is always decreased along the shock wave. Far upstream corresponds to the imposed Mach number and then it is gradually reduced to its downstream value to fulfill the R-H relations. In the upstream area, the gradient is steeper that in the downstream area. As the Mach number is increased, the velocity gradient increases and more kinetic energy is dissipated. For example, for $M_1=1.2$, the initial velocity is $u_1=1.09$ and the final is $u_2=0.844$, while for $M_1=25$, the corresponding values are 22.82 and 5.73 respectively. Hence, the velocity decrease and the transition from the upstream to the downstream local equilibrium conditions become more abrupt as the upstream Mach number is increased.

- **Pressure**

The pressure distribution is related to temperature and density according to the equation of state. The pressure increase along the shock wave is qualitatively similar with that of the number density. Quantitatively however, the pressure gradient is much steeper than the density one due to the rapid modification of the temperature profile as well. Also, the maximum value of the pressure distribution changes rapidly with the increase of the Mach number. With the Mach number changing from 1.2 to 25 the maximum pressure increases about 50 times.

- **Heat flux**

The heat flux is taking negative values since the heat flux vector is in the negative *x* direction. Far upstream and downstream there is no temperature gradient and therefore its value is zero. The variation of the heat flux between the two limiting equilibrium states is non monotonic. More specifically starting far upstream the heat flux is decreased up to some point located few mean free paths before x=0 and then it is increased again. The variation is according to the temperature gradient along the flow field. Although the Fourier law is not always valid particularly in the case of high Mach numbers the heat flux is still proportional to the temperature gradient. Overall, the absolute value of the heat flux is rapidly increased with the increase of the Mach number. It increases several orders of magnitude as the Mach number is increased from 1.2 up to 25. Indicatively, for M_1=1.2, it is q=-0.03, while for M_1=25 it is q=-3662.7. The shape of the heat flux distribution continues to be similar in all Mach numbers, but its negative peak is moved towards the upstream area as the Mach number is increased. For M_1=1.2, it is close to x=0 and the profile is almost symmetric.

- **Parallel and perpendicular temperatures**

In highly anisotropic flows is useful to investigate separately the so-called parallel and perpendicular temperatures. They both increase along the shock wave flow field. At M_1=1.2 the profiles of both temperatures are increased smoothly. As the Mach number is increased the perpendicular temperature distributions remain smooth, while on the contrary the parallel (or longitudinal) is changing more rapidly and for M_1>2 a temperature overshoot is observed few mean free paths before x=0. In all these cases the profile versus the shock distance is non monotonic and the peak is always computed at the middle of the shock front. The temperature overshoot in the longitudinal temperature is defined by Eq. (2.65) and the following identity is obtained by Yen [33]:

$$\tau_{//} = \frac{\tau_{//1}}{3}\left[\left(5M_1^2+3\right)\frac{\rho_1}{\rho} - 5M_1^2\left(\frac{\rho_1}{\rho}\right)^2\right] \tag{4.2}$$

The $\tau_{//}$ temperature is differentiated with respect to ρ, and it is evaluated downstream (ρ=ρ_2) in order to obtain (apart from positive constant factors) $9-5M_1^2$. Thus, the parallel temperature has always an overshoot (since the density is monotonic) for $M_1 > \left(9/5\right)^{1/2} = 1.3416$. This overshoot is rather marked and this explains the overshoot in the temperature (the transversal temperature being always monotonic) [34]. This abruptly behavior increases its order of magnitude along with the Mach number and the distance is also increased in order to decay this perturbation. In both temperatures the gradient in the upstream area is steeper than in the downstream area.

- **Total temperature**

The total temperature is the sum of the parallel and the perpendicular temperature. Hence, its behavior has the added effects of both components. However, the overshoot that is mentioned before, it can’t be seen easily in these figures. The profiles are more close to the perpendicular ones, although they are more stip. Therefore, the temperature decomposition is always necessary and it reveals an important phenomenon in the shock wave structure.

In addition, the temperature-density separation presents a complex behavior for all the three kinetic models. The BGK model has the shortest distance while, the S model has the longest. For M_1=1.2 and for the S model, the temperature-density separation Δ is at 1.65, it decreases at 1.53 for M_1=3, but it is increased again until M_1=25, where it reaches its maximum value at 3.72. Therefore, it is clear that as the Mach number is increased, the non-equilibrium phenomena are more intense.

Closing this section it is noted that the other two kinetic models provide results for the macroscopic quantities which have a similar behavior with the one discussed above for the S model. More specifically there is very good agreement between ES and S models, while there are discrepancies which may become significant between the BGK and the other two models. This is due to the incorrect Prandtl number deduced by the BGK model. Only Xu and Huang [35] managed to produce good results with the BGK model but in their scheme, the Prandtl number is inserted through the correction of the heat flux in the update of the macroscopic variables and therefore effects the construction of the equilibrium state in the collision term as well as the update of the gas distribution function. As noted before, the ES model agrees well with the S model, but there are some cases with significant deviation, especially at high Mach numbers. In all the macroscopic distributions, the models differ significantly in the upstream area, while in the downstream area, the deviations are lesser.

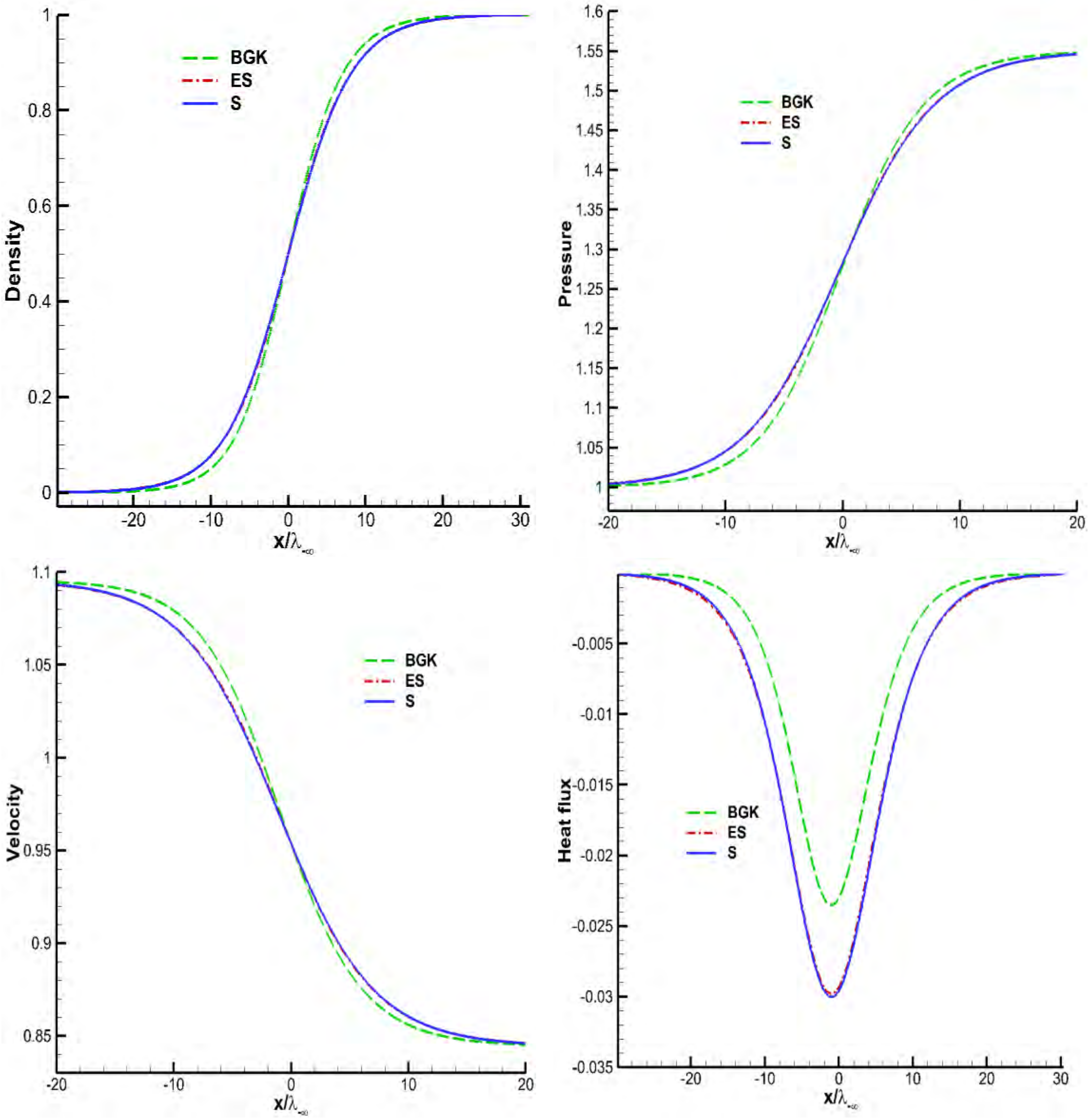

Figure 4.1: Normalized density, pressure, velocity and heat flux for upstream Mach number M_1=1.2 obtained by the BGK, ES and S models.

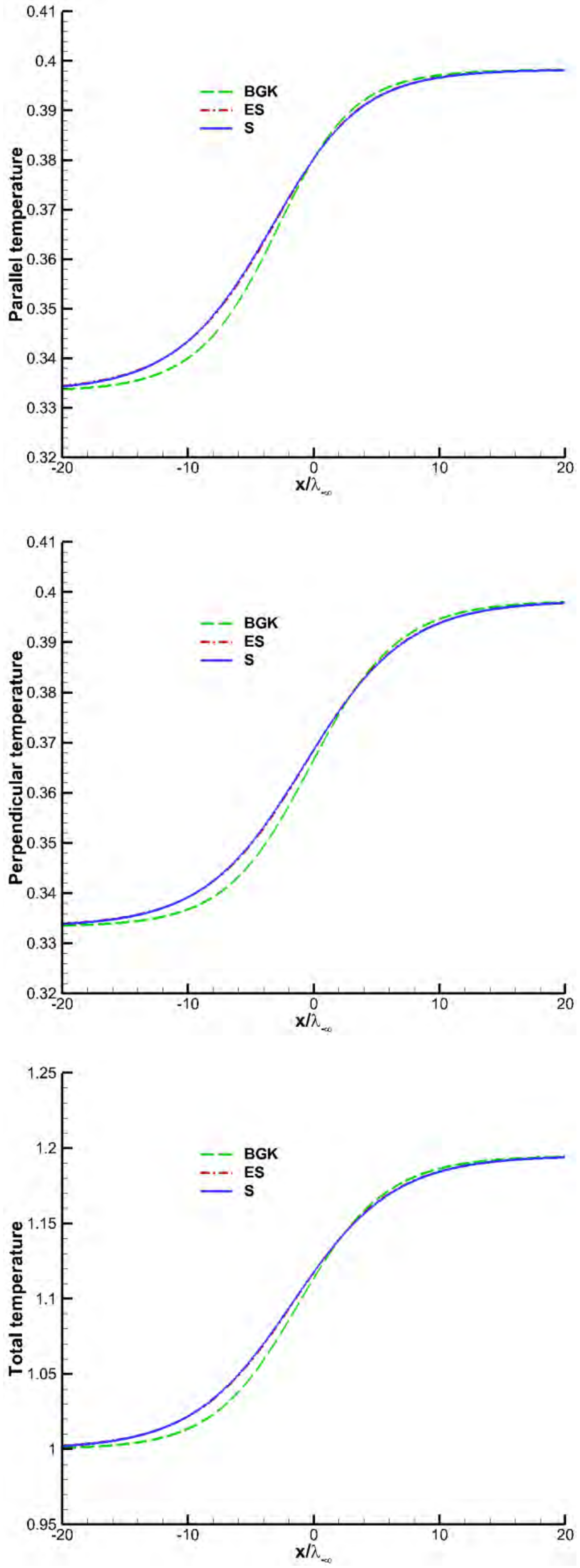

Figure 4.2: Parallel, perpendicular and total temperature for upstream Mach number M_1=1.2 by the BGK, ES and S models.

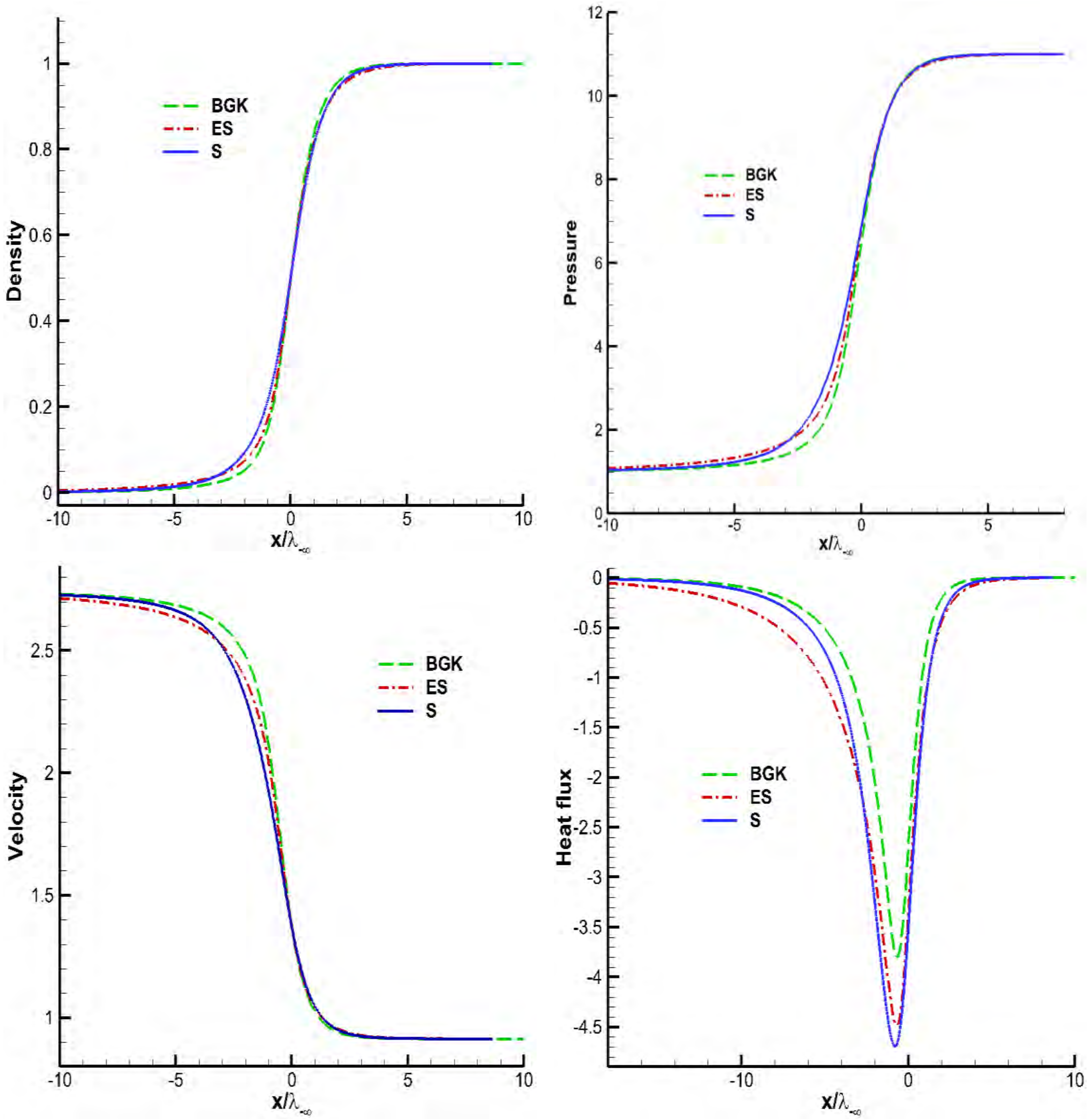

Figure 4.3: Normalized density, pressure, velocity and heat flux for upstream Mach number M_1=3 by the BGK, ES and S models.

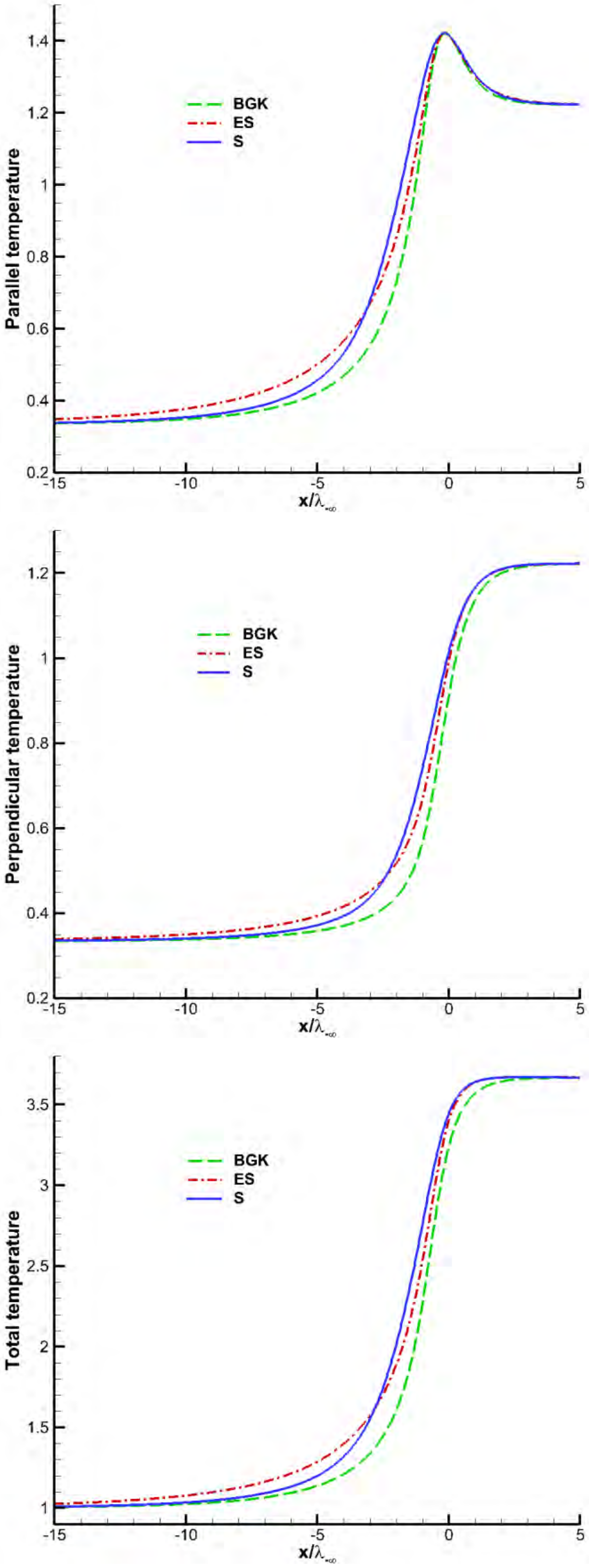

Figure 4.4: Parallel, perpendicular and total temperature for upstream Mach number M_1=3 by the BGK, ES and S models.

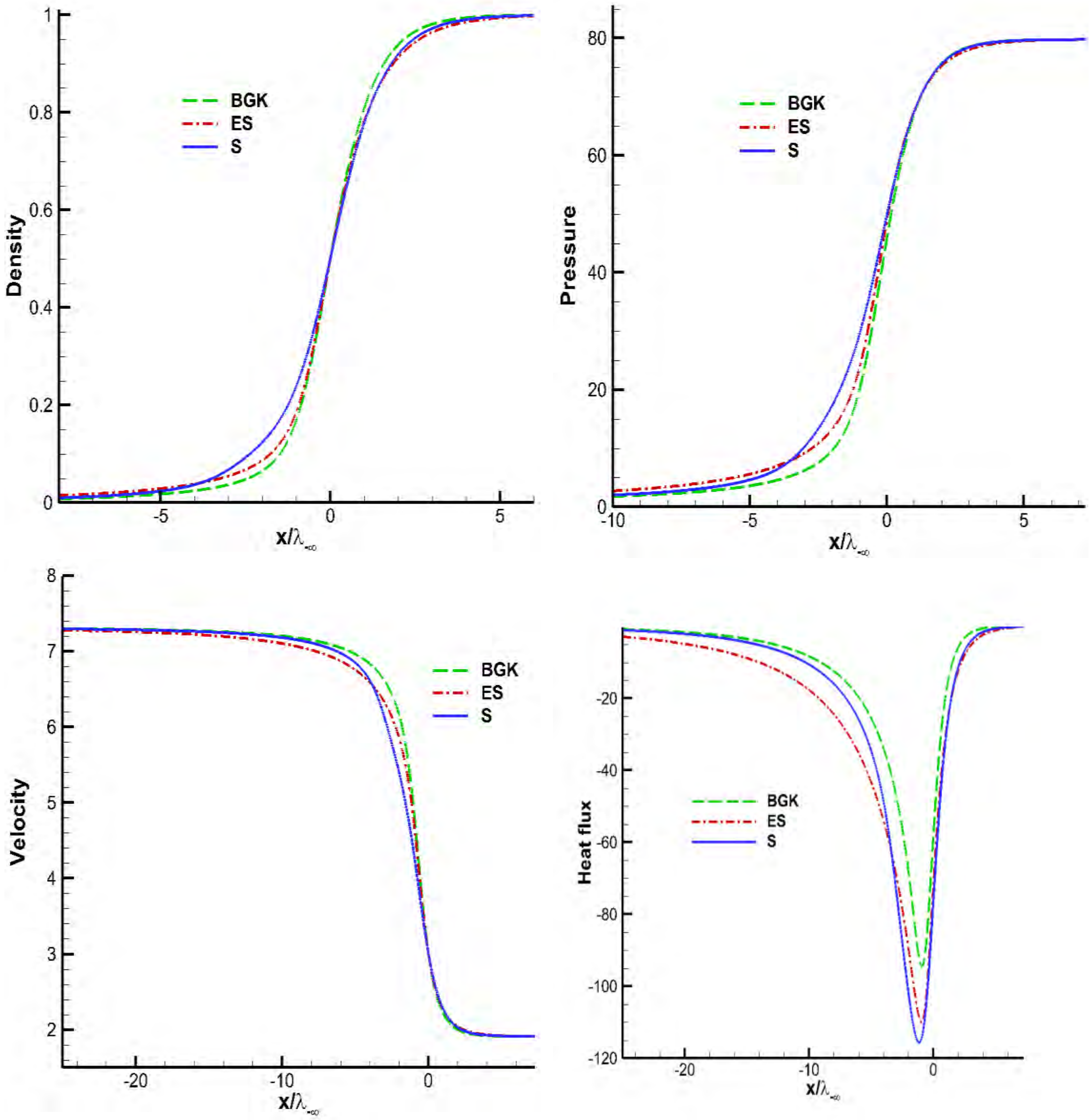

Figure 4.5: Normalized density, pressure, velocity and heat flux for upstream Mach number M_1=8 by the BGK, ES and S models.

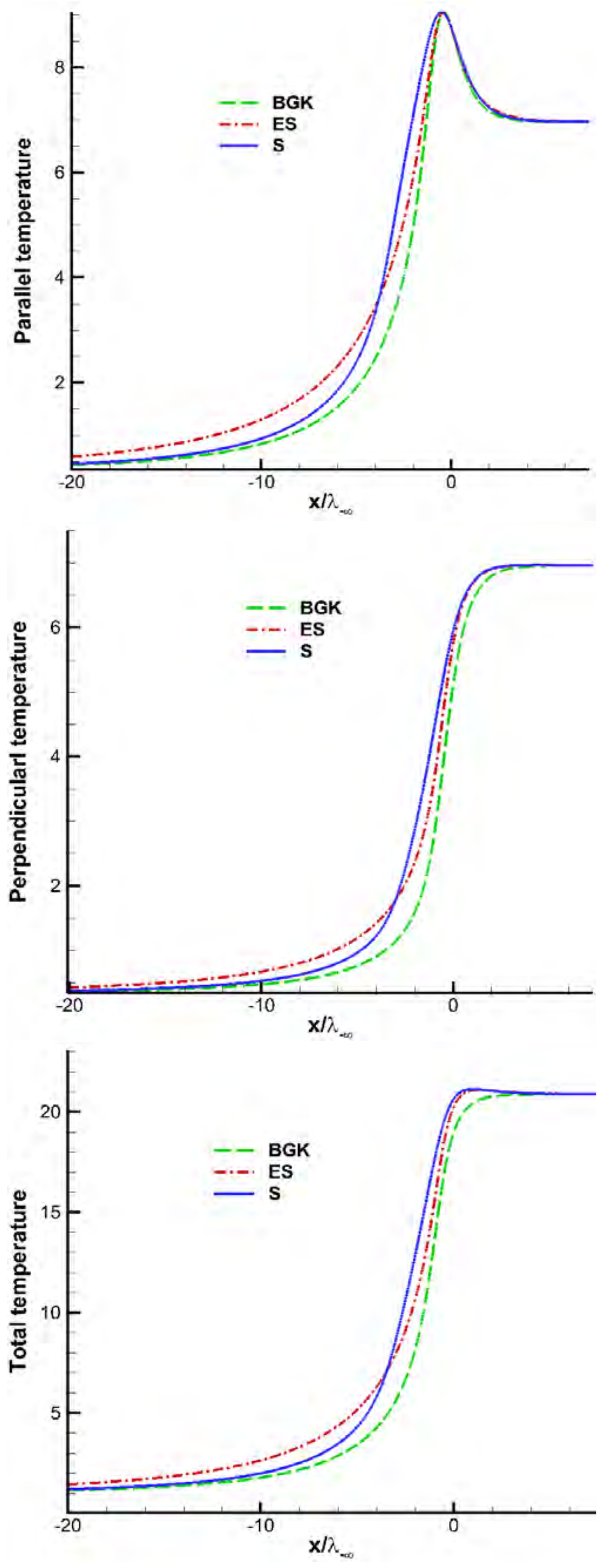

Figure 4.6: Parallel, perpendicular and total temperature for upstream Mach number M_1=8 by the BGK, ES and S models.

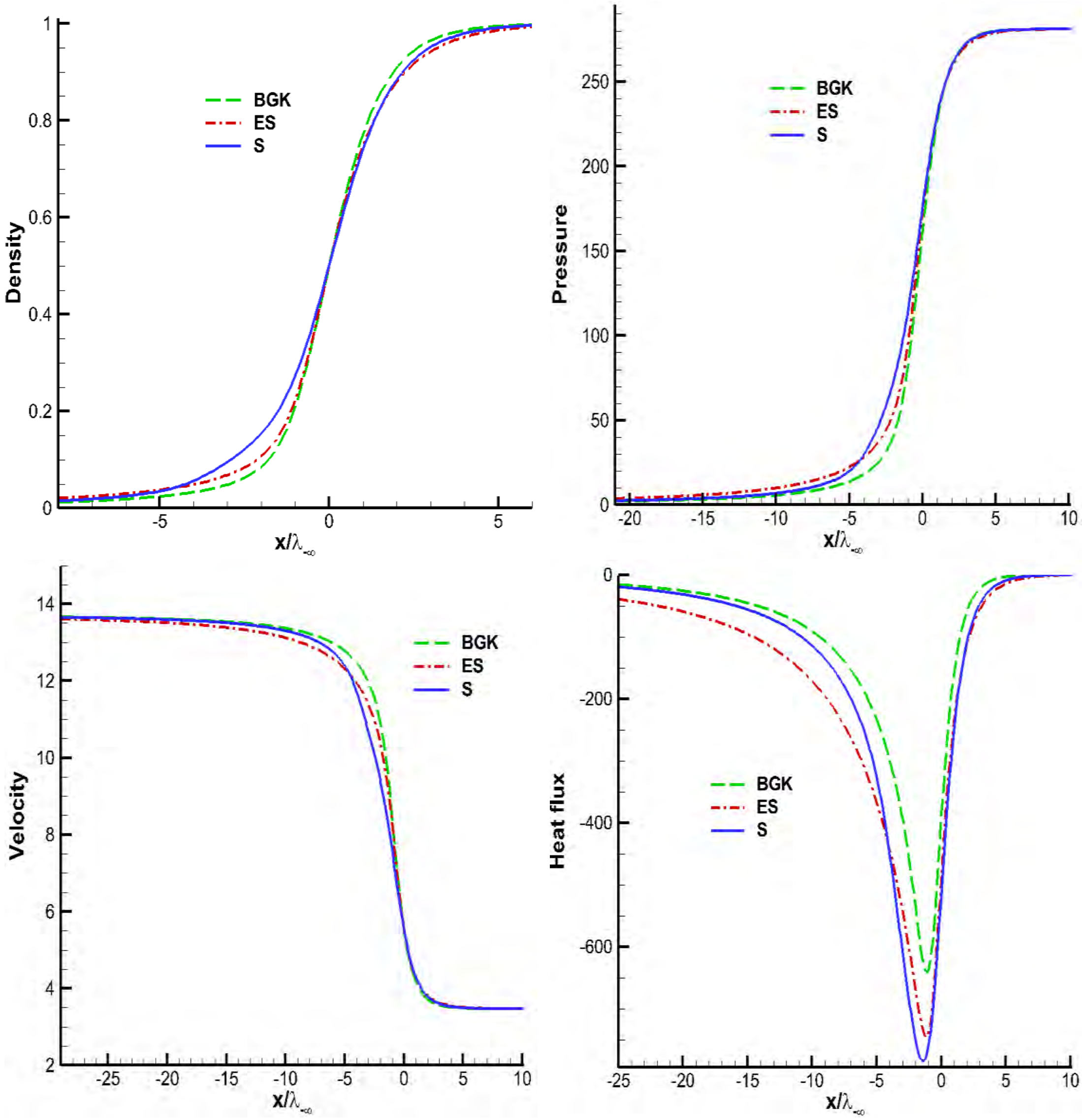

Figure 4.7: Normalized density, pressure, velocity and heat flux for upstream Mach number M_1=15 by the BGK, ES and S models.

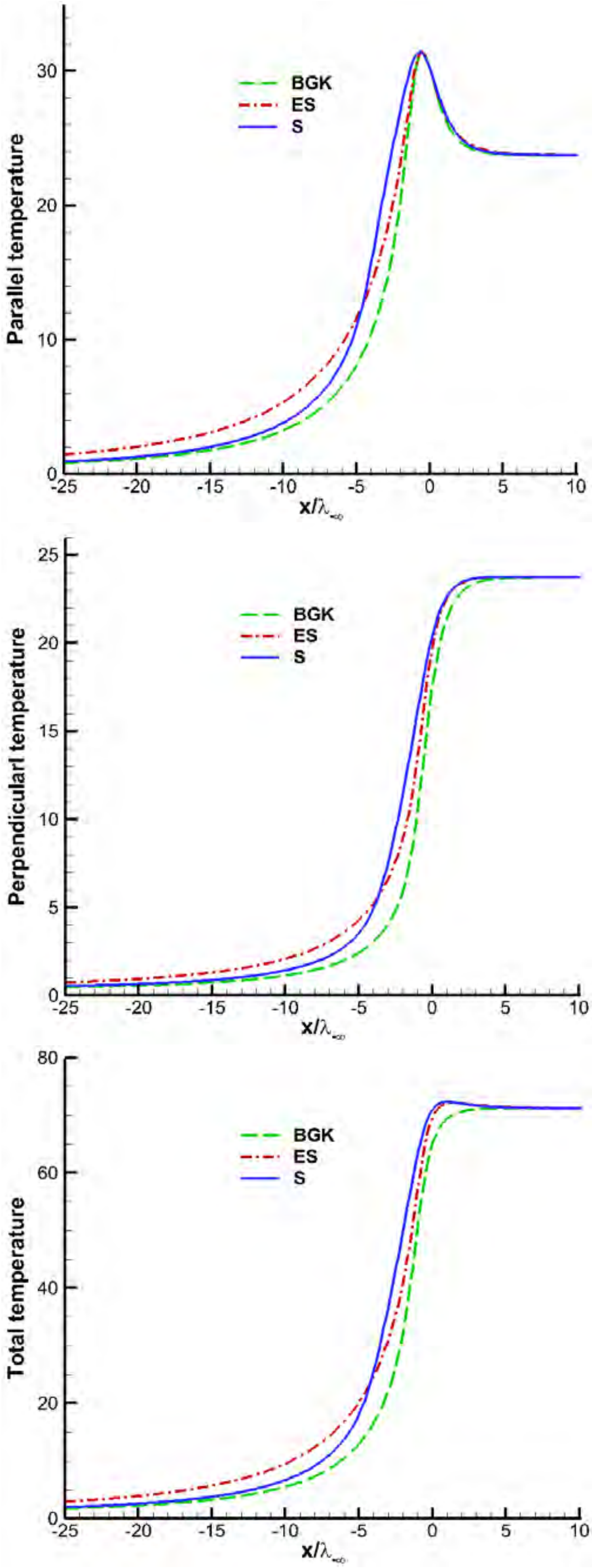

Figure 4.8: Parallel, perpendicular and total temperature for upstream Mach number M_1=15 by the BGK, ES and S models.

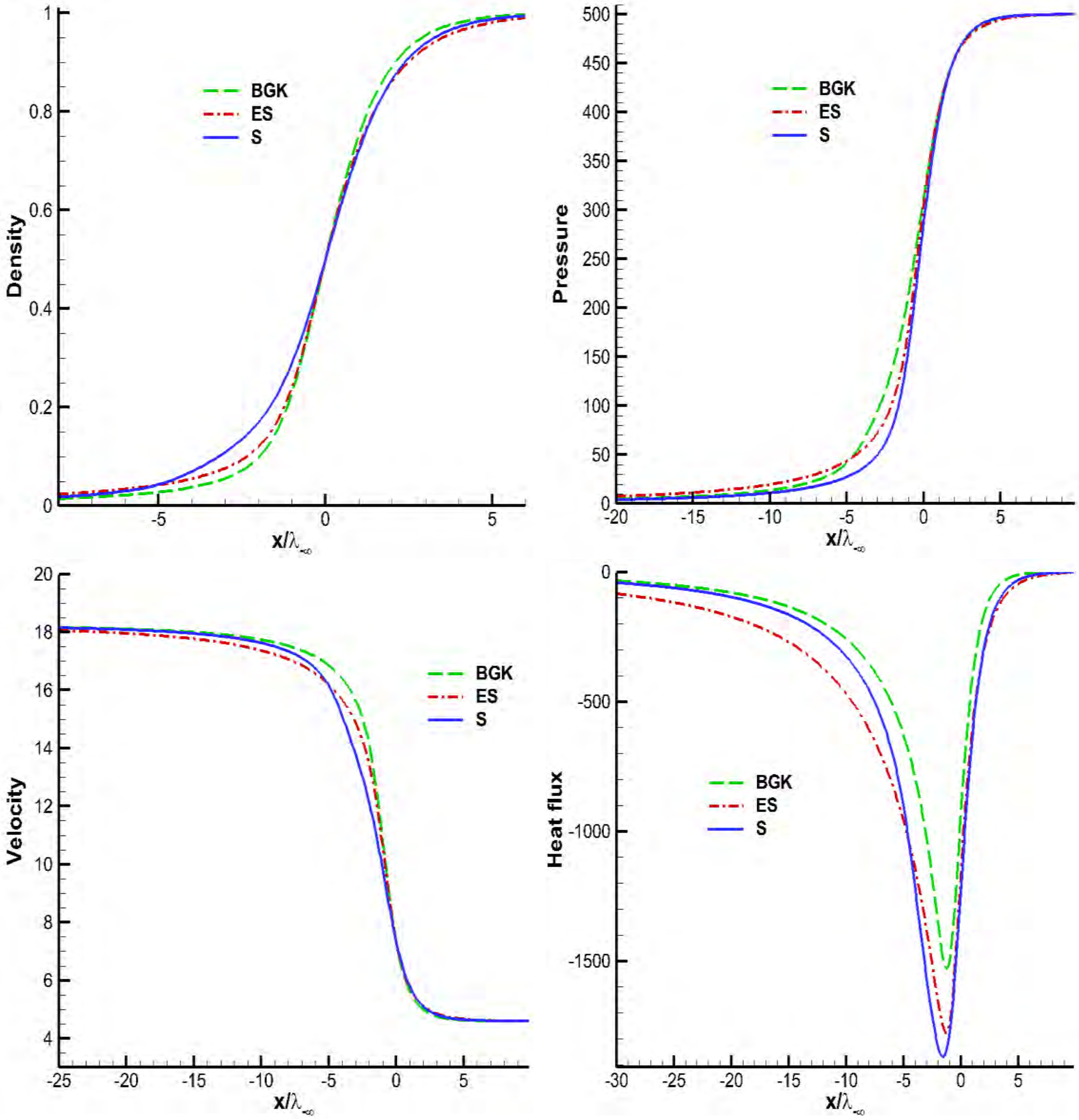

Figure 4.9: Normalized density, pressure, velocity and heat flux for upstream Mach number M_1=20 by the BGK, ES and S models.

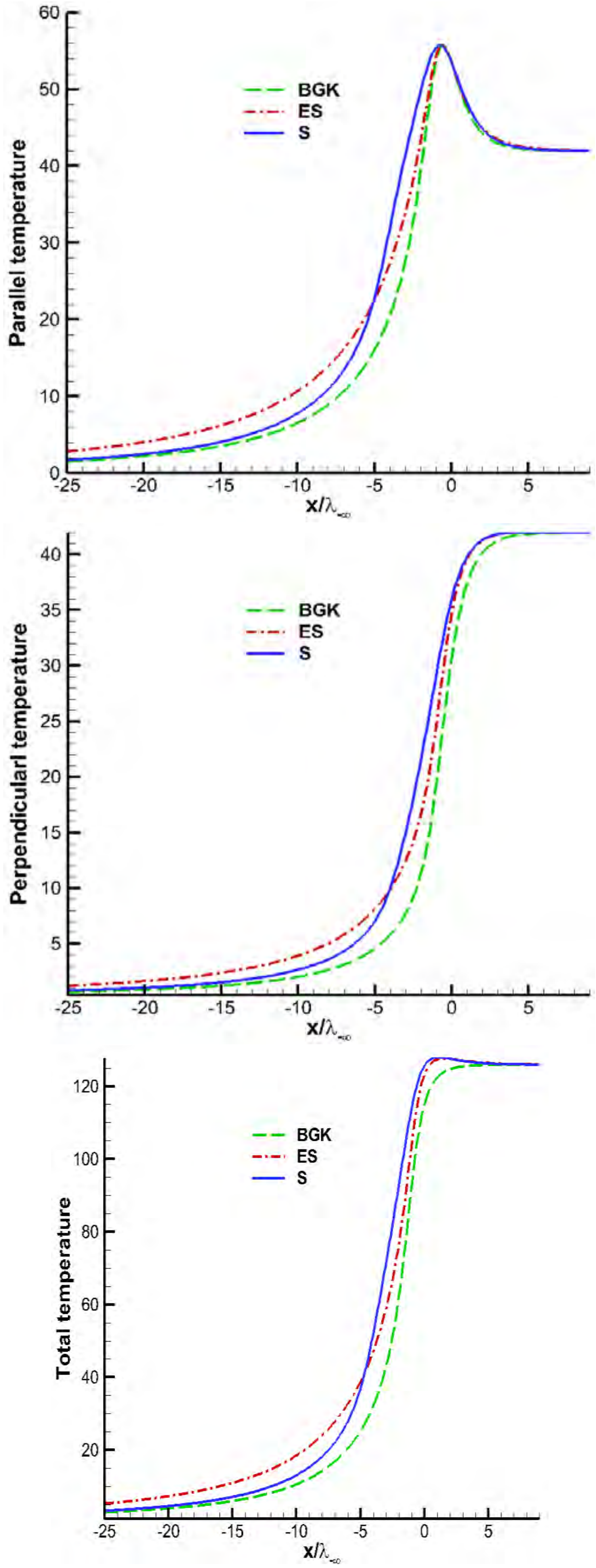

Figure 4.10: Parallel, perpendicular and total temperature for upstream Mach number M_1=20 by the BGK, ES and S models.

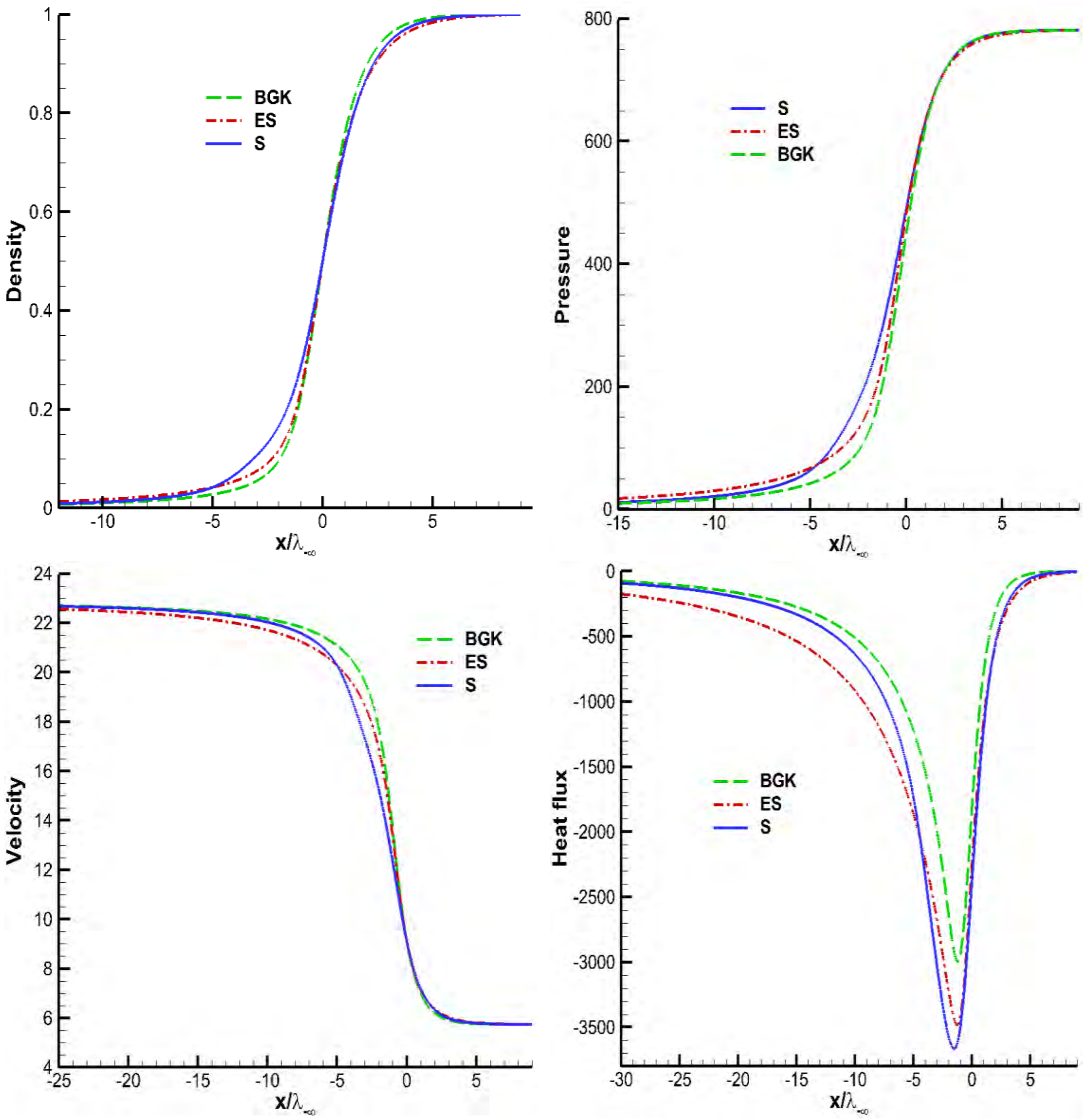

Figure 4.11: Normalized density, pressure, velocity and heat flux for upstream Mach number M_1=25 by the BGK, ES and S models.

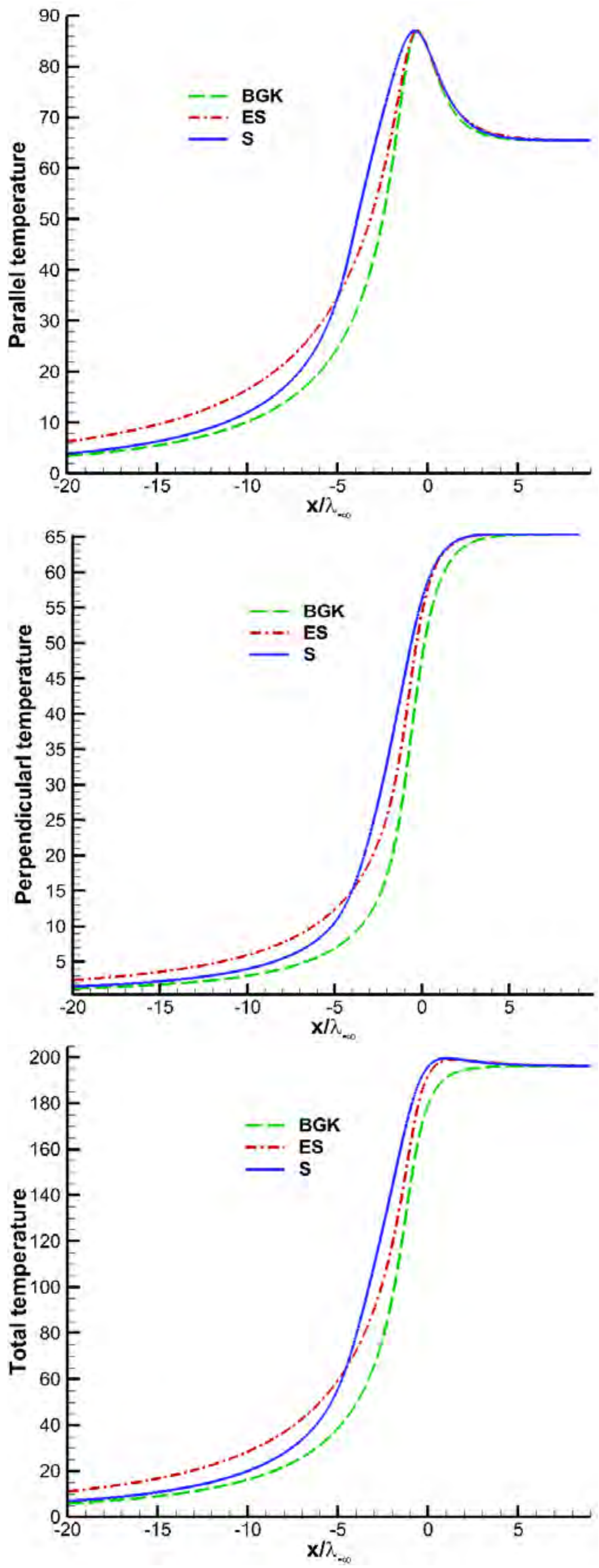

Figure 4.12: Parallel, perpendicular and total temperature for upstream Mach number M_1=25 by the BGK, ES and S models.

4.3 Shock thickness and effect of intermolecular potential

Figure 4.13 presents the reciprocal shock thickness versus Mach numbers from 1 up to 25 for argon gas with $\omega=0.72$. Apart from the kinetic models, both experimental data [3] and DSMC solutions [35] are also included for several Mach numbers. Figure 4.14 present the evolution of the Knudsen number versus the Mach number along with the results from the S model. At the beginning, the reciprocal shock thickness is increased very rapidly and the maximum value is reached at about M_1=3. Afterwards, it is decreased, while the Mach number is further increased. As it is mentioned before that the number of MFPs is minimum at M_1=3 which is confirmed with the reciprocal shock thickness. Also, observing carefully it is seen that near the continuum low Mach number limit, the S and the ES model have a better agreement with the experimental data. This is expected because the S model and the ES model deduce accurately the NS solution in the continuum regime. However, as the Mach number is increased not only the BGK but also the ES results do not agree well with the experimental data. This comparison clearly demonstrates the growing discrepancy between the ES and BGK models with experiment at large Mach numbers. Also, the BGK thickness is thinner than that of the ellipsoidal model at low Mach number, while as the Mach number is increased, the calculated shock thickness shows small differences between the two models. However, the S model seems to have very good agreement with the experimental data in the whole range of the Mach number. Even at about M_1=5 where the most significant deviation is spotted for the other models, the S model behaves very well. It is also seen that the DCMC and the S model solutions are very close at low Mach numbers, but as the Mach number increases, the two approaches begin to disperse with the S model solution always being very close to measurements. Overall, the Knudsen number is increased while the local Kn is decreased after M_1=4.

Observing Figs. 4.15 and 4.16, it is clear that the intermolecular potential has significant impact on the density and temperature shock profiles. This comparison is presented only for the S model since similar effects are found for the ES and the BGK models. In the upstream area, the temperature is greatly affected from the intermolecular potential, while in the downstream area, the results based on the two intermolecular models seem to converge. For M_1=1.2, the intermolecular potential has minimum effect on the profiles, while for M_1=8 and 25 there are large differences. The bulk distributions obtained for various real gases, such as Argon with ω=0.72, are placed between the limiting cases of hard sphere and Maxwell molecules. In all cases the hard sphere model provides results much closer to the ones corresponding to real gases compared to the Maxwell model, which is quite unrealistic. From the point of view of the CPU time requirement, the case with the Maxwell model needs always the shortest time to converge, while the hard sphere model needs the longest time because it has to traverse the longest distance in order to reach its solution. In conclusion, the effect is increased as the Mach number is increased, while the CPU time requirement is decreased.

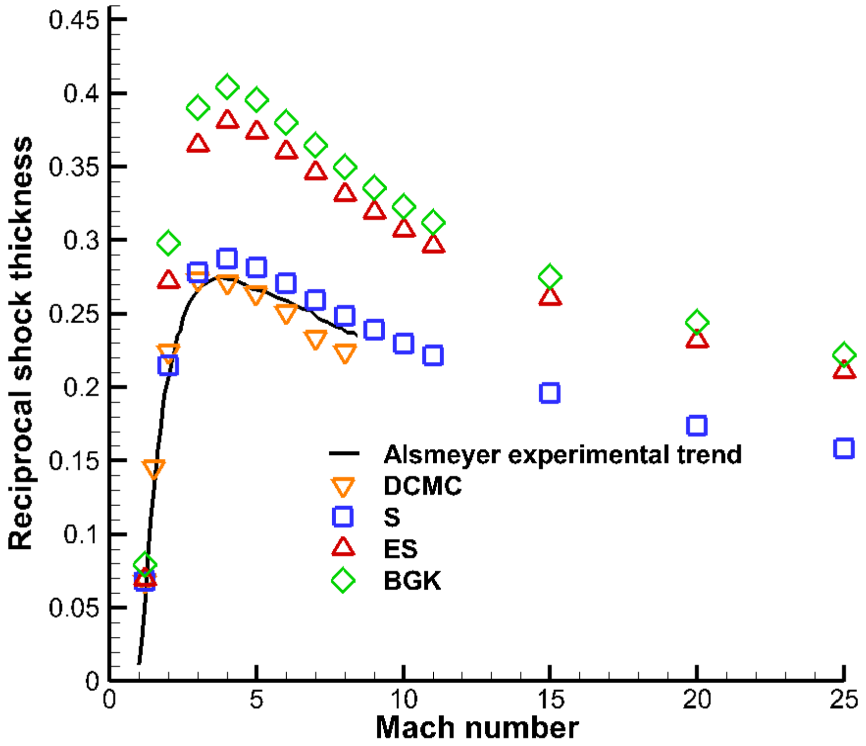

Figure 4.13: Reciprocal shock thickness versus Mach numbers for based on the BGK, ES and S models, the DSMC method [35] and experimental data [3] for Argon.

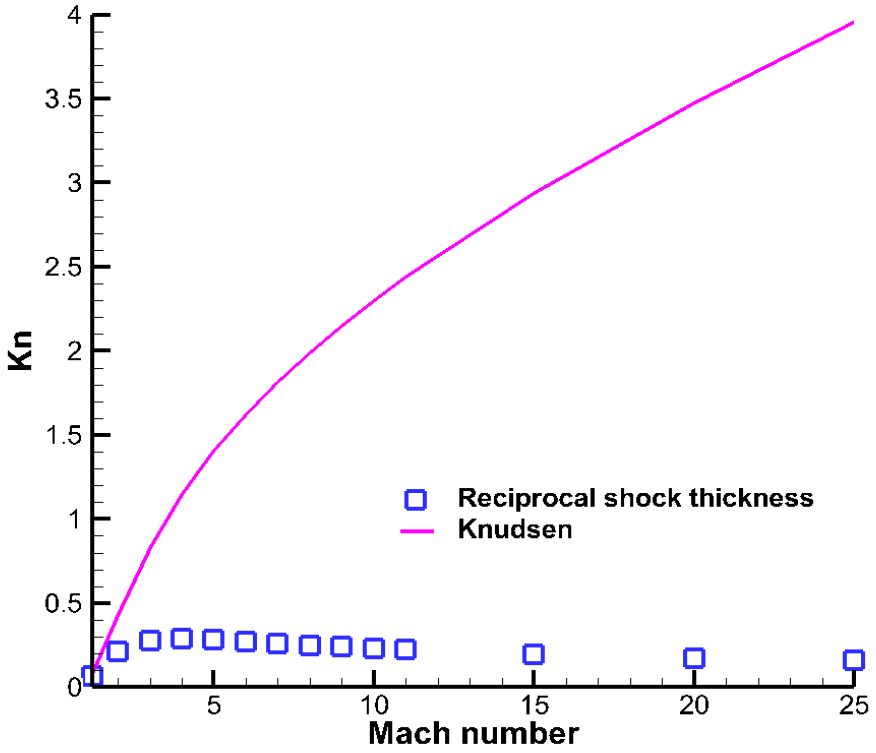

Figure 4.14: Knudsen number versus Mach numbers for Argon gas (the reciprocal shock thickness based on the model is also shown).

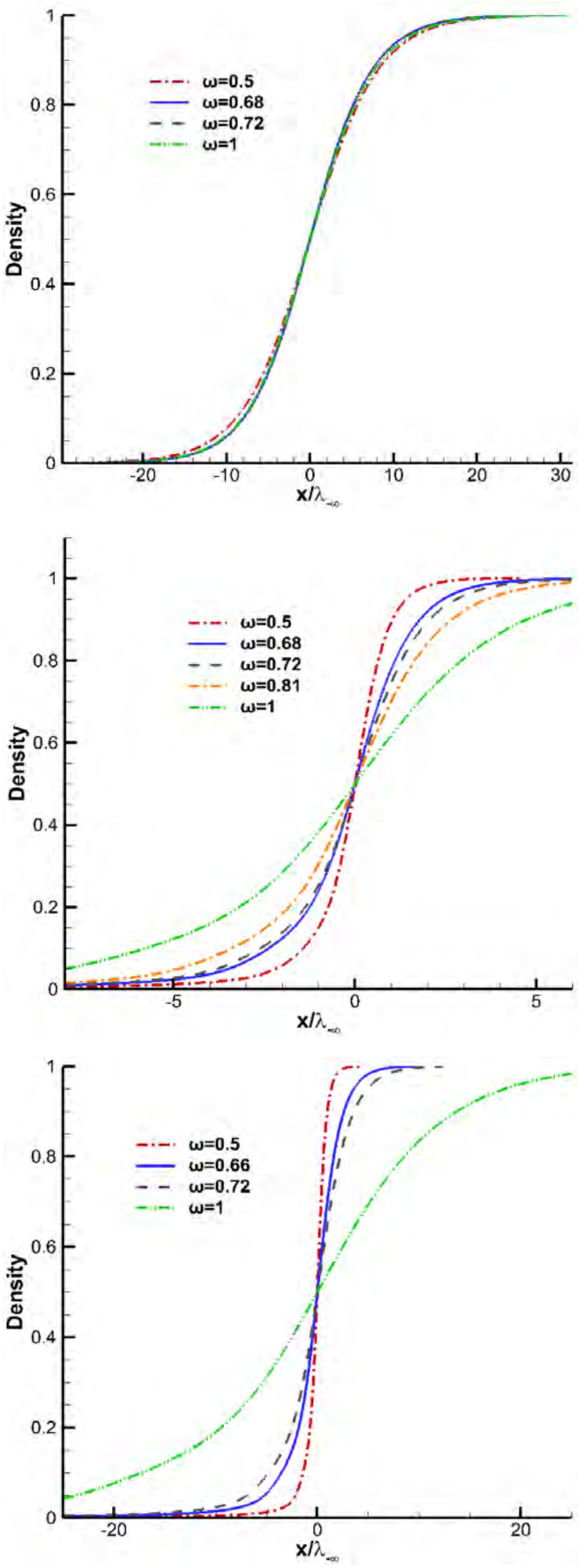

Figure 4.15: Effect of the intermolecular potential on the density profile based on the S model for upstream Mach numbers M_1*=1.2, 8 and 25.*

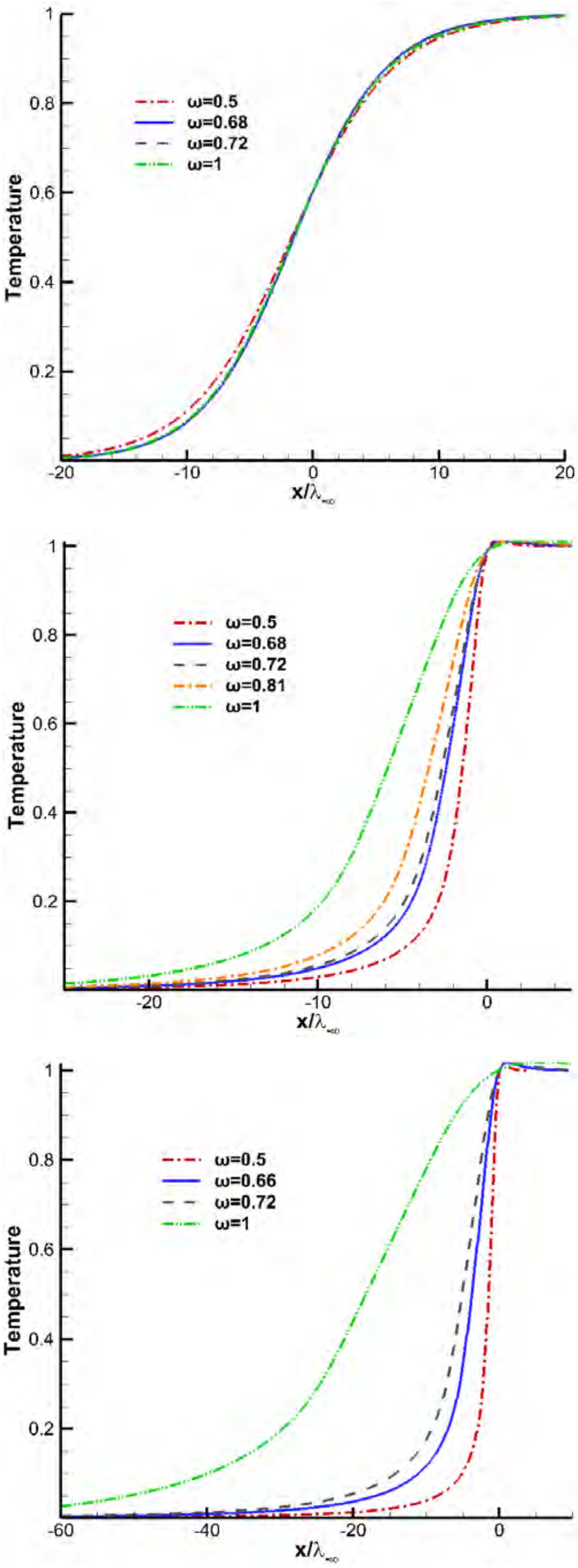

Figure 4.16: Effect of the intermolecular potential on the temperature profile based on the S model for upstream Mach numbers M_1=1.2, 8 and 25.

4.4 Comparison of kinetic models with Boltzmann equation, DCMC and experiments

The kinetic model results are compared with corresponding ones based on the direct solution of the Boltzmann equation (BE), the DCMC method and experiments. The comparison with the BE is based on the solution provided by Ohwada [36] for hard sphere molecules at M_1=1.2 and 3. Figure 4.17 presents the density profiles inside the shock layer for all kinetic models and the Boltzmann equation. It is clearly seen that the S and ES models produce identical results at M_1=1.2, while there are small differences with the BGK model. At M_1=3 the S model keeps having very good agreement with the BE, while the ES results have some differences particularly in the upstream region.

Following the validation with the Boltzmann equation, the results from the kinetic models are compared with the DCMC solutions provided in [35, 37, 38]. In Fig. 4.18 the density profiles are presented, for M_1= 8 and 11 with $\omega=0.72$ and for M_1=25 with $\omega=0.75$. Observing carefully the density variation, it is seen that the S model complies with the DCMC solutions for the three Mach numbers. As it is mentioned before, the differences between the S and the other two models are increased with the Mach number. However, for Mach number 25, the ES model seems to produce better results.

To further validate the capability of the gas-kinetic algorithm in computing the higher-order macroscopic moments of the distribution function, the heat flux q_x and the viscous normal stresses σ_{xx} and σ_{yy} are compared in Fig. 4.19 for M_1= 8. The heat flux q_x and viscous stresses σ_{xx} and σ_{yy} have been normalized by dividing by the product of the density times and the most probable velocity in the cubic power. It can be distinctly revealed that the profiles of the heat flux and the viscous stress are not symmetric across x=0. The agreement between the DSMC results and the kinetic models is very good in the downstream area, while the major differences exist in the front of the shock wave. In addition, the S and the ES models seem to be more close to the DCMC solution rather than the BGK model. In terms of the stresses, it is noted that the ES model agrees better with the DCMC results than the other two models.

The measured density profiles from Schmidt [8] at M_1=2.8 and 8 are presented in Fig. 4.20 along with the computed results. Once again the results based on the S model are in better agreement compared to the other two. Furthermore, in Fig. 4.21, the computed results are compared with another set of measurements that is obtained by Alsmeyer [3]. The cases are for M_1=8 and 9 with viscosity-temperature index ω=0.72. The variations that become apparent at M_1=2.8, are now more obvious. The differences between density profiles for ES and BGK models become less distinguishable and both models give poorer agreement with experiment as the Mach number increases. The density profiles are always too steep, especially for the BGK model which seems to be the most inadequate. However, the S model continues to give the proper solution and it seems to have better agreement with ω=0.72 rather than ω=0.68.

The helium shock structure calculations for M_1=25 are presented in Fig. 4.22. The distribution functions from the S model are compared with the experimental data in Pham-Van Diep et al [12]. The gas distribution functions are presented directly at different locations inside the shock layer. The locations of the normalized density for the distribution function presentation are at $\rho = 0.291, 0.332$ and $\rho = 0.610, 0.636$. In order to compare the same quantities, the velocity distribution function has been normalized with its maximum value. Also, the x axis is normalized with the reference molecular velocity where the maximum distribution function is observed. The comparison appears to be good and the most significant deviation is for the downstream part, where there is a spot that the calculated results do not agree with the measured profile. Finally, it seems that the distribution functions are not too sensitive to the locations inside the shock layer.

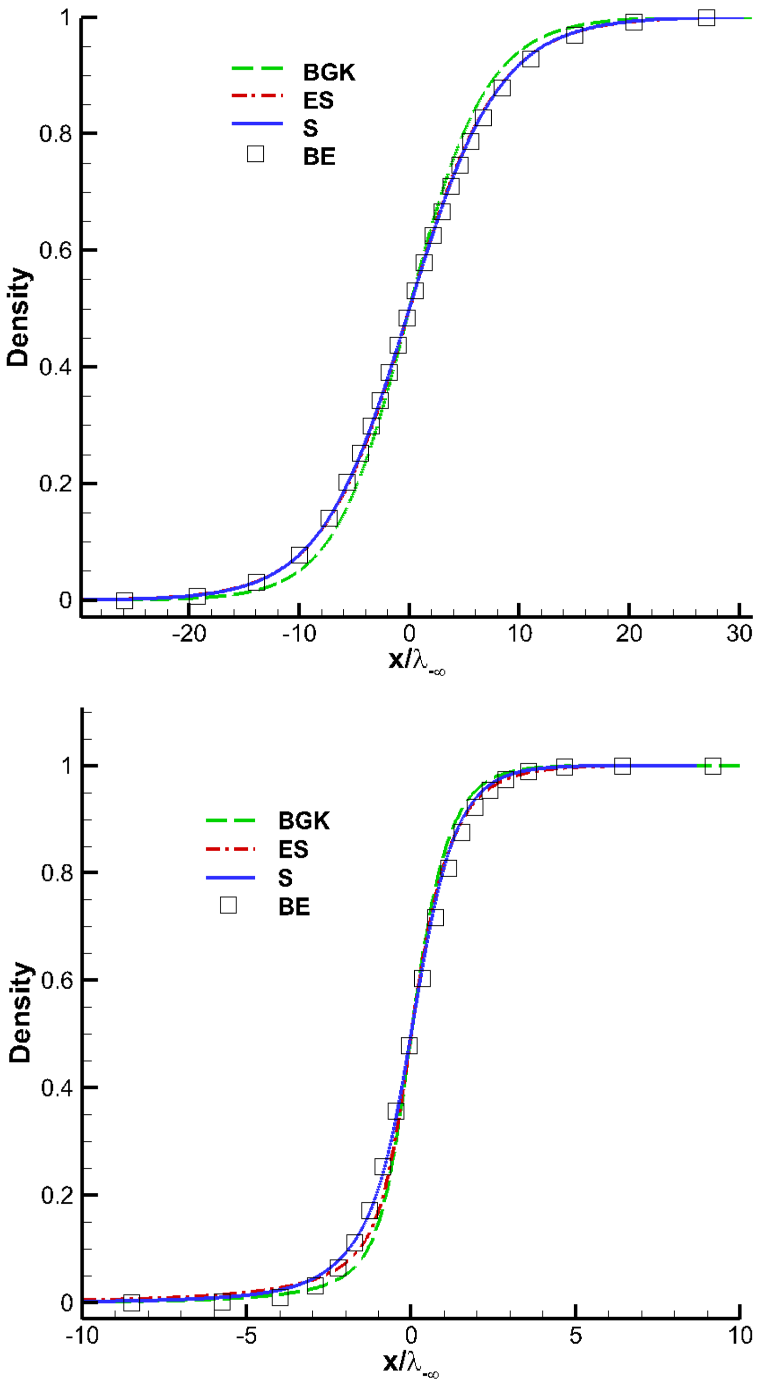

Figure 4.17: Density profiles at M_1=1.2 and 3 in a hard-sphere shock structure computed by the BGK, ES and S models and the Boltzmann equation [36].

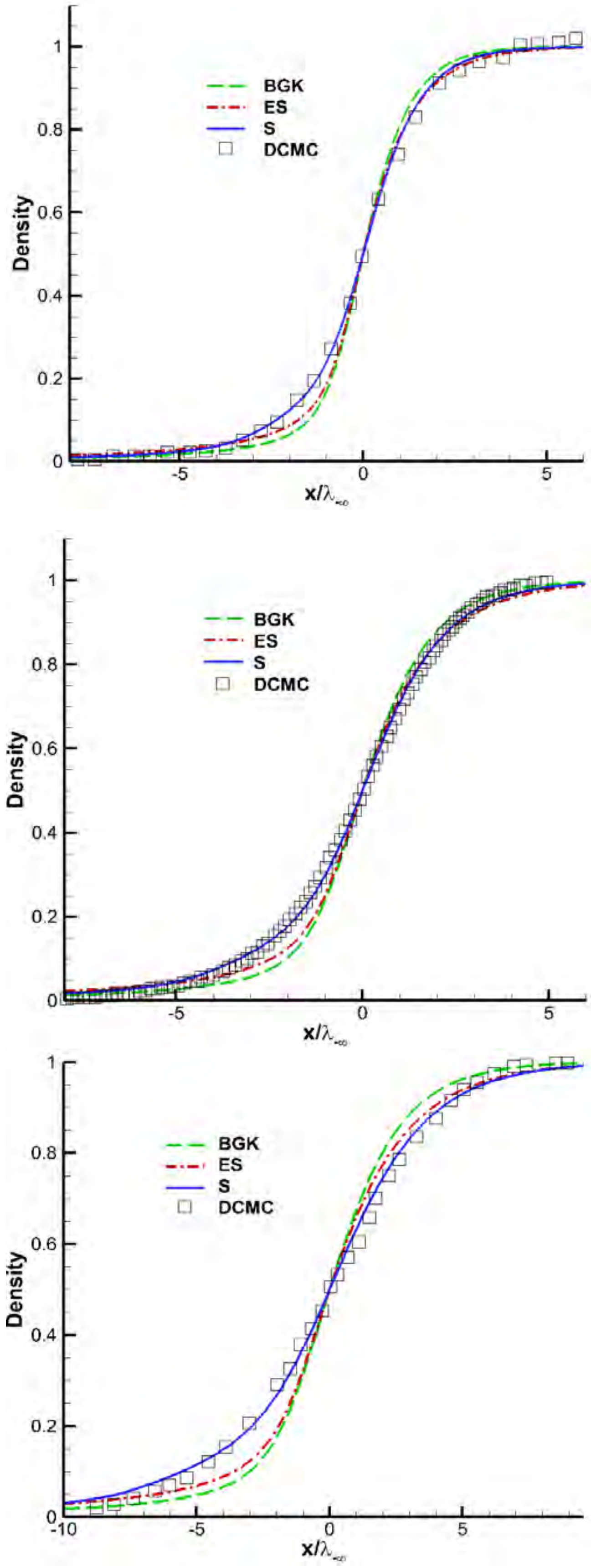

Figure 4.18: Density profiles at M_1=8 and 11 with ω=0.72 and at M_1=25 with ω=0.75 in an Argon shock structure computed by the BGK, ES and S models and the DSMC method [35, 37, 38].

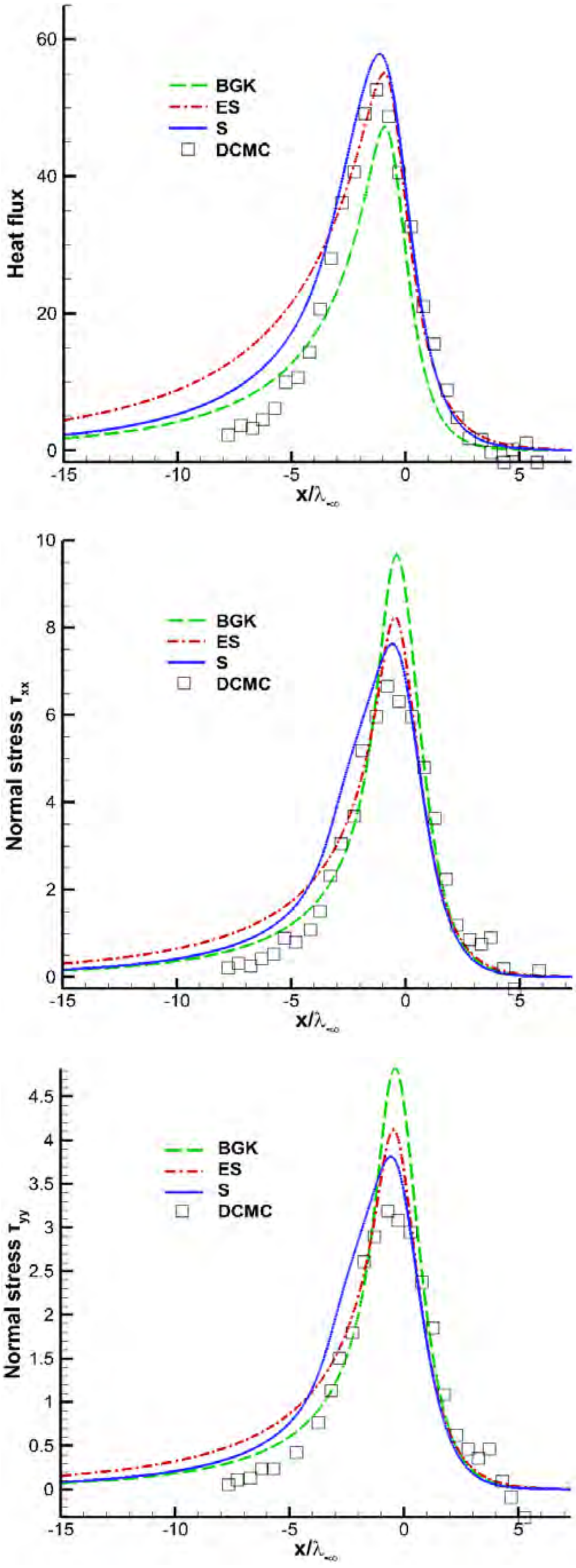

Figure 4.19: Heat flux and normal stress profiles at $M_1 = 8$ computed by the BGK, ES and S models and the DSMC method [38].

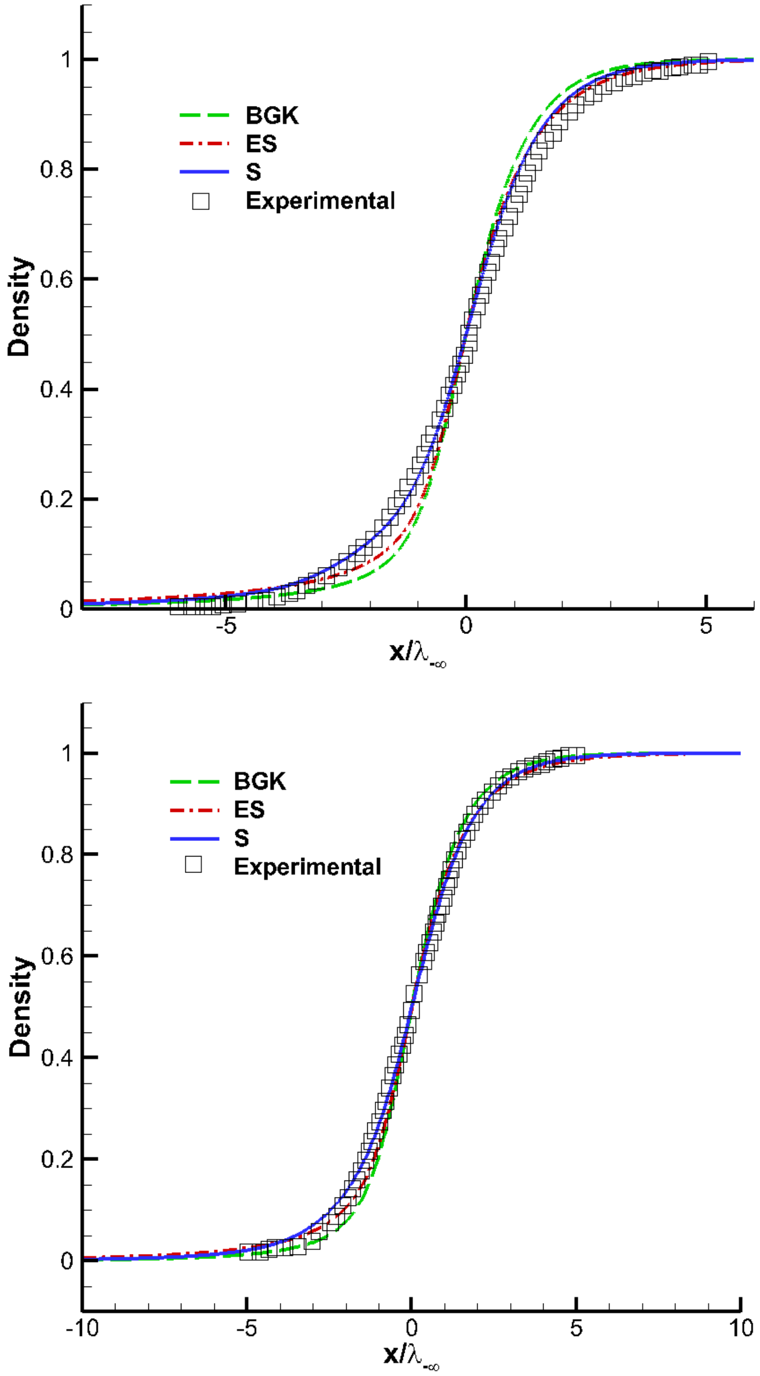

Figure 4.20: Density profiles at M_1= 2.8 for ω=0.75 and M_1=8 for ω=0.68 in Argon computed by the BGK, ES and S models and comparison with the experimental data in [8].

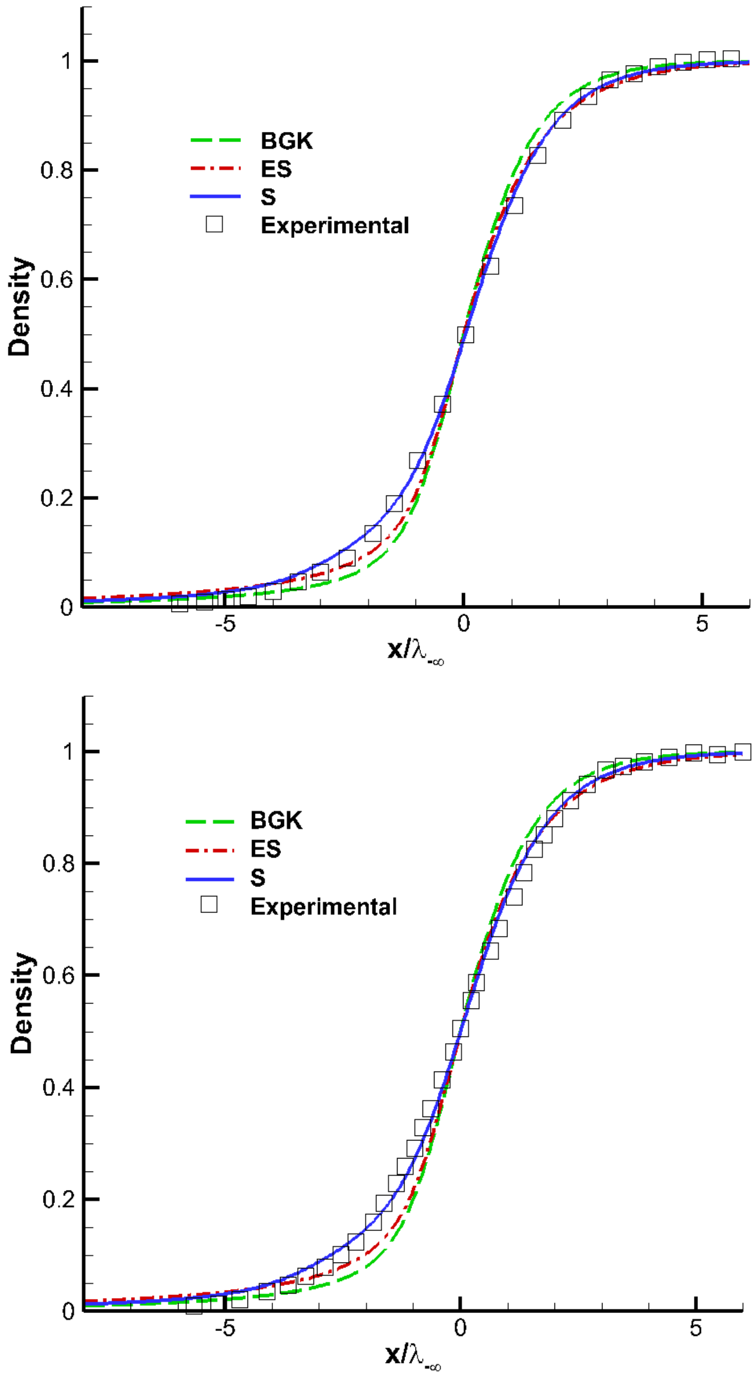

Figure 4.21: Density profiles at M_1= 8 and 9 for ω=0.72 in Argon computed by the BGK, ES and S models and comparison with the experimental data in [3].

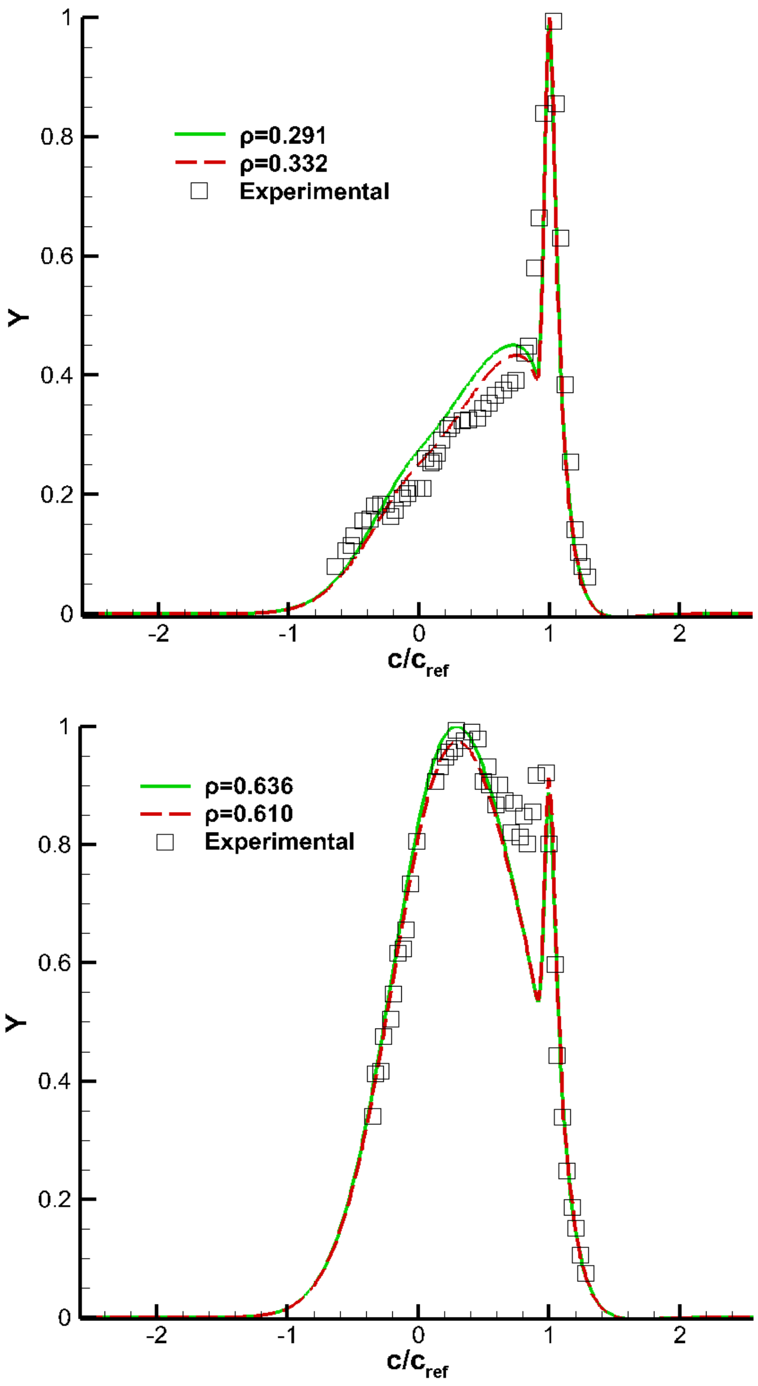

Figure 4.22: Gas distribution functions at M_1=25 helium shock layer computed by S model and comparison with the experiment data in [12] at different locations with normalized densities (ρ=0.291, 0.332, 0.610, 0.636).

4.5 Distribution functions of the BGK, ES and S model in various positions for different Mach numbers

The shape of the reduced distribution functions Y and Φ at several locations as computed by the BGK, ES and S models are presented. Even though, the results are not projected, two of the locations are in the upstream area, one is in the middle of the shock front and the remaining two in the downstream area. Also, the equilibrium distribution function Y^{eq} and Φ^{eq} of each model are also shown in order to observe the departure of the distributions from the corresponding equilibrium ones (it is not shown for except for M_1=1.2 because in this small Mach number they are almost identical). The detailed discussion of the distribution functions in terms of the molecular velocity is based on the S model which seems to be the most promising one.

Figures 4.23, 4.25 and 4.27 present the distribution function Y for all three models and for M_1=1.2, 8 and 25, while Figures 4.24, 4.26 and 4.28 present the corresponding results for the distribution function Φ. For M_1=1.2, both the distribution functions are similar which is expected because the solution is the continuum area where all the solutions give close-by results. Moreover, the equilibrium distribution functions are very close to the computed and the only small variations are seen in the middle of the shock front. It is interesting to note that at M_1=8, the distribution functions obtain non-equilibrium shape within the shock wave. The transition from the sharply peaked upstream distribution to that corresponding to the downstream equilibrium state is clearly indicated. However, the distribution function contribution is initially formed about a negative velocity rather than about the downstream equilibrium flow velocity. The small peak barely seen on the curve corresponding to the most forward location indicates that a small number of oncoming molecules undergo collisions far upstream. This behavior in the distribution function grows and moves to the right in c_x as one progresses through the shock it finally forms the distribution of the downstream flow. Also, the highly peaked shape corresponding to the upstream conditions exhibits a similar behavior since the magnitude of the peak decreases. However, its location in c_x does not change noticeably. Both the distribution functions present this behavior, while it seems to be more significant for Y.

It is also noted that even in the downstream area where the shape between the distribution function Y of the three kinetic models is similar, their maximum values are different. However, in the upstream area, there are quantitatively and qualitatively deviations. For example, at locations 36 and 39, the distributions are very steep for the ES and the BGK models, while the profile for the S model is smoother. In addition, the S and the BGK profiles are similar in the middle of the shock front, while the ES model presents a more abruptly shape and a peak that is correlated with the upstream behavior. All these discrepancies are encountered in the distribution function Y and for M_1=8.

Although, for M_1=25, they are decayed and the profiles become similar for all models. This is also observed in the Φ distribution where the variations are minor between the models. Finally, it is clear that the equilibrium distribution functions always overestimate the computed results in the middle of the shock, while in the upstream area, they underestimate the computed profiles.

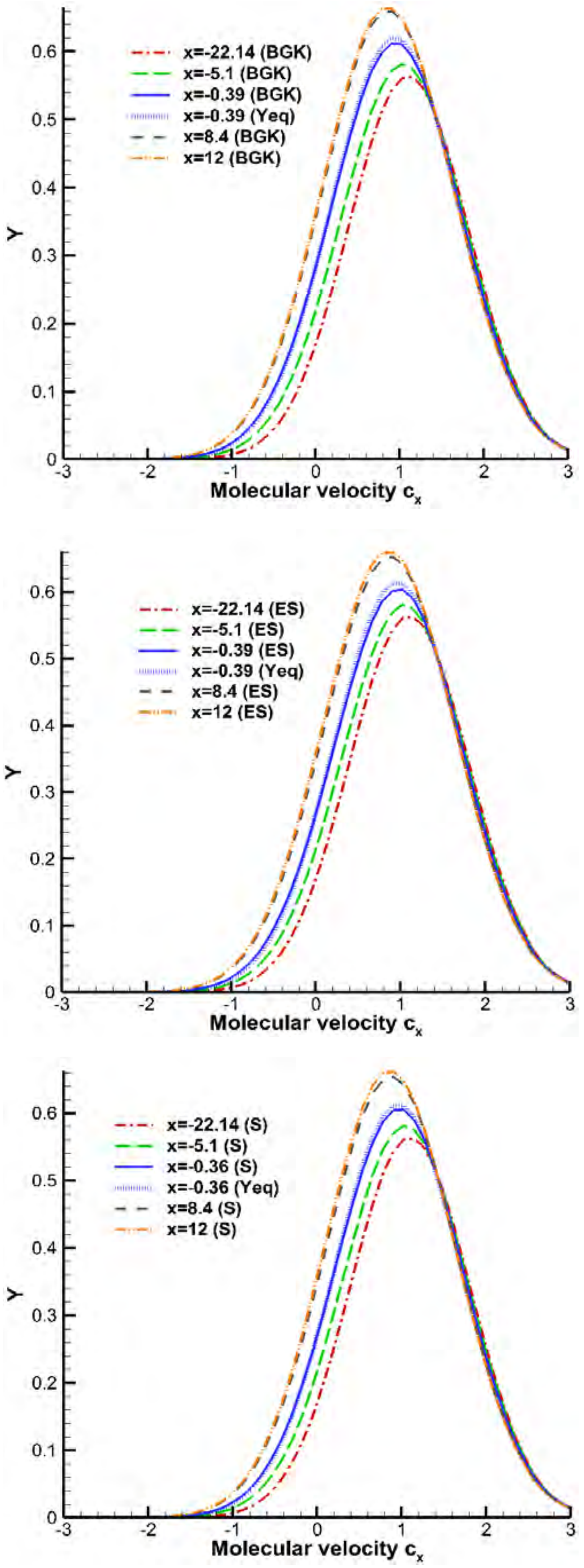

Figure 4.23: Distribution functions Y by the BGK, ES and S models along with the corresponding equilibrium distributions for M_1=1.2.

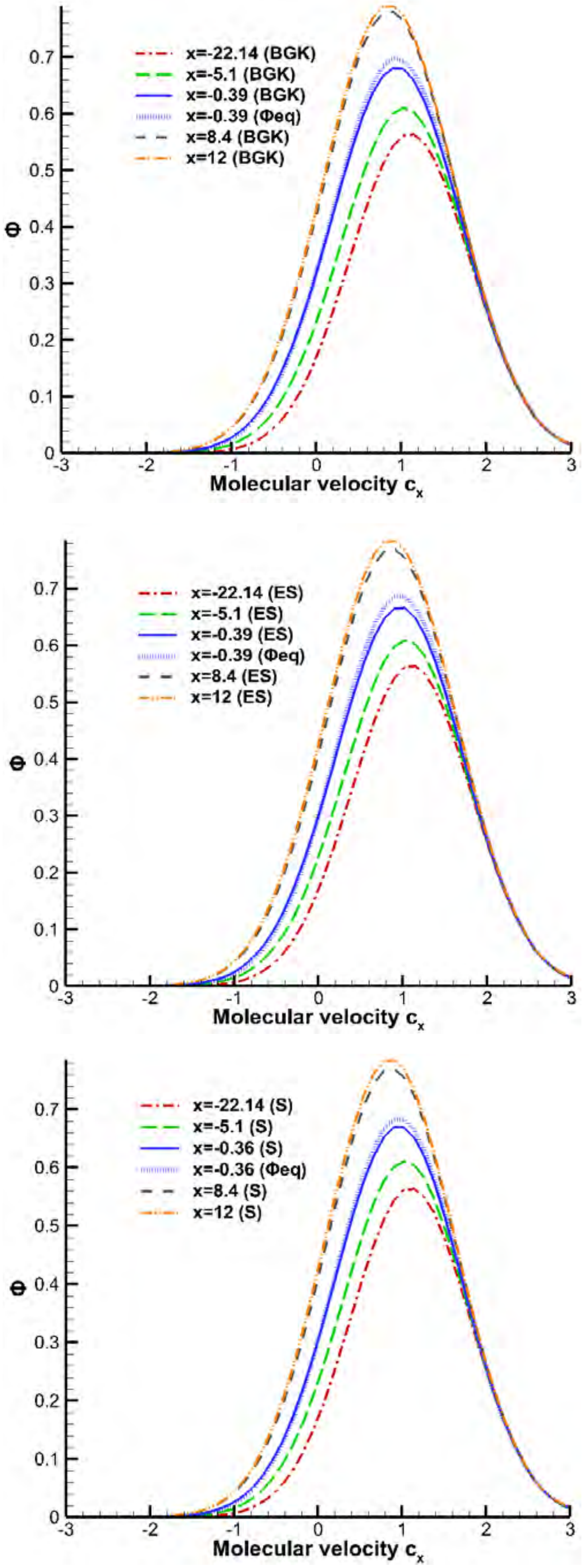

Figure 4.24: Distribution function Φ by the BGK, ES and S models along with the corresponding equilibrium distributions for $M_1=1.2$

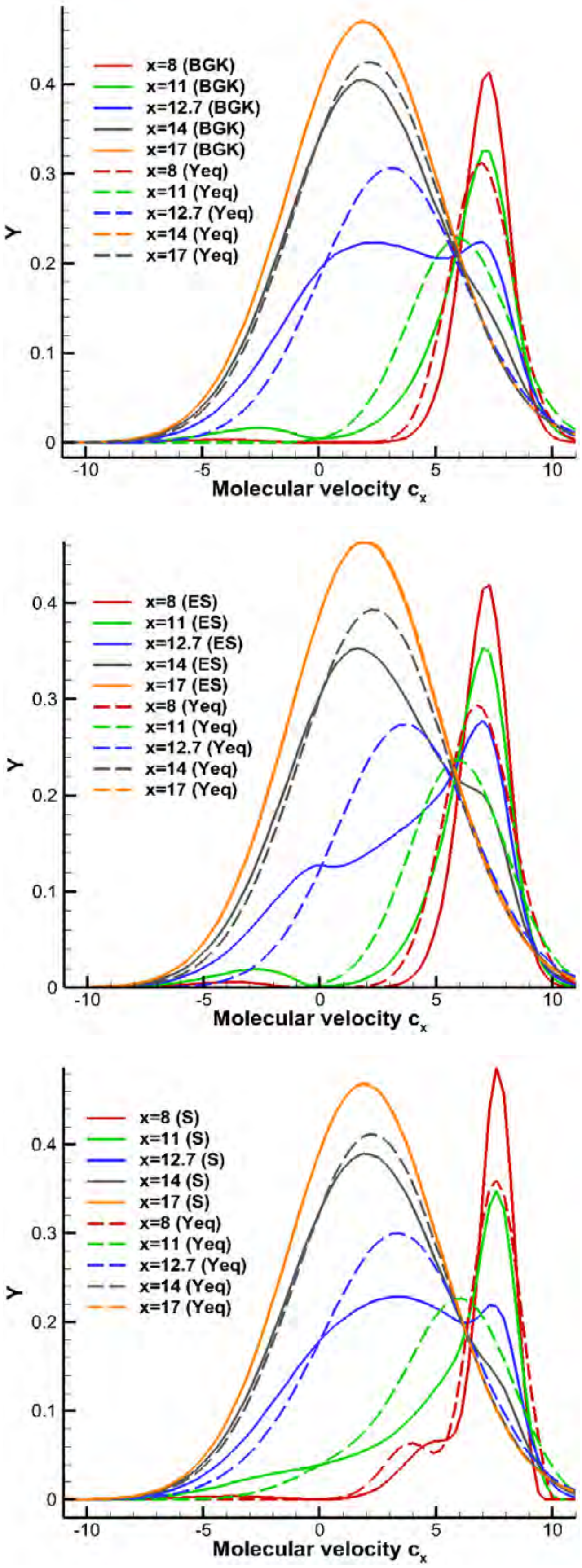

Figure 4.25: Distribution functions Y by the BGK, ES and S models along with the corresponding equilibrium distributions for M_1=8.

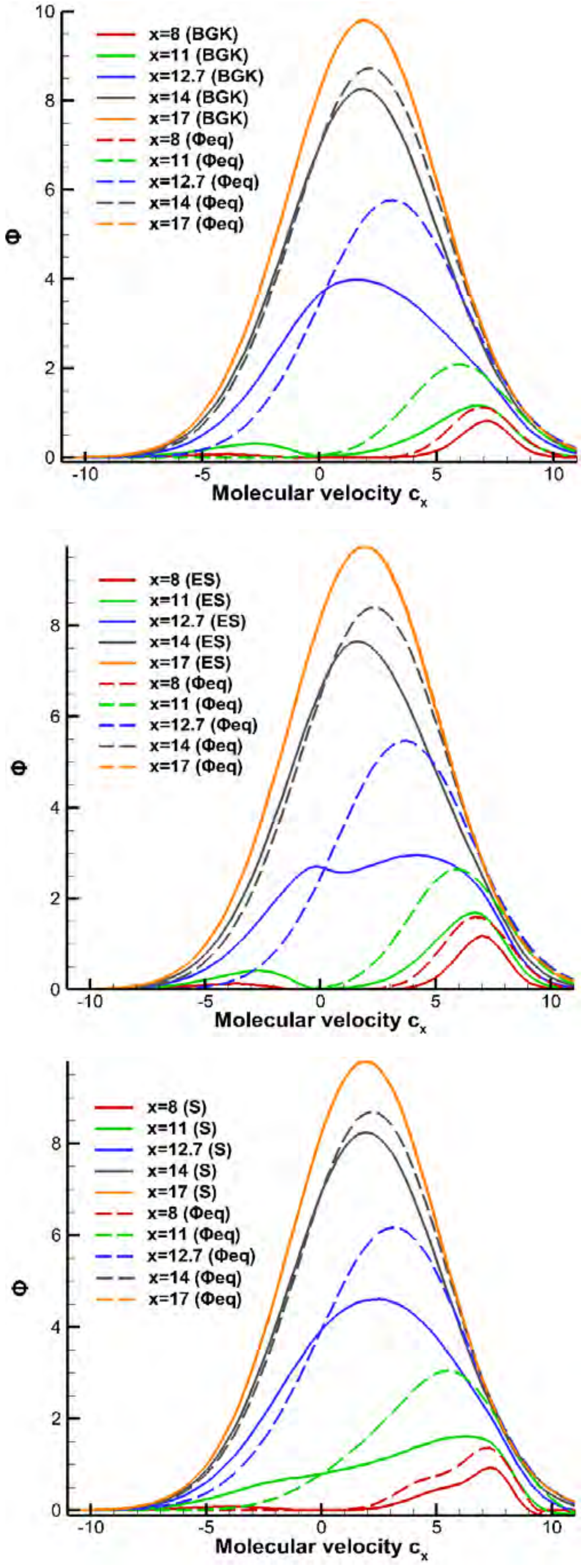

Figure 4.26: Distribution function Φ by the BGK, ES and S models along with the corresponding equilibrium distributions for M_1=8.

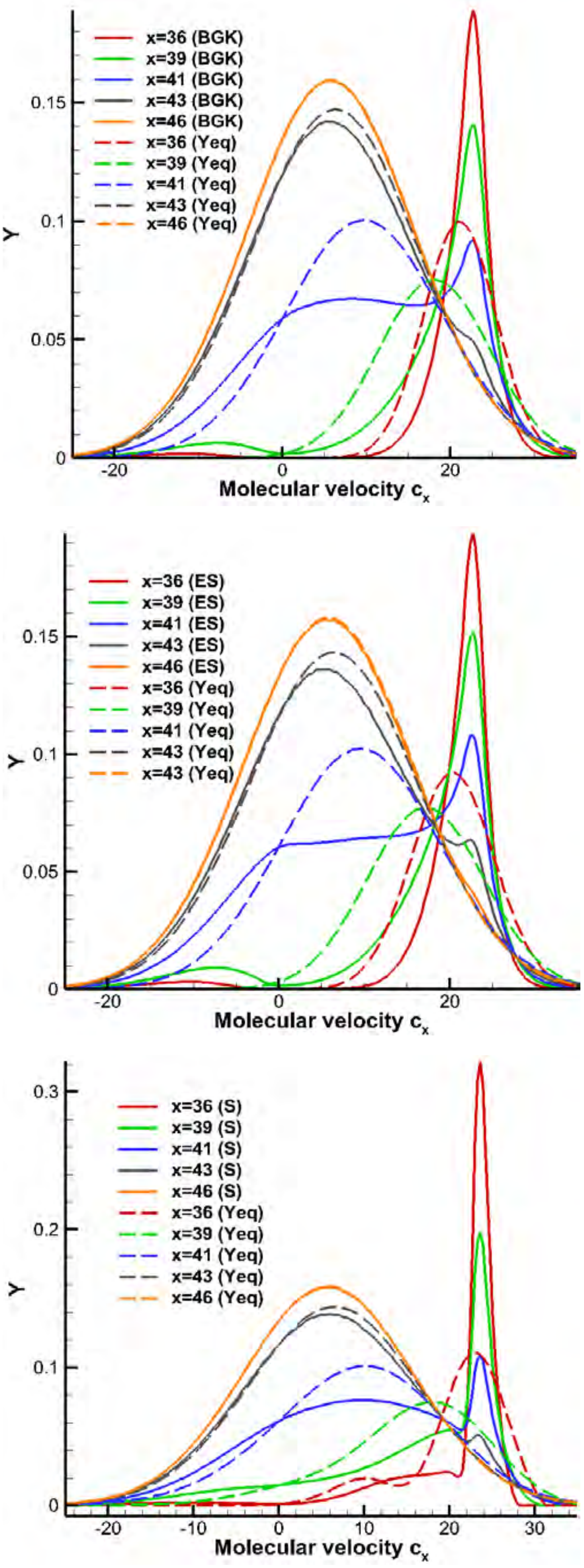

Figure 4.27: Distribution functions Y by the BGK, ES and S models along with the corresponding equilibrium distributions for M_1=25

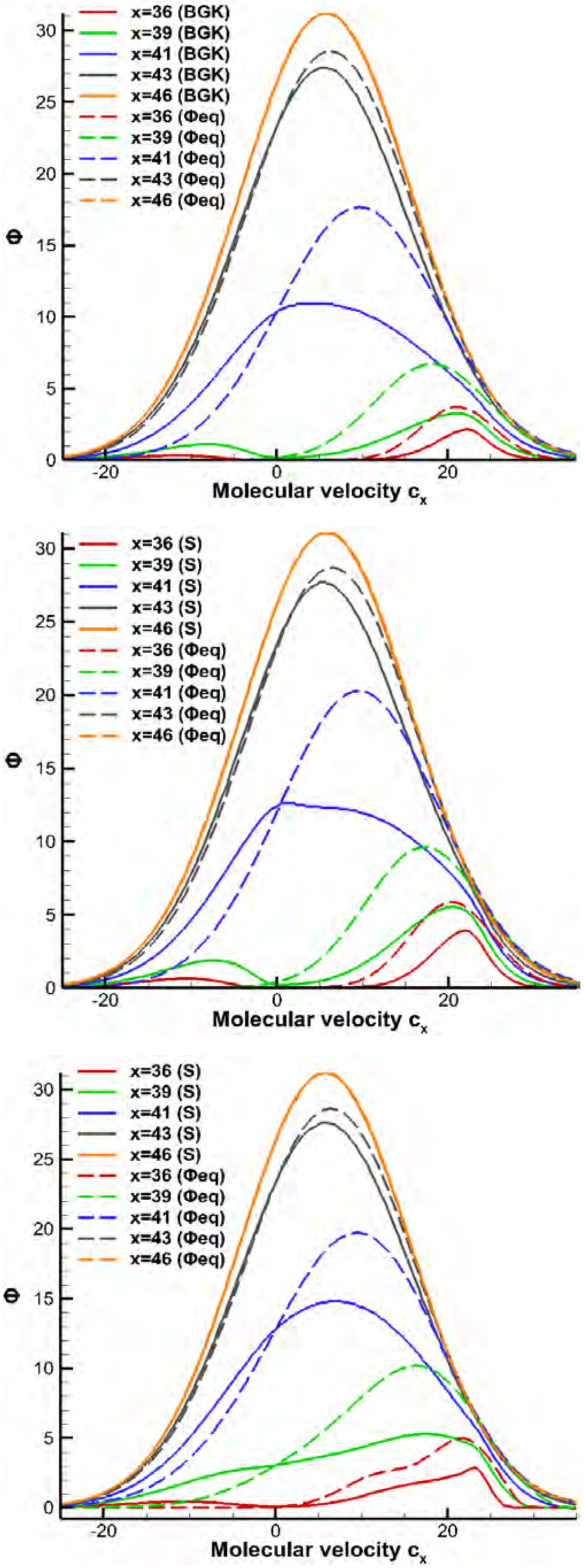

Figure 4.28: Distribution function Φ by the BGK, ES and S models along with the corresponding equilibrium distributions for M_1=25.

4.6 Range of validity of the Navier-Stokes approach

One of the main objectives of this thesis is to examine the validity of the Navier-Stokes approach. Hence, after it is established that the S model complies much better with the experiments as well as with the DCMC and BE solutions than the other two models, its results are compared with the hydrodynamic approach. The comparisons are made for the hard sphere molecules at M_1=1.2, 2 and 3. They are not applied in very strong shock waves because it is well expected that the NS approach will fail. The case of M_1=8 is also presented in order to demonstrate the inadequacy of the continuum theory.

Figures 4.29, 4.30, 4.31 and 4.32 show the density, temperature, velocity and heat flux inside a shock layer by both approaches. At M_1=1.2 the standard NS solution is very close to the S model solution. However, the results from the hydrodynamic approach begin to differ in greater Mach numbers. More specifically the discrepancies are evident at M_1=2 and 3 and this particularly true in the heat fluxes. As expected the NS solution completely fails at M_1=8. In general, the critical Mach number for the validity of the NS equations is about M_1=1.4. At that Mach number the reciprocal shock thickness is 0.1, which happens to be the starting point of the transition regime and the limiting point where the NS solution is valid. Hence, it is obvious that NS solutions are seriously deviated from the results of the S model, so that the continuum predictions seem to be invalid for shock Mach numbers greater than two, which confirms previous works on weak shock waves [39]. The variations are rapidly increased for M_1=8 and the profiles of all the macroscopic quantities are extremely steep. More specifically, the density has lesser deviations while the most significant ones are presented in the heat flux. The deviations are also present in the locations and of course in the thickness of the shock wave.

It is also seen that there is a prominent increase in the separation distance between the temperature and density profiles as the Mach number is increased from 1.2 up to 8 which manifests that the normal shock wave is a non-equilibrium flow with large departures from thermodynamic equilibrium. Finally, it is interesting to note that the prediction of the heat flux distribution is so poor that the macroscopic continuum theory based on the Chapmann-Enskog expansion has difficulty in describing sensitive higher-order flow moments of the distribution function.

Figures 4.33, 4.34 and 4.35 present the distribution functions Y^{NS} and Φ^{NS} which are compared with the corresponding distribution functions from the S model for M_1=1.2, 2, 3 and 8. At Mach numbers 2, 3 and 8, the position of the shock wave is different for the S model than the NS equations. Therefore, in order to compare the same positions for the two approaches, the results are projected to match the S model positions. Again, five typical points are presented, two of them are in the upstream area, one is in the middle of the shock front and the remaining two in the downstream area.

It is obvious that for both the distribution functions Y and Φ, the results are very close at M_1=1.2. This similarity is expected because the solution is in the continuum regime where both approaches give a correct solution throughout the computational domain. However, for M_1=2, the deviations are clear, even at x=9 where it is before from the shock wave. The distributions functions seem to be closer in the upstream area, while they are more far apart in the downstream region. The variations are of the same order of magnitude for the distribution function Y, while for the distribution function Φ, they are far more significant. Furthermore, at M_1=8, there is not even qualitatively agreement. Specifically, the NS profiles at the first two locations are completely underestimated, while in the other locations they may seem look but their magnitude differ significantly. Hence, it is partially explained why the variations exist between the macroscopic quantities of the two approaches. Finally, it is seen that the deviations are increased with increasing Mach number and after a certain Mach number the hydrodynamic approach is completely inadequate.

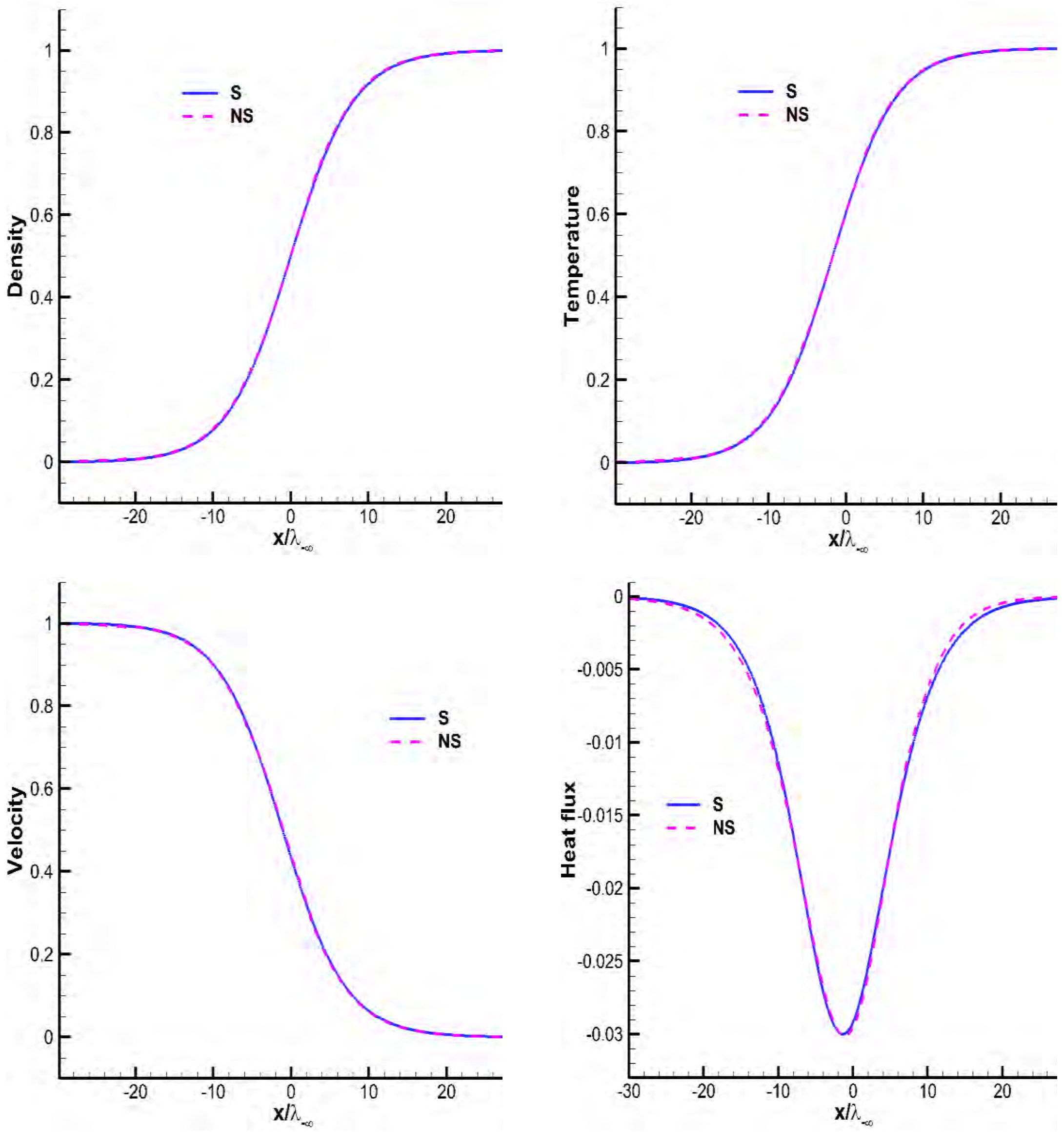

Figure 4.29: Comparison of normalized density, temperature, velocity and heat flux between the S model and the Navier-Stokes approach at M_1=1.2.

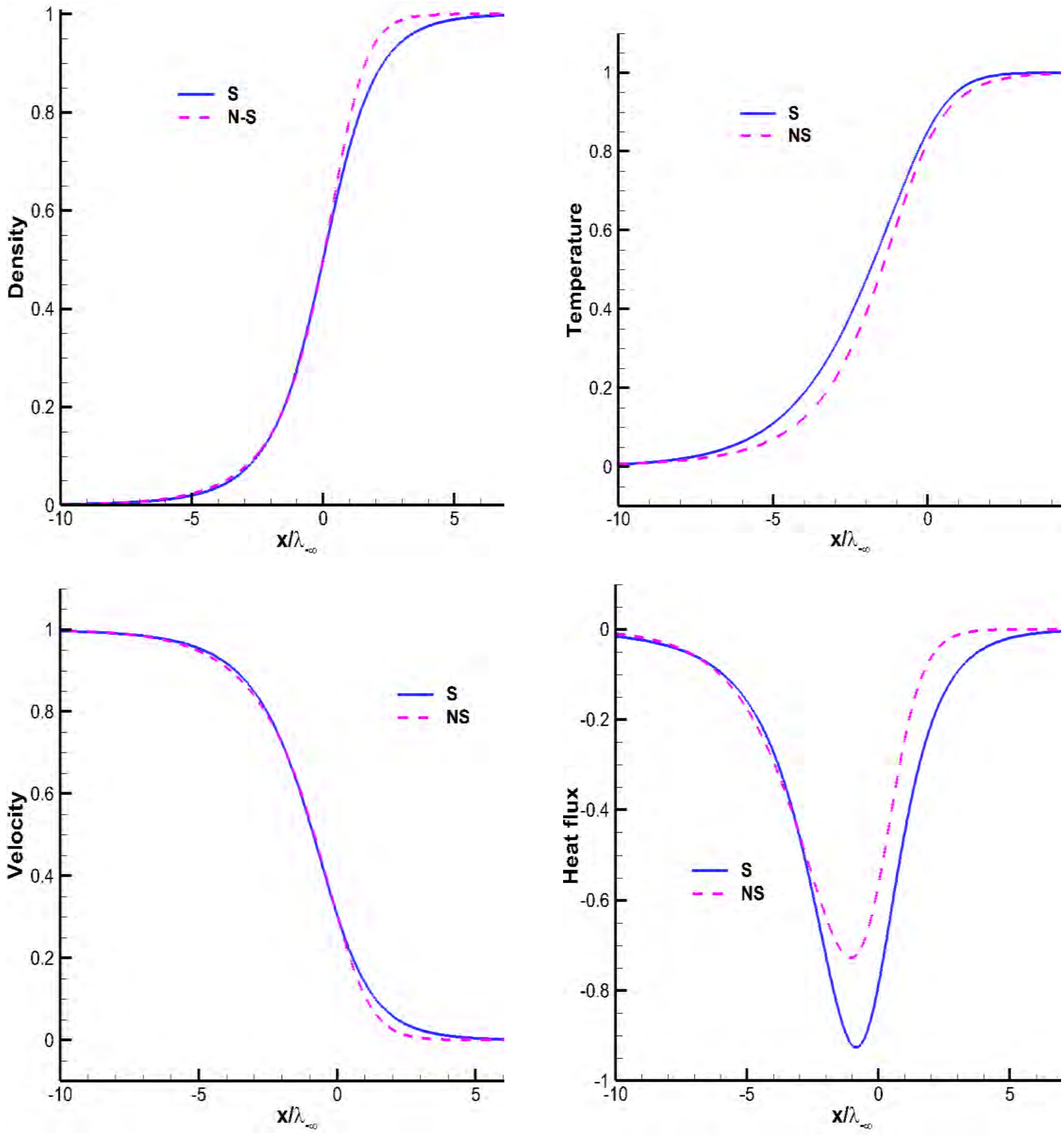

Figure 4.30: Comparison of normalized density, temperature, velocity and heat flux between the S model and the Navier-Stokes approach at $M_1=2$.

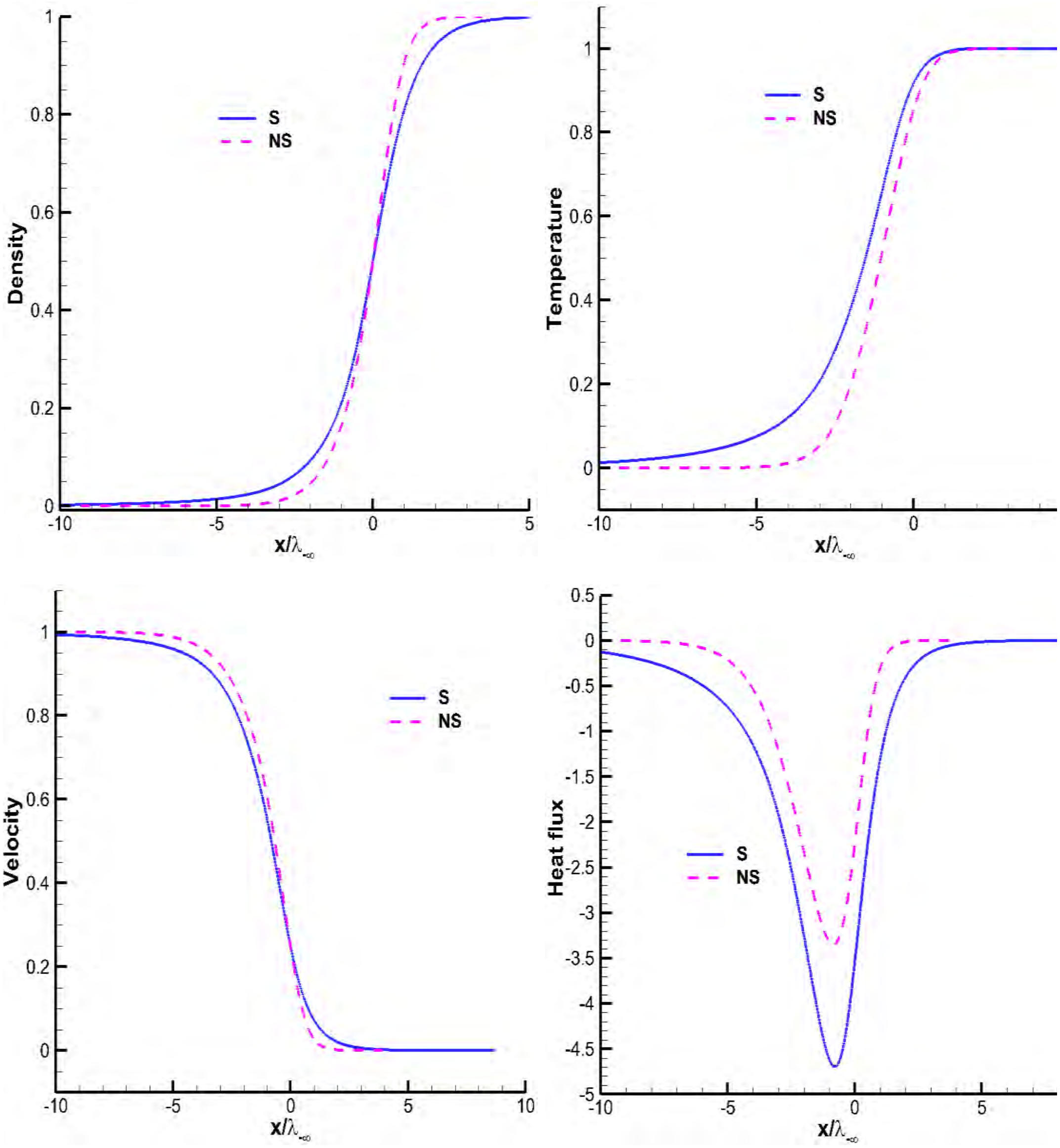

Figure 4.31: Comparison of normalized density, temperature, velocity and heat flux between the S model and the Navier-Stokes approach at M_1*=3.*

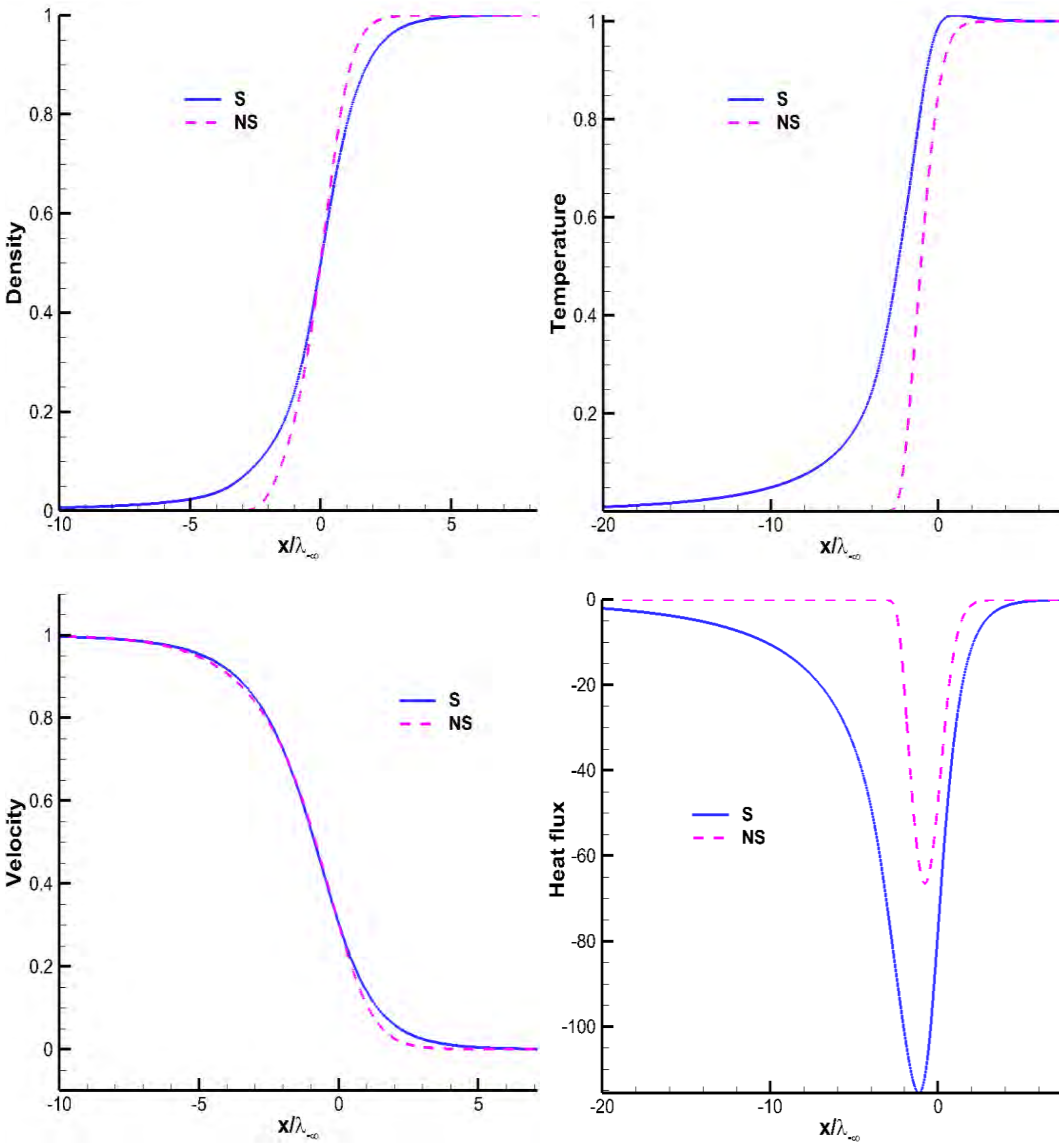

Figure 4.32: Comparison of normalized density, temperature, velocity and heat flux between the S model and the Navier-Stokes approach at M_1=8.

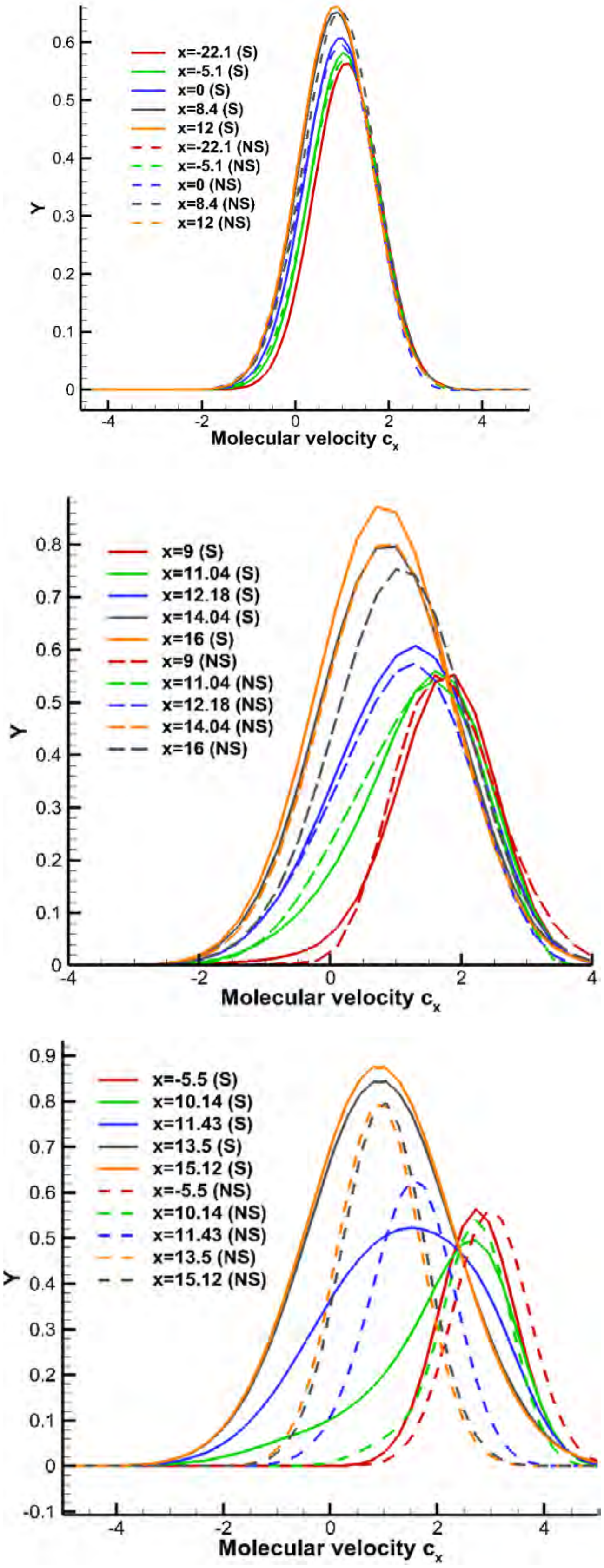

Figure 4.33: Distribution function Y computed by the S model and the NS approach at M_1=1.2, 2 and 3 at several locations.

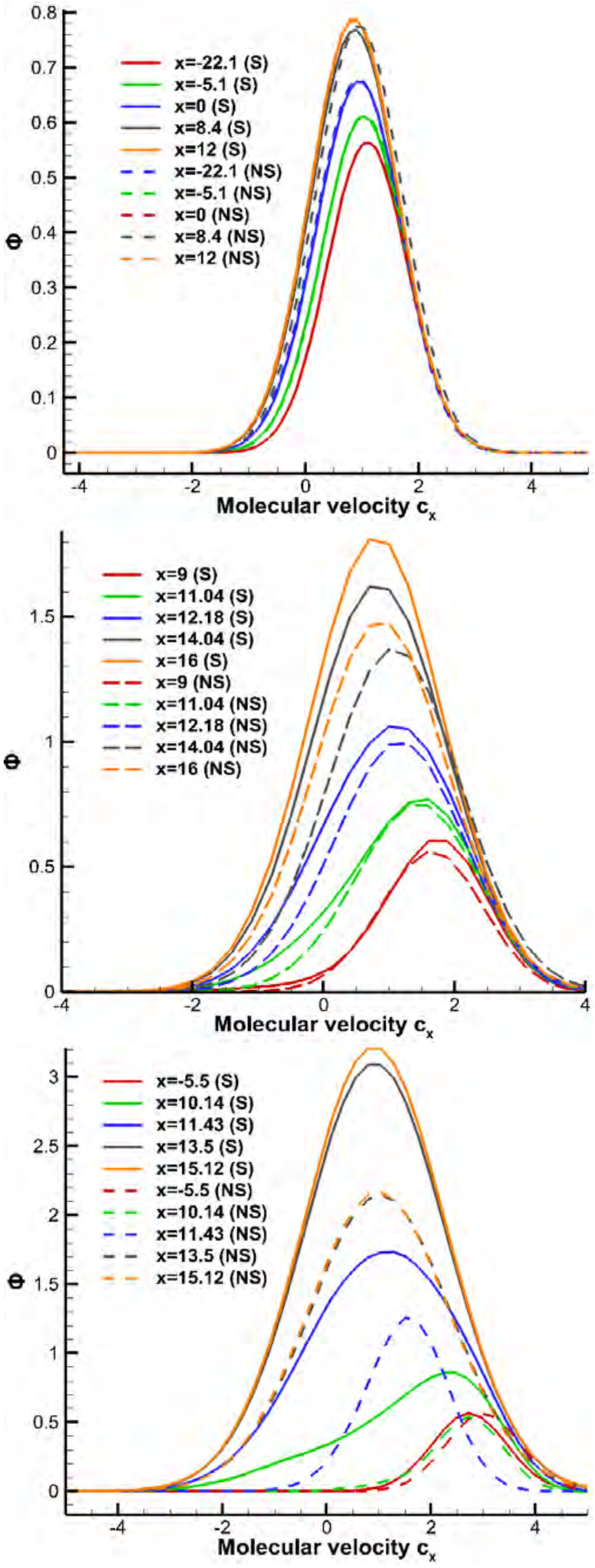

Figure 4.34: Distribution function Φ computed by the S model and the NS approach at M_1=1.2, 2 and 3 at several locations.

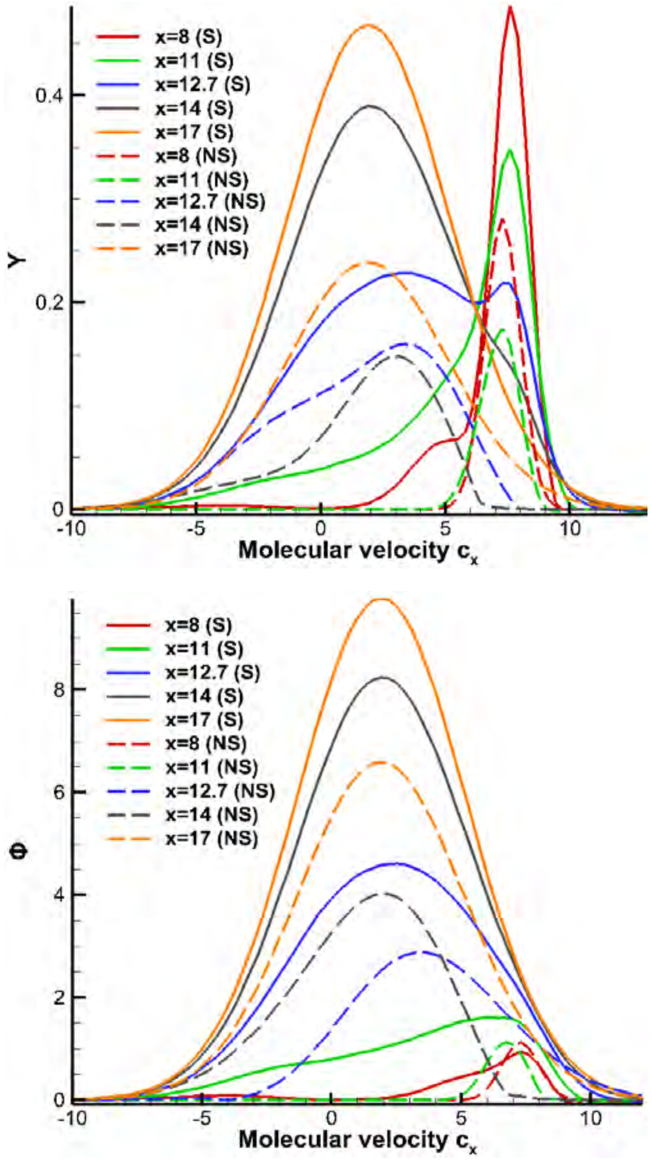

Figure 4.35: Distribution functions Y and Φ computed by S model and NS approach at M_1=8 at several locations.

Chapter 5

Concluding remarks

The scope of the present work is the investigation of the shock wave structure in a wide range of the Mach number. This is a problem that has been used as a test bed in order to validate the accuracy of the implemented kinetic models, namely the BGK, the ES and the S models, as well as of the developed nonlinear kinetic codes. Comparison with corresponding computational results obtained by other kinetic solvers such as the DSMC method and the direct solution of the Boltzmann equation, as well as with experimental results is performed. In addition to the detailed macroscopic distributions across the shock wave in terms of the Mach number other issues related to the shock thickness and the importance of the involved intermolecular potential model are also discussed. The problem has been also solved by a typical Navier-Stokes solution and then the range of validity of the NS approach is presented.

Following a brief introduction and a literature review in Chapter 1, the mathematical formulation of the implemented models is presented in the Chapter 2. In Chapter 3, the numerical schemes for the kinetic and NS approaches are described. Extensive results are being presented for various Mach numbers in Chapter 4.

In order to model the flow, we use kinetic models and the NS equations coupled to Rankine- Hugoniot boundary conditions. The kinetic solution is based on the discrete velocity method and the hydrodynamic is computed using the Runge-Kutta method. All macroscopic distributions of practical interest are computed (density, velocity, parallel, perpendicular and total temperatures, heat flux, pressure). Apart from them, the distribution functions for both approaches are computed.

It has been found that the S model yields the most accurate results in all Mach numbers providing an excellent agreement with the Boltzmann equation, the DCMC method and measurements. Although the ES model has been built in order to catch the shock wave structure it turns out that there is good agreement only at small and moderate Mach numbers, while in high Mach numbers significant discrepancies are observed. The BGK model is inadequate even in small Mach numbers which is expected due to its deficiency to properly compute at the same time the transport coefficients of viscosity and thermal conductivity. Also, the CPU time in the BGK model is too long compared to the other ones. Hence, the S model, which requires moderate CPU time, is considered as the most appropriate model in order to compute shock structure for all the Mach numbers.

The reciprocal shock thickness is computed for all three kinetic models. It is compared with DCMC and experiment and only the S model provides an accurate profile. An interesting issue is that as the Mach number is increased the shock thickness is rapidly decreased up to a characteristic Mach number and then is increased in a very slow pace. This minimum thickness of the shock front which is observed at about Mach number equal to 3 is analogous to the so-called Knudsen minimum and it has been also reported in previous theoretical and experimental works. Furthermore, the effect of the intermolecular potential is critical specifically as the Mach number is increased. Also, the computational time is presented in terms of the Mach number and it is found that its maximum values occur at about Mach numbers equal to 2 and 3.

It has been also found that the hydrodynamic approach cannot correctly compute the shock front at large Mach numbers. The NS distribution function is presented in order to justify the deviations. It is shown that it matches the corresponding S model distribution function only at very small numbers. Actually the NS approach is valid only up to a Mach number of about 1.5 where the flow is considered still close to local equilibrium. Above that limit the local Knudsen number is increased above the characteristic value of 0.1 and the flow enters into the transition regime where the classical constitutive laws fail.

The present work may be extended to tackle two-dimensional normal and oblique shock waves which are of more practical interest. To achieve that, in a computationally efficient manner, the code may be upgraded to run in GPUs. In parallel the development of an in-house DSMC solver will be more than useful for comparison purposes. Furthermore, the observed minimum at the shock wave thickness in terms of the Mach number may be investigated using the recently introduced DSMC decomposition approach, where the distribution function is split into two parts namely the ballistic and collision parts. Finally, it could be of major interest to use the present benchmark shock wave problem in order to investigate the potential of multiscale approaches developing a hybrid hydrodynamic-kinetic code.

References

1. W. Weiss, Continuous shock structure in extended thermodynamics, Phys. Rev. E 52, R5760, (1995)
2. Jennings, S, The mean free path in air. Journal of Aerosol Science 19 (2): 159. (1988)
3. H. Alsmeyer, Density profiles in argon and nitrogen shock waves measured by the absorption of an electron beam. J. Fluid Mech. 74, 497, (1976)
4. Karniadakis, G.E. and Beskok A., Microflows: Fundamentals and Simulations. Springer-Verlag, Berlin, (2000)
5. Gad-el Hak, M., The MEMS Handbook. CRC Press, Florida, USA, (2002)
6. L.C. Woods, An Introduction to the Kinetic Theory of Gases and Magneto plasmas, Oxford University Press, Oxford, (1993)
7. H. M. Mott-Smith, The Solution of the Boltzmann Equation for a Shock Wave, Phys. Rev. 82, 885 (1951)
8. B. Schmidt, Electron Beam Density Measurements in Shock Waves in Argon, J. Fluid Mech. 39, 361 (1969)
9. H. Grad, On the kinetic theory of rarefied gases, Commun. Pure Appl. Maths 2, 331 (1949)
10. I. Muller and T. Ruggeri, Rational Extended Thermodynamics (Springer, New York, (1998)
11. F. Robben and L. Talbot, Measurements of Rotational Temperatures in a Low Density Wind Tunnel, Phys. Fluids, (1966)
12. D. A. Erwin, G. C. Pham-Van-Diep, E. P. Muntz, Non-equilibrium gas flows. I: A detailed validation of Monte Carlo direct simulation for monatomic gases, Physics of Fluids A 3, 697 (1991)
13. Kun Xu, A Gas-Kinetic BGK Scheme for the Navier–Stokes Equations and Its Connection with Artificial Dissipation and Godunov Method, Journal of Computational Physics 171, 289–335 (2001)
14. Bird, G. A., Molecular Gas Dynamics and the Direct Simulation of Gas Flows. Oxford University Press, Oxford, (1994)
15. P. L. Bhatnagar, E. P. Gross, and M. Krook, A model for collision processes in gases I: Small amplitude processes in charged and neutral one-component systems, Phys. Rev. 94, 511 (1954)

16. Shakhov, E. M., Method of Investigation of Rarefied Gas Flows. Nauka, Moscow, (1974). [in Russian]
17. L. H. Holway, New statistical models for kinetic theory: Methods of construction, Jr., Phys. Fluids 9, 1958 (1966)
18. Launius, Roger D.; Jenkins, Dennis R., Coming Home: Reentry and Recovery from Space. NASA. (2012)
19. Liepmann, Hans W.; Roshko A., Elements of Gasdynamics, New York, (1957)
20. Ya. B. Zel'dovich, Yu. P. Raizer, Physics of Shock Waves and High-Temperature Hydrodynamic Phenomena, Academic Press, New York, (1966)
21. S. K. Shrivastava, Kailash. Shock wave treatment in medicine. Journal of Biosciences, Volume 30, Issue 2, pp 269-275 (2005)
22. Currie I. G., Fundamental mechanics of fluids, McGraw-Hill, New York (1974)
23. Macrossan, M.N., 251h Int. Symp. on Rarefied Gas Dynamics, St. Petersburg, Russia, 759. (2006)
24. H. W. Liepmann, R. Narasimha, and M. T. Chahine, Structure of a Plane Shock Layer, Phys. Fluids 5, 1313 (1962)
25. Masatsuka K., I do like CFD, VOL.1, Second Edition, *Yorktown* (2013).
26. Valougeorgis D., Notes on kinetic theory, University of Thessaly Press, (2015)
27. Bird, G. A., Monte Carlo simulation in an engineering context. Progr. Astro. Aero. 74, 239-255. (1981)
28. Gilbard D., Paolucci D.: The structure of shock waves in the continuum theory of fluids. Journal for Rational Mechanics and Analysis 2, (1953)
29. Valougeorgis D., Notes on computational methods, University of Thessaly Press, (2005)
30. Pantazis S., Simulation of transport phenomena in conditions far from thermodynamic equilibrium via kinetic theory with applications in vacuum technology and MEMS (Ph.D. dissertation), University of Thessaly - Department of Mechanical Engineering, Volos, Greece, (2008)
31. Giddens D., Huang A., Young V., Evaluation of two statistical models using the shock structure problem, Physics of Fluids 14, 2645 (1971)
32. Shakhov, E. M., Shock structure in a monoatomic gas. Gaza, Moscow, 1969.
33. Hicks B. L. and Yen S. M., Solution of the non-linear Boltzmann equation for plane shock waves in Rarefied Gas Dynamics, L. Trilling and H. Y. Wachman, eds.. Vol. I, 313-318, Academic Press, New York (1969).

34. Cercignani C., Rarefied Gas Dynamics, Cambridge University Press (2000)
35. Kun Xu, Juan-Chen Huang, An improved unified gas-kinetic scheme and the study of shock structures, MA Journal of Applied Mathematics 76, 698−711 (2011)
36. Ohwada T. Structure of normal shock waves: direct numerical analysis of the Boltzmann equation hard-sphere molecules, Physics of Fluids A, 5, 217–234 (1993)
37. Greenshields C and Reese M. J., The structure of shock waves as a test of Brenner's modifications to the Navier-Stokes equations. Journal of Fluid Mechanics, 580. pp. 407-429. (2006)
38. Bird, G. A., Aspects of the Structure of Strong Shock Waves, Physics of Fluids 13, 1172 (1970)
39. Pham-Van-Diep, G.C., Erwin, D.A., and Muntz, E.P., Testing continuum descriptions of low Mach number shock structures. Journal of Fluid Mechanics, 232, 403–413 (1991)

Appendix A

Derivation of reduced distribution functions

The detailed derivation for both the NS distribution functions Y^{NS} and Φ^{NS} are presented in this section. It is important to calculate every component of the stress tensor. The detailed calculations are given in Eqs. (A.1-A.14).

- Distribution function *Y*

$$\begin{gathered}\frac{\rho}{\pi^{3/2}\tau^{3/2}}\frac{q_x\left(c_x-u_x\right)}{p\tau}\int_{-\infty}^{\infty}\int_{-\infty}^{\infty}e^{-\frac{\left(c_x-u_x\right)^2+c_y^2+c_z^2}{\tau}}\left(1-4\frac{\left(c_x-u_x\right)^2+c_y^2+c_z^2}{5\tau}\right)dc_ydc_z= \\ \frac{\rho}{\pi^{1/2}\tau^{3/2}}\frac{2q_x\left(c_x-u_x\right)}{5p}exp\left[-\frac{\left(c_x-u_x\right)^2}{\tau}\right]\left(-4\left(c_x-u_x\right)^2+\tau\right)\end{gathered}\tag{A.1}$$

$$\begin{gathered}\frac{\rho}{\pi^{3/2}\tau^{3/2}}\frac{\sigma_{xx}}{p}\int_{-\infty}^{\infty}\int_{-\infty}^{\infty}exp\left[-\frac{\left(c_x-u_x\right)^2+c_y^2+c_z^2}{\tau}\right]\frac{\left(c_x-u_x\right)^2}{\tau}dc_ydc_z= \\ \frac{\rho}{\pi^{1/2}\tau^{3/2}}\frac{\sigma_{xx}\left(c_x-u_x\right)^2}{p}exp\left[-\frac{\left(c_x-u_x\right)^2}{\tau}\right]\end{gathered}\tag{A.2}$$

$$\begin{gathered}\frac{\rho}{\pi^{3/2}\tau^{3/2}}\frac{\sigma_{yy}}{p}\int_{-\infty}^{\infty}\int_{-\infty}^{\infty}exp\left[-\frac{(c_x-u_x)^2+c_y^2+c_z^2}{\tau}\right]\frac{c_y^2}{\tau}dc_ydc_z= \\ \frac{\rho}{\pi^{1/2}\tau^{1/2}}\frac{\sigma_{yy}}{2p}exp\left[-\frac{\left(c_x-u_x\right)^2}{\tau}\right]\end{gathered}\tag{A.3}$$

$$\begin{gathered}\frac{\rho}{\pi^{3/2}\tau^{3/2}}\frac{\sigma_{zz}}{p}\int_{-\infty}^{\infty}\int_{-\infty}^{\infty}exp\left[-\frac{(c_x-u_x)^2+c_y^2+c_z^2}{\tau}\right]\frac{c_z^2}{\tau}dc_ydc_z= \\ \frac{\rho}{\pi^{1/2}\tau^{1/2}}\frac{\sigma_{zz}}{2p}exp\left[-\frac{(c_x-u_x)^2}{\tau}\right]\end{gathered}\tag{A.4}$$

$$\frac{\rho}{\pi^{3/2}\tau^{3/2}}\frac{\sigma_{xy}}{p}\int_{-\infty}^{\infty}\int_{-\infty}^{\infty}exp\left[-\frac{(c_x-u_x)^2+c_y^2+c_z^2}{\tau}\right]\frac{\left(c_x-u_x\right)c_y}{\tau}dc_xdc_y=0\tag{A.5}$$

$$\frac{\rho}{\pi^{3/2}\tau^{3/2}}\frac{\sigma_{zy}}{p}\int_{-\infty}^{\infty}\int_{-\infty}^{\infty}exp\left[-\frac{(c_x-u_x)^2+c_y^2+c_z^2}{\tau}\right]\frac{c_zc_y}{\tau}dc_ydc_z=0\tag{A.6}$$

$$\frac{\rho}{\pi^{3/2}\tau^{3/2}}\frac{\sigma_{xz}}{p}\int_{-\infty}^{\infty}\int_{-\infty}^{\infty}exp\left[-\frac{(c_x-u_x)^2+c_y^2+c_z^2}{\tau}\right]\frac{\left(c_x-u_x\right)c_z}{\tau}dc_xdc_z=0\tag{A.7}$$

- Distribution function Φ

$$\begin{gathered}\frac{\rho}{\pi^{3/2}\tau^{3/2}}\frac{q_x\left(c_x-u_x\right)}{p\tau}\int_{-\infty}^{\infty}\int_{-\infty}^{\infty}(c_y^2+c_z^2)exp\left[-\frac{(c_x-u_x)^2+c_y^2+c_z^2}{\tau}\right]\\ \left(1-4\frac{(c_x-u_x)^2+c_y^2+c_z^2}{5\tau}\right)dc_ydc_z=\\ \frac{\rho}{\sqrt{\pi}}\frac{2q_x\left(c_x-u_x\right)}{5p\sqrt{\tau}}exp\left[-\frac{(c_x-u_x)^2}{\tau}\right]\left(4(c_x-u_x)^2+3\tau\right)\end{gathered}\tag{A.8}$$

$$\begin{gathered}\frac{\rho}{\pi^{3/2}\tau^{3/2}}\frac{\sigma_{xx}}{p}\int_{-\infty}^{\infty}\int_{-\infty}^{\infty}(c_y^2+c_z^2)exp\left[-\frac{(c_x-u_x)^2+c_y^2+c_z^2}{\tau}\right]\frac{\left(c_x-u_x\right)^2}{\tau}dc_ydc_z=\\ \frac{\rho}{\sqrt{\pi}}\frac{\sigma_{xx}\left(c_x-u_x\right)^2}{\sqrt{\tau}p}exp\left[-\frac{(c_x-u_x)^2}{\tau}\right]\end{gathered}\tag{A.9}$$

$$\begin{gathered}\frac{\rho}{\pi^{3/2}\tau^{3/2}}\frac{\sigma_{yy}}{p}\int_{-\infty}^{\infty}\int_{-\infty}^{\infty}(c_y^2+c_z^2)exp\left[-\frac{(c_x-u_x)^2+c_y^2+c_z^2}{\tau}\right]\frac{c_y^2}{\tau}dc_ydc_z=\\ \frac{\rho\sqrt{\tau}}{\sqrt{\pi}}\frac{\sigma_{yy}}{p}exp\left[-\frac{(c_x-u_x)^2}{\tau}\right]\end{gathered}\tag{A.10}$$

$$\begin{gathered}\frac{\rho}{\pi^{3/2}\tau^{3/2}}\frac{\sigma_{zz}}{p}\int_{-\infty}^{\infty}\int_{-\infty}^{\infty}(c_y^2+c_z^2)exp\left[-\frac{(c_x-u_x)^2+c_y^2+c_z^2}{\tau}\right]\frac{c_z^2}{\tau}dc_ydc_z=\\ \frac{\rho\sqrt{\tau}}{\sqrt{\pi}}\frac{\sigma_{zz}}{p}exp\left[-\frac{(c_x-u_x)^2}{\tau}\right]\end{gathered}\tag{A.11}$$

$$\frac{\rho}{\pi^{3/2}\tau^{3/2}}\frac{\sigma_{zy}}{p}\int_{-\infty}^{\infty}\int_{-\infty}^{\infty}(c_y^2+c_z^2)exp\left[-\frac{(c_x-u_x)^2+c_y^2+c_z^2}{\tau}\right]\frac{c_zc_y}{\tau}dc_ydc_z=0\tag{A.12}$$

$$\frac{\rho}{\pi^{3/2}\tau^{3/2}}\frac{\sigma_{xy}}{p}\int_{-\infty}^{\infty}\int_{-\infty}^{\infty}(c_y^2+c_z^2)exp\left[-\frac{(c_x-u_x)^2+c_y^2+c_z^2}{\tau}\right]\frac{(c_x-u_x)c_y}{\tau}dc_ydc_x=0\tag{A.13}$$

$$\frac{\rho}{\pi^{3/2}\tau^{3/2}}\frac{\sigma_{xz}}{p}\int_{-\infty}^{\infty}\int_{-\infty}^{\infty}(c_y^2+c_z^2)exp\left[-\frac{(c_x-u_x)^2+c_y^2+c_z^2}{\tau}\right]\frac{(c_x-u_x)c_z}{\tau}dc_xdc_z=0\tag{A.14}$$

Appendix B

Derivation of macroscopic distributions

In section 2.5, the macroscopic quantities are presented for this problem. The detailed calculations of these quantities are given in Eqs. (B.1-B.5).

Appendix

Density

$$\begin{gathered} n=\int_{-\infty}^{\infty}\int_{-\infty}^{\infty}\int_{-\infty}^{\infty} f\left(x,\xi_x,\xi_y,\xi_z\right) d\xi_y d\xi_z d\xi_x = \\ \frac{n_1}{\left(2R_iT_1\right)^{3/2}}\frac{\left(2R_iT\right)_1^{3/2}}{1}\int_{-\infty}^{\infty}\int_{-\infty}^{\infty}\int_{-\infty}^{\infty} g dc_y dc_z dc_x = \\ \rho\left(x\right)=\frac{n}{n_1}=\int_{-\infty}^{+\infty} Y\left(x,c_x\right) dc_x \end{gathered} \tag{B.1}$$

Velocity

$$\begin{gathered} \hat{u}_x=\frac{1}{n}\int_{-\infty}^{\infty}\int_{-\infty}^{\infty}\int_{-\infty}^{\infty} \xi_x f\,\partial\xi_x\partial\xi_y\partial\xi_z = \\ \frac{\sqrt{2R_iT_1}}{\hat{\rho}}\frac{n_1}{\left(2R_iT_1\right)^{3/2}}\frac{\left(2R_iT_1\right)^{3/2}}{n_1}\int_{-\infty}^{\infty}\int_{-\infty}^{\infty}\int_{-\infty}^{\infty} c_x g dc_y dc_z dc_x = \\ u_x\left(x\right)=\frac{\hat{u}_x}{\sqrt{2R_iT_1}}=\frac{1}{\rho}\int_{-\infty}^{\infty} c_x Y\left(x,c_x\right) dc_x \end{gathered} \tag{B.2}$$

Temperature

$$\begin{gathered} T=\frac{m}{3kn}\int_{-\infty}^{\infty}\int_{-\infty}^{\infty}\int_{-\infty}^{\infty}\left(\left(\xi_x-\hat{u}_x\right)^2+\xi_y^2+\xi_z^2\right) f\,\partial\xi_x\partial\xi_y\partial\xi_z \rightarrow \\ T=\frac{m}{3kn}\frac{n_1}{\left(2R_iT_1\right)^{3/2}}\frac{\left(2R_iT_1\right)^{3/2}2R_iT_1}{1} \\ \int_{-\infty}^{\infty}\int_{-\infty}^{\infty}\int_{-\infty}^{\infty}\left(\left(c_x-\hat{u}_x\right)^2+c_y^2+c_z^2\right) f dc_y dc_z dc_x \rightarrow \\ \tau=\frac{T}{T_1}=\frac{2}{3}\frac{1}{\rho}\left(\int_{-\infty}^{+\infty}\left\{\left(c_x-u_x\right)^2 L\right\} dc_x+\int_{-\infty}^{\infty}\Phi dc_x\right)\rightarrow \\ \tau\left(x\right)=\frac{T}{T_1}=\frac{2}{3}\frac{1}{\rho}\int_{-\infty}^{+\infty}\left\{\left(c_x-u_x\right)^2 L\left(x,c_x\right)+\Phi\left(x,c_x\right)\right\} dc_x \end{gathered} \tag{B.3}$$

Heat flux

$$\begin{gathered} \hat{q}_x=\frac{m}{2}\int_{-\infty}^{\infty}\int_{-\infty}^{\infty}\int_{-\infty}^{\infty}\left(\xi-\hat{u}\right)^2\left(\xi_x-\hat{u}_x\right) f\,\partial\xi_x\partial\xi_y\partial\xi_z \Rightarrow \\ q=\frac{\hat{q}_x}{P_1u_1}=\int_{-\infty}^{\infty}\int_{-\infty}^{\infty}\int_{-\infty}^{\infty}\left(c-\hat{u}\right)^2\left(c_x-\hat{u}_x\right) f\,\partial c_x\partial c_y\partial c_z = \\ =\int_{-\infty}^{+\infty}\left\{\left(c_x^3-u_x^3-\left(3c_xu_x^2+3c_x^2u_x\right)\right)Y\left(x,c_x\right)+\left(c_x-u_x\right)\Phi\left(x,c_x\right)\right\} dc_x \end{gathered} \tag{B.4}$$

Stress

$$\begin{gathered} \hat{\sigma}_{ij}=\int_{-\infty}^{\infty}\int_{-\infty}^{\infty}\int_{-\infty}^{\infty}\left(\xi_i-\hat{u}_j\right)\left(\xi_i-\hat{u}_j\right) f\,\partial\xi_x\partial\xi_y\partial\xi_z \Rightarrow \\ \sigma_{ij}=\frac{\hat{\sigma}_{ij}}{P_0u_0}=\int_{-\infty}^{\infty}\int_{-\infty}^{\infty}\int_{-\infty}^{\infty}\left(c_i-u_i\right)\left(c_j-u_j\right) g\,\partial c_x\partial c_y\partial c_z \end{gathered} \tag{B.5}$$